



Study of the degradation process of polyimide induced by  
high energetic ion irradiation

Dissertation am  
**Fachbereich Chemie der Philipps-Universität Marburg**  
vorgelegt von

**Daniel Severin**

**Study of the degradation process of polyimide induced  
by high energetic ion irradiation**

Dissertation

zur

Erlangung des Doktorgrades  
der Naturwissenschaften

(Dr. rer. nat.)

dem

Fachbereich Chemie der Philipps-Universität Marburg  
vorgelegt von

Daniel Severin

aus Marburg / Lahn

Marburg / Lahn 2008



Vom Fachbereich Chemie der Philipps-Universität Marburg  
am \_\_\_\_\_ angenommen.

Erstgutachter: Prof. Dr. W. Ensinger

Zweitgutachter: Prof. Dr. H. Jungclas

Tag der mündlichen Prüfung: 19. September 2008









---

## Abstract

The dissertation focuses on the radiation hardness of Kapton under extreme radiation environment conditions and is motivated by the application of this polyimide as insulator in superconducting magnets for the new Facility for Antiproton and Ion Research (FAIR) planned at the Gesellschaft für Schwerionenforschung (GSI). The new FAIR accelerators are expected to deliver protons and heavy ions of extreme energies (10 GeV/u) and unprecedented intensities ( $10^{12}$  ions/pulse). Reliable data of the radiation hardness of polymers concerning mechanical, electrical, and outgassing properties are of great interest also for other facilities such as the Large Hadron Collider (LHC) of CERN.

To study ion-beam induced modifications, Kapton foils were irradiated at the GSI linear accelerator UNILAC using several projectiles (e.g. Ti, Mo, Au, and U) within a large fluence regime ( $1 \times 10^{10} - 5 \times 10^{12}$  ions/cm<sup>2</sup>). The irradiated Kapton foils were analysed by means of infrared and UV/Vis spectroscopy, tensile strength measurement, mass loss analysis, and dielectric relaxation spectroscopy. For testing the radiation stability of Kapton at the cryogenic operation temperature (5-10 K) of the superconducting magnets, additional irradiation experiments were performed at the Grand Accélérateur National d' Ions Lourds (GANIL, France) focusing on the online analysis of the outgassing process of small volatile degradation fragments.

Results obtained by optical spectroscopy, tensile strength measurement and mass loss analysis show similar trends and can be scaled by the irradiation dose given by the product of fluence and energy deposited along the ion trajectory. Critical material degradation appears above a dose of 1 MGy. The investigations of the electrical properties analysed by dielectric relaxation spectroscopy exhibit a different trend: high fluence irradiations with light ions (e.g. Ti) lead to a slight increase of the conductivity, whereas heavy ions (e.g. Sm, Au) cause a drastic change already in the fluence regime of non-overlapping tracks ( $5 \times 10^{10}$  ions/cm<sup>2</sup>).

Online analysis of the outgassing process during irradiation at cryogenic temperatures shows the release of a variety of small gaseous molecules (e.g. CO, CO<sub>2</sub>, and short hydro carbons). Also a small amount of large polymer

fragments is identified and confirms the degradation mechanism of Kapton proposed in earlier studies. Simultaneous in-situ infrared spectroscopy gives evidence of accumulation of these small molecules inside the bulk polymer at cryogenic temperatures. During heat-up cycles, these fragments outgas in specific temperature zones.

The results obtained by the different analytical techniques allow the following conclusions which are of special interest for the application of Kapton as insulating material in a high-energetic particle radiation environment.

a) The material degradation measured with the optical spectroscopy and tensile strength tests are scalable with the dose deposited by the ions. The high correlation of the results allows the prediction of the mechanical degradation with the simple and non-destructive infrared spectroscopy. The degradation curve points to a critical material degradation which has to be expected above a dose of 1 MGy.

b) The dielectric relaxation spectroscopy indicates a dramatic increase in the conductivity induced by irradiation with heavy ions which pass a threshold of mass and deposited energy ( $dE/dx$ ). The phenomenon indicates that only a few hits (fluences of  $10^{10}$  ion/cm<sup>2</sup>) of a heavy high energetic ion leads to a significant increase of conductivity.

c) The degradation induced formation of small molecules and their outgassing even at cryogenic temperature cause a gas release during irradiation. At temperatures below 20 K, an additional accumulation of these molecules in the bulk material occurs and leads to a critical gas evolution during heat-up cycles.

---

## Zusammenfassung

Ziel der vorliegenden Arbeit war die Analyse der Strahlenbeständigkeit von Kapton gegenüber hochenergetischer Teilchenstrahlung. Hintergrund der Untersuchung ist der Einsatz dieses Polyimids als elektrischer Isolator in supraleitenden Magneten für das FAIR Projekt (Facility for Antiproton and Ion Research) der Gesellschaft für Schwerionenforschung (GSI). Diese neue Beschleunigeranlage erzeugt Protonen- und Schwerionenstrahlung mit extremen Energien (10 GeV/u) und sehr hohen Intensitäten ( $10^{12}$  Ionen/Puls).

Zuverlässige Daten über die Strahlenbeständigkeit von Polymeren hinsichtlich ihrer mechanischen und elektrischen Eigenschaften sowie ihres Ausgasverhaltens sind auch für andere Beschleunigerzentren wie z.B. den Large Hadron Collider (LHC) des CERNs von zentraler Bedeutung.

Kaptonfolien wurden am Linearbeschleuniger (UNILAC) der GSI mit verschiedenen Projektilen (z.B. Ti, Mo, Au und U) innerhalb eines breiten Fluenzbereichs ( $1 \times 10^{10} - 5 \times 10^{12}$  Ionen/cm<sup>2</sup>) bestrahlt, um die ionenstrahlinduzierte Materialveränderung zu untersuchen. Es folgten Analysen der bestrahlten Kaptonfolien mittels Infrarot- und UV/Vis Spektroskopie, Zug-Dehnungsmessungen, Massenverlustanalyse und Dielektrischer Relaxationsspektroskopie. Zur Testung der Strahlenbeständigkeit von Kapton bei den kryogenen Operationstemperaturen der supraleitenden Magnete (5-10 K) wurden zusätzliche Bestrahlungsexperimente am Grand Accélérateur National d'Ions Lourds (GANIL) in Frankreich durchgeführt. Diese konzentrierten sich auf die online Analyse von Ausgasprozessen kleiner, flüchtiger Abbaufragmente.

Die Ergebnisse der optischen Spektroskopie, der Zug-Dehnungsmessungen und der Massenverlustanalyse zeigen einheitliche Trends und sind skalierbar mit der Bestrahlungsdosis. Diese berechnet sich aus der Fluenz und der deponierten Energie entlang der Ionenspur. Ein kritischer Materialabbau tritt oberhalb einer Dosis von 1 MGy auf. Die Untersuchungen der elektrischen Eigenschaften mittels dielektrischer Relaxationsspektroskopie weisen einen anderen Trend auf: Hochfluenzbestrahlungen ( $> 10^{12}$  Ionen/cm<sup>2</sup>) mit leichten Ionen (z.B. Ti) führen nur zu einem leichten Anstieg der Leitfähigkeit, während schwere Ionen (z.B. Sm und Au) schon in einem Fluenzbereich von  $5 \times 10^{10}$  Ionen/cm<sup>2</sup> einen drastischen Anstieg der Leitfähigkeit verursachen.

Bemerkenswert erscheint, dass in diesem Fluenzbereich ein Spurüberlapp ausgeschlossen werden kann.

Die online Analyse des Ausgasprozesses während der Bestrahlung bei kryogenen Temperaturen zeigt, dass kleine, gasförmige Moleküle (CO, CO<sub>2</sub> und kurze Kohlenwasserstoffe) freigesetzt werden. Auch einige große Polymerfragmente ließen sich identifizieren und bestätigen den in früheren Arbeiten postulierten Abbaumechanismus von Kapton. Gleichzeitig belegt die in-situ Infrarotspektroskopie die Akkumulation kleiner Moleküle innerhalb des Polymers bei kryogenen Temperaturen. Diese Moleküle gasen während des Aufheizzyklus in spezifischen Temperaturbereichen aus.

Die Ergebnisse der einzelnen analytischen Methoden sind im Folgenden unter Berücksichtigung der Anwendung von Kapton als elektrisches Isolationsmaterial in einer Umgebung von hochenergetischer Partikelstrahlung zusammengefasst.

- a) Der mittels optischer Spektroskopie und Zug-Dehnungsmessungen definierte Materialabbau ist skalierbar mit der durch die Ionen deponierten Dosis. Die hohe Korrelation der Ergebnisse zwischen den Methoden ermöglicht die Vorhersage des mechanischen Abbaus mit Hilfe der einfachen, zerstörungsfreien Infrarotspektroskopie. Die Abbaukurve verweist auf einen kritischen Materialabbau oberhalb einer Dosis von 1 MGy.
- b) Die dielektrische Relaxationsspektroskopie zeigt einen dramatischen Anstieg der Leitfähigkeit bei Bestrahlung mit Ionen, die eine bestimmte Schwelle bezüglich Masse und deponierter Energie (dE/dx) überschritten haben. Die Ergebnisse veranschaulichen, dass nur wenige Einschläge von schweren, hoch energetischen Ionen (Fluenz von 10<sup>10</sup> Ionen/cm<sup>2</sup>) zu einer signifikanten Erhöhung der Leitfähigkeit führen.
- c) Die Bildung von kleinen Abbaufragmenten und deren Freisetzung sogar bei kryogenen Temperaturen führen zu einer Gasentwicklung während der Bestrahlung. Zusätzlich kommt es zu einer Akkumulation dieser Moleküle innerhalb des Polymers bei Temperaturen unter 20 K. Die bei tiefen Temperaturen immobilisierten, kleinen Moleküle verursachen eine enorme Gasfreisetzung während des Aufheizzyklus.

---

## Index of contents

Chapter 1 : Introduction .....	1
1.1 Radiation effects .....	1
1.2 Polymer modification by ionizing radiation .....	2
1.3 Radiation hardness of polymer materials .....	5
Chapter 2 : Motivation.....	7
2.1 FAIR project .....	7
2.2 Magnet design .....	9
2.3 Objective and key elements of the thesis.....	12
Chapter 3 : Theoretic background.....	15
3.1 Interaction of high energetic particles and matter .....	15
3.1.1 Energy loss of the particle.....	15
3.1.2 Particle range.....	17
3.1.3 Track formation .....	18
3.2 Important units .....	19
3.2.1 Fluence and flux.....	19
3.2.2 Dose .....	19
3.3 Degradation mechanism of polyimide .....	20
Chapter 4 : Experimental .....	22
4.1 Material .....	22
4.2 Dose simulation.....	24
4.3 Experimental approach for the irradiation .....	25
4.4 Ion Radiation .....	26
4.4.1 Irradiation experiments at GSI, Darmstadt, Germany .....	26
4.4.2 Irradiation experiments at GANIL, Caen, France .....	28
4.5 Analytical methods .....	31
4.5.1 Infrared spectroscopy .....	31
4.5.2 UV/Vis spectroscopy.....	35
4.5.3 Tensile strength .....	37
4.5.4 Dielectric relaxation spectroscopy (DRS).....	40
4.5.5 Mass loss analysis .....	44
4.5.6 Residual gas analysis during irradiation.....	45
4.5.7 Residual gas analysis during heat-up cycles .....	48

---

Chapter 5 : Results and discussion.....	51
5.1 Room temperature experiments.....	51
5.1.1 Infrared spectroscopy .....	51
5.1.2 UV/Vis spectroscopy.....	56
5.1.3 Tensile strength .....	59
5.1.4 Dielectric relaxation spectroscopy.....	63
5.1.5 Mass loss analysis .....	76
5.2 Low temperature experiments.....	77
5.2.1 In-situ FTIR spectroscopy .....	77
5.2.2 Residual gas analysis during irradiation.....	79
5.2.3 Residual gas analysis during heat-up cycles .....	81
Chapter 6 : Conclusions.....	85
6.1 Room temperature experiments.....	85
6.2 Low temperature experiments.....	91
6.3 Consequences for the magnet design.....	93
Chapter 7 : Outlook.....	95
7.1 High dose experiment at (HHD) .....	95
7.2 Electrical material properties.....	96
7.3 Cryogenic conditions and the new M3 experimental .....	98
station .....	98
Chapter 8 : Bibliography .....	101
Chapter 9 : Appendix .....	109

# Chapter 1 :

## Introduction

### 1.1 Radiation effects

The investigation of radiation effects on polymer materials started in the 1950s. The interest was basically motivated by two reasons: First, the possibility to modify polymer materials and second, to estimate the radiation hardness of polymers (for their use in high-voltage accelerators, equipment for nuclear reactors, and compounds of space crafts) [1, 2].

In most cases an ionization of the atoms or molecules appears as consequence of the energy entry. This process leads to a positive charged molecule or atom if the transferred energy is greater than the binding energy of an electron. It is also possible that the molecule is excited by e.g. a fast charged particle. The excited molecule reacts under creation of free radicals. The radicals can undergo recombination reactions causing:

- cross-linking - formation of a new bond between two polymer chains
- unsaturation - formation of a double bond
- degradation - breaking of the main polymer chain.

In general, irradiation of polymers like PE, PP, and PS leads to cross-linking while polymers which are totally substituted (PTFE etc.) undergo mainly degradation. An indication for the radiation sensitivity is the G-value defining the number of produced or degraded molecules per 100 eV transferred energy. It is typically measured by using ESR analysis for the determination of radicals [3].

## 1.2 Polymer modification by ionizing radiation

Ionizing radiation permits special possibilities to modify materials. It has become an important tool for the polymer industry. In the following, several techniques for improving polymer properties are presented:

**Cross-linking** of polymer chains generally leads to better material performance. Historically the development starts with the sulphur vulcanisation of rubber. In former times the cross-linking initiation was assumed to be possible only by addition of chemical agents. But in the middle of the 1950s Charlesby reported about successful cross-linking of polymer chains by ionizing radiation [4-7]. It was also found that even polymers without reactive functional groups can be cross-linked by ionizing radiation [8]. Great advantages of performing cross-linking without chemical agents are the reduction of costs, reaction temperature and reaction time. Additionally, the abdication of chemicals leads to a clean, solvent free product and lowers chemical waist. Today the cross-linking by ionizing radiation is state-of-the-art for a large variety of polymers like latex, silicone, PMMA/ABN blends etc [8-11]. It is used for heat and cable insulation in the automotive industry [12] and especially the cable insulation of high performance applications in the aircraft and aerospace industry using cross-linked PE and PVC cable insulators. Cross-linking can also help to produce special blends which normally undergo phase-separation.

In general, polymers can be grouped in such that are cross-linked and such that primarily undergo chain scission under radiation. But by choosing special radiation conditions also polymers, which normally react with chain scission e.g. PTFE, can be cross-linked by irradiation [13]. Polymeric spheres and particles in the micron and sub-micron range can be irradiated as emulsions containing one or more monomers leading to a new cross-linked polymeric system [14].

Another field of application using the principle of radiation induced polymerisation is **curing of coatings and inks**. It is mainly applied in the graphic arts and packaging industry [15]. The advantage of the electron-beam (e-beam) is, that it provides a high efficient, fast, energy saving and solvent free [16] method of curing also through a heavily pigmented coating. Problems of the process appear due to the required inert atmosphere during irradiation. It has to be noted that nowadays many applications deal with UV irradiation instead of the E-beam if only a short penetration depth is required.

The combination of radiation induced cross-linking process with the so-called “memory effect” is also used for application. Primarily polyethylene-based heat shrink materials are established for food wraps and tubing of electric wires. The crystalline regions of the radiation cross-linked polymer are molten when the polymer is stretched. Afterwards the polymer is rapidly cooled down by keeping its stretched structural position. The quenching procedure leads to a meta-stable, elongated form of the material. If the polymer is now heated again it shrinks to its original size [17].

The E-beam induced cross-linking is also used to produce **fibre-matrix composites**. The advantage in contrast to the temperature induced hardening is the lower process temperature which eliminates internal stress and allows shorter curing times [18].

Another broad field is the **surface modification** by radiation treatment. Radiation takes often place under presence of a reactive gas ( $O_2$  or  $NH_3$ ) to introduce polar surface groups [19]. Especially low-energy ions and electrons have a small penetration depth which leads to the possibility to modify the surface while keeping the properties of the bulk material. In principle, radiation allows the increase or decrease of surface roughness. With high-intensive beams it could be shown that polytetrafluoroethylene (PTFE), polycarbonate (PC), and polyimide can be turned into microcellular foam [20]. It is also possible to create polymer-metal interfaces by means of irradiation [21].

Radiation induced **grafting** is also a well established technique which is frequently used for industrial applications [22]. It allows the synthesis of materials with different properties concerning the bulk material and the surface. Normally a material with good mechanical strength and low costs is chosen as bulk substrate onto which a second polymer with the desired properties is “grown”. By means of irradiation, bulk material with a large amount of free radicals is created in the surface layer. These activated sites react e.g. with a specific monomer forming a “grafted” surface [23]. The grafting process could be performed directly or simultaneously during the irradiation. In this case a solution of the monomer is present during the irradiation (an inhibitor avoids homo-polymerisation). Alternatively the process can be initiated after irradiation applying the “preoxidation” method where the material is irradiated in the presence of air and the monomer is attached afterwards. The applications of

grafted materials range from immobilisation of enzymes for organic synthesis [24], substrates for analytical chromatography [25], filter membranes for heavy metal ions [26] to the general increase of biocompatibility of polymers [27].

The radiation induced cross-linking is also used to produce **hydrogels**. Hydrogels are three-dimensional structured networks of hydrophilic polymers which have the ability to absorb a large amount of water [28]. They are mostly used in biomedical applications e.g. wound dressing, soft contact lenses, drug delivering systems, and artificial skin [29]. The fabrication of hydrogels applies the radiation at one side for the cross-linking as well as for sterilisation.

The **radiation sterilisation** of plastic medical items is also a common industrial technique. The major benefit of the use of radiation instead of chemical solutions is the elimination of toxic residue at the product [30].

Radiation treatment of polymers is suitable for **plastic recycling**. Decomposing of waste polymers by chain scission leads to a mixture of low molecular weight polymer. Alternatively cross-linking of waste polymers is another way of “recycling” by producing e.g. recycled polymers with enhanced mechanical properties [31].

A special application of energetic heavy ions is based on the ion track technology, where MeV-GeV ions produce latent tracks inside the polymer [32, 33]. The track zones are characterised by a strong physical and chemical material modification. Ion irradiated polymer films can be treated with organic solvents of strong acids or bases to etch or dissolve preferentially the tracks [34]. The process of **etching ion tracks** provides a tool to tailor the polymer on a nanometre scale e.g. to build filters or template structures. Especially the formation of nanopores or the growth of nanowires in porous templates is very interesting [35-37].

The degradation of polymers induced by ionizing radiation is used to provide micro-powders with low molecular weight. Therefore the **chain scissoring** mechanism especially for PTFE is commercially established [38].

### 1.3 Radiation hardness of polymer materials

In the past five decades, the interest of radiation hardness of polymers increased significantly with respect to their application as insulators in high radiation environment such as nuclear power plants and particle accelerators [39-41]. The proper function of devices is often limited by radiation induced problems of polymeric insulators. On the other hand, compared to metals or ceramic materials, polymers are often necessary because of their excellent processability and insulating properties.

A great contribution concerning radiation hardness tests for insulating materials has been done at CERN (Conseil Européen pour la Recherche Nucléaire). The studies focused in particular on cable insulating materials [42, 43] exposed to neutrons and gammas. The real radiation conditions of a material located close to the beam tube of a particle accelerator were simulated by reactor radiation (for neutrons) and gamma irradiation by a Cobalt-60 source. The material analyses were restricted to mechanical tests (mainly tensile strength tests) which just give limited information with respect to radiation damage (Figure 1).

In the 1980s, the tests at CERN were extended to new polymer materials and to electrical tests [44]. Also dose-rate effects were analysed but again the radiation sources were limited to neutrons and gammas [45, 46]. A further study analysed degradation not by direct irradiation but by positioning the samples close to the beam line in order to get a more realistic impression of the fragment spectra caused by beam losses of the primary beam [47]. Only a few very general studies focus on the degradation problems which appear at cryogenic temperatures [48-52].

Nowadays, many research groups analyse polymer degradation after irradiation with different kinds of particle radiation including light and heavy ions in a large energy regime from keV to GeV [53-57]. To understand the degradation mechanism various techniques such as optical spectroscopy, microscopy, nuclear magnetic resonance spectroscopy (NMR) [58], and electron paramagnetic resonance spectroscopy (EPR) are applied [59-61].

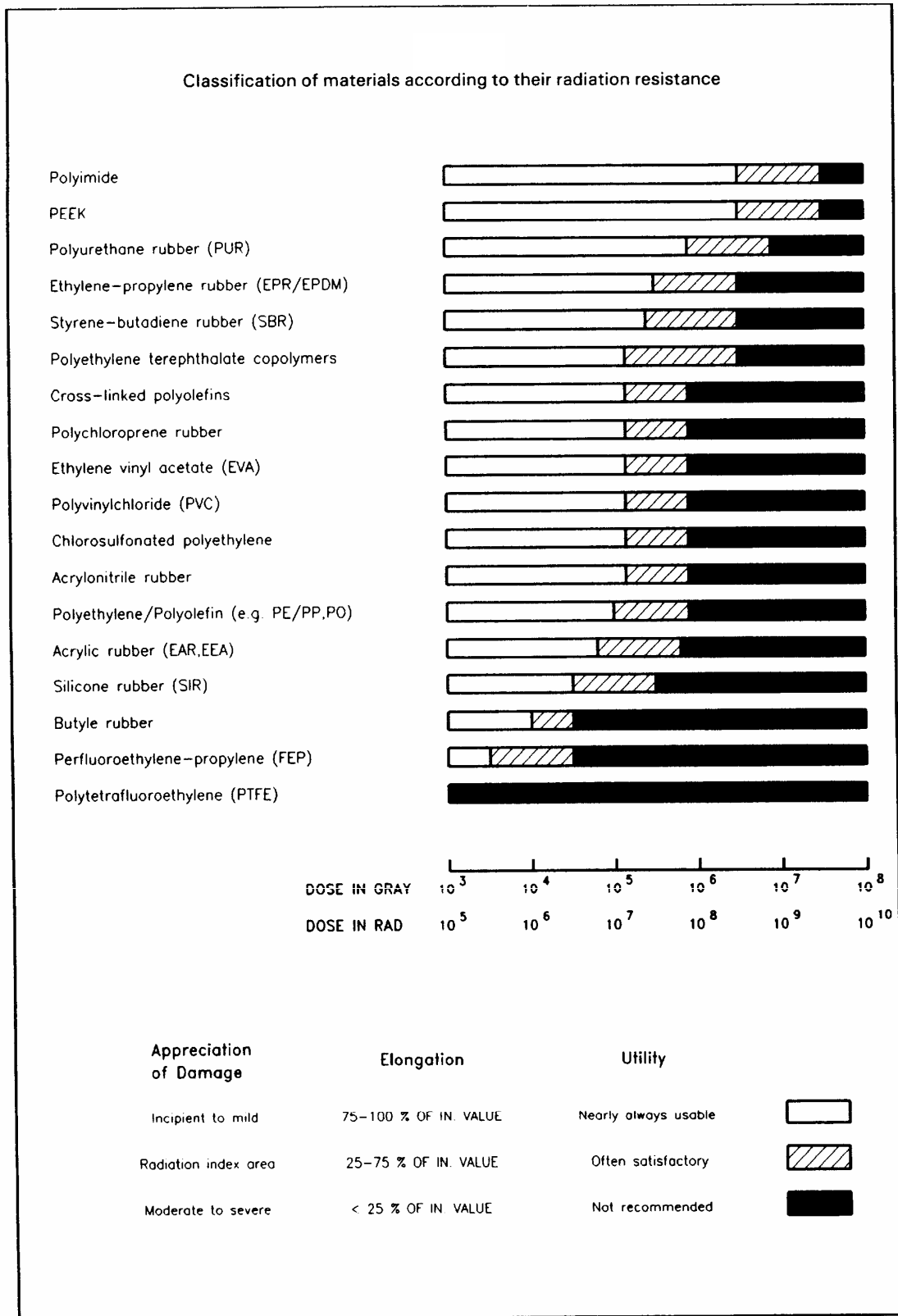


Figure 1: General radiation stability table taken from the CERN Report [62]

## Chapter 2 :

# Motivation

### 2.1 FAIR project

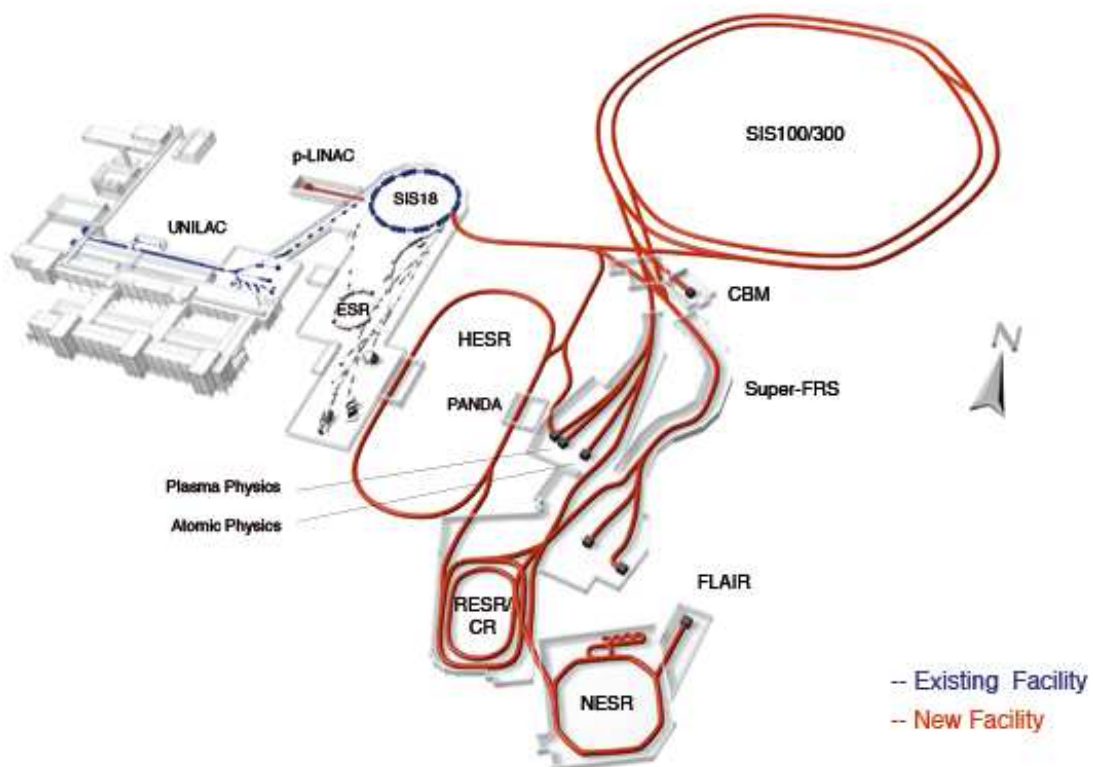
The Gesellschaft für Schwerionenforschung (GSI) in Darmstadt, Germany plans the new accelerator facility FAIR (Facility for Antiproton and Ion Research) for studying the matter at the level of atoms, atomic nuclei, protons and neutrons as the building blocks of nuclei and hadrons [63]. A closer focus will also be set on the sub nuclear constituents called quarks and gluons. With this new project, GSI will provide an accelerator and experimental facility for novel experiments in fields of hadron, nuclear, atomic, and plasma physics [64].



Figure 2: Aerial photo of the existing GSI (left) and a virtual view of the planned FAIR facility (right)

Areas of research are e.g. plasmas existing in the interior of large planets, the formation of nucleons, the quark-gluon-plasma, and the formation of elements larger than iron. The FAIR project will be built in cooperation with their users and the international community. The heart of the new facility consists of two superconducting double ring synchrotrons with a circumference of about 1100 m [65].

The existing GSI accelerators (linear accelerator UNILAC and heavy ion synchrotron SIS18) will serve as injectors. The new facility will deliver ion beams of unprecedented intensities and energies. Especially secondary beams of unstable nuclei or antiprotons can be produced. A system of different storage-cooler rings allows to increase the quality of these secondary beams in terms of energy spread and emittance.



**Figure 3: Drawing of the planned FAIR facility**

Moreover, in connection with the double ring synchrotron, an efficient parallel operation of up to four scientific programmes can be realized at a time. The

project is based on many technological innovations, and expects to provide the following beams:

- for the radioactive beam production, primary beams of about  $1 \times 10^{12}$  U ions/s at energies from 400 to 1000 MeV/u either with a long duty cycle (~100 %) or in short bunches with pulse lengths from 50 to 100 ns
- for the antiproton facility,  $2.5 \times 10^{13}$  protons per pulse at 29 GeV every 5 s
- for plasma physics research at least  $1 \times 10^{12}$  U ions in a single short bunch (100 ns / 50 ns) at 400 to 1000 MeV/u
- for a research programme with high-energy heavy-ion beams, e.g.  $1 \times 10^9$  U ions/s at 22 GeV/u.

## 2.2 Magnet design

To provide such enormous energies and intensities a set of specific preconditions concerning the accelerator facility and the magnets is required [66]:

- The existing UNILAC has to be upgraded as injector and a new proton linear accelerator (50 or 100 MeV) is needed for providing high intensive proton beam for the  $p^-$  production.
- The existing synchrotron SIS18 has to be modified to operate as a fast-ramp booster synchrotron with four machine cycles per second (SIS12 mode).
- The new synchrotron SIS100 needs fast-ramped superconducting magnets designed for  $B_p = 100$  Tm,  $B_{\max} = 2$  T, and  $dB/dt = 4$  T/s, to accelerate heavy ions, e.g.  $U^{28+}$  ions to 1000 MeV/u (at  $B_p = 50$  Tm) and also for the protons to 30 GeV (at  $B_p = 100$  Tm).
- A second synchrotron SIS200 in the same ring tunnel with superconducting high-field magnets is designed for  $B_p = 200$  Tm,  $B_{\max} = 4$  T, and  $dB/dt = 1$  T/s for the acceleration of bare  $U^{92+}$  ions to 22 GeV/u and also for the operation as stretcher ring to provide  $U^{28+}$  ions between 400 and 1000 MeV/u with a long duty cycle of about 100 % at maximum beam intensity ( $1 \times 10^{12}$  ions/s).

The magnets of such a large synchrotron make up a major portion of its costs. Therefore, a careful choice of the magnet design must be made at a very early stage of a new project. Today, it is a standard accelerator technology to use superconducting high field magnets (4 to 9 T) in high energy proton or heavy-ion colliders. But the difference concerning the requirements is that these machines are traditionally run at low ramp rates ( $< 0.1$  T/s). As the FAIR facility requires fast ramp rates of 1-4 T/s, low field superconducting dipoles (2 to 4 T) must be considered as the most suitable ring magnets since they keep the stored magnet field energy low. The following magnet types are proposed for the new synchrotrons:

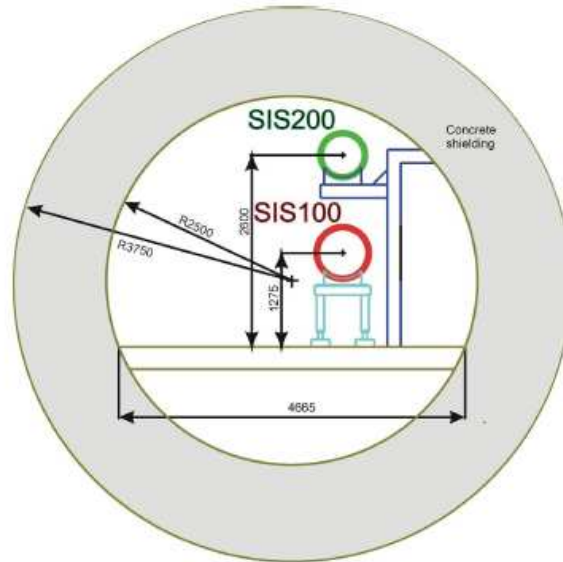


**Figure 4: Tunnel cross section of SIS100/200 synchrotrons of the FAIR accelerator facility**

**The Nuclotron type** is an iron-dominated magnet which seems to be the best choice for SIS100. A cross section of the dipole (maximum field: 2 T) is shown in Figure 5. The superconducting coil has an indirectly cooled hollow pipe conductor with superconducting NbTi-wire wound around the pipe. The magnet operates at 4.5 K. Both, iron yoke and beam tube are cold. The Nuclotron magnets have been operated successfully in a synchrotron at the JINR in Dubna, Russia since 1993, their nominal ramp rate is 4 T/s. The new accelerator is based on this design but some modifications are needed to improve the field quality, to reduce the loss, and to increase the mechanical stability.

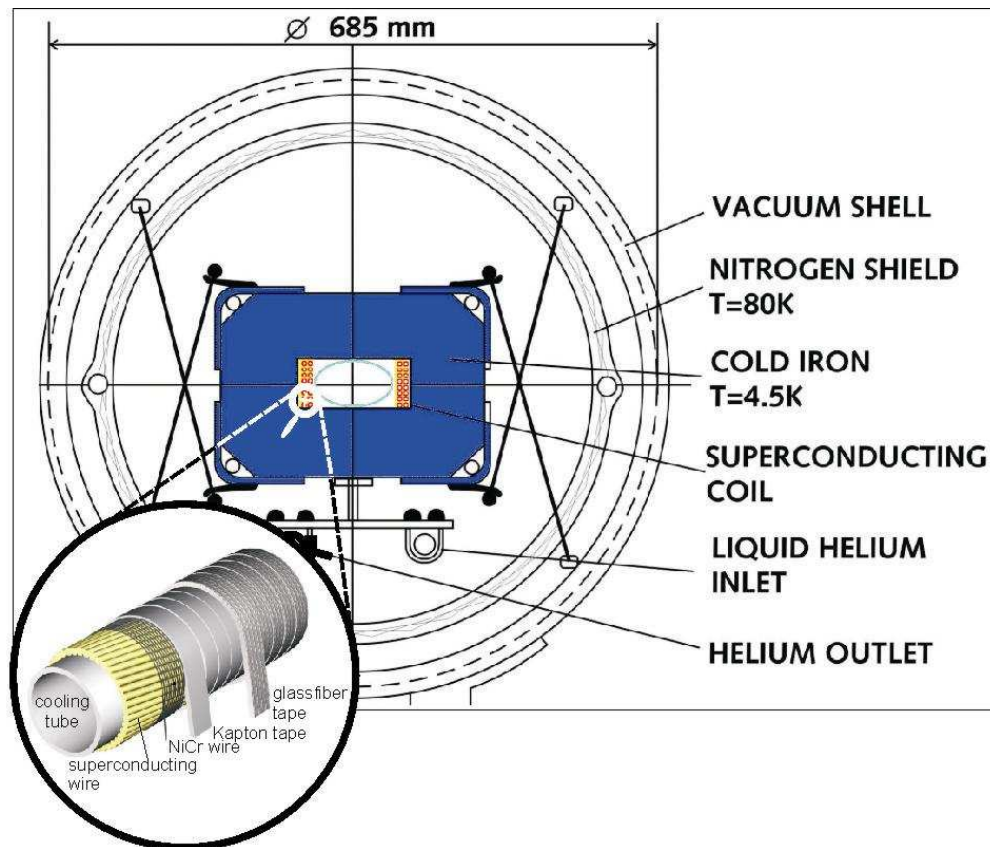


**Figure 5: Cross section of the nucletron magnet for the SIS100**

For the SIS200 Coil-dominated magnets of the  $\cos\theta$  type are planned similar to the magnets of the RHIC facility. A cross section of the **RHIC arc dipole** with a magnetic field of up to 4 T is shown in Figure 6. The coil has only one layer. The most likely conductor candidate is a standard Rutherford cable consisting of NbTi filament embedded in a Cu matrix. The complete magnet with the cold bore is also operated at 4.5 K. The RHIC-type magnet allows operation at higher fields. Further studies, using an advanced Rutherford cable, are required before a magnet of this type can operate at high ramp rates with reasonable loss and with adequate field quality, achieved by control of the persistent/eddy current effects.

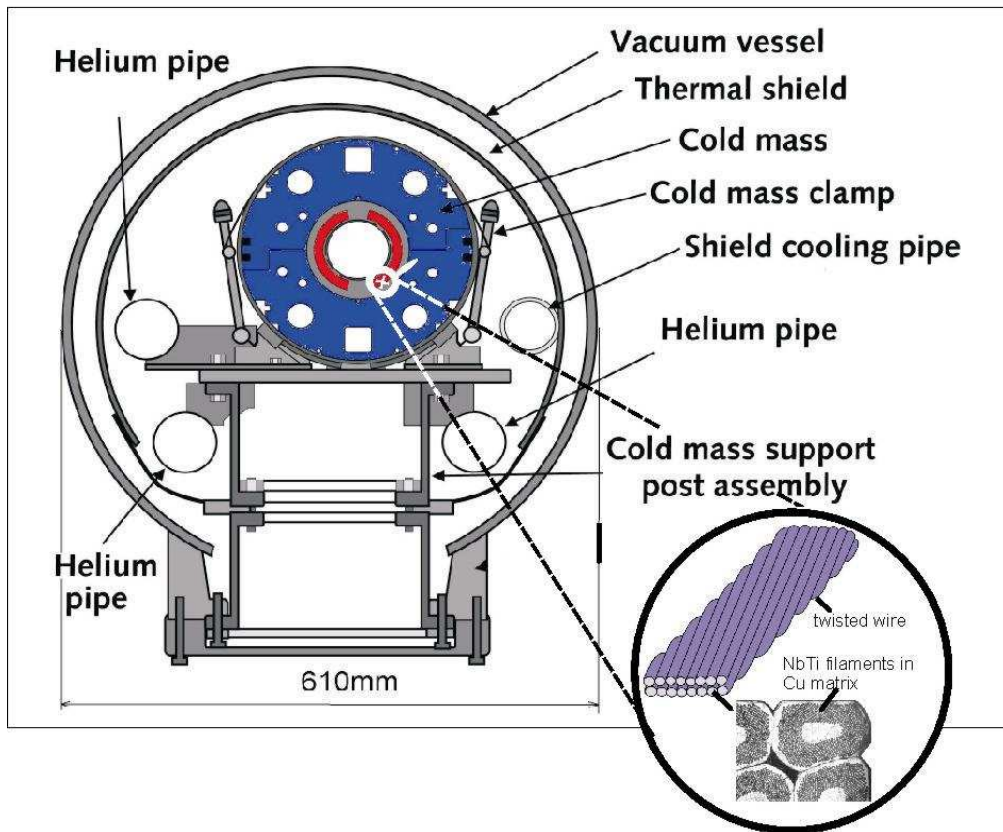


**Figure 6: Cross section of the RHIC arc magnet for SIS200**

The two magnet types provide different magnetic fields: The nucletron type reaches only 2 T in contrast to the 4 T of the RHIC arc magnets. The disadvantage of the RHIC arc magnet is the low iron content of the coil (35 %) which leads to higher losses and persistent currents being critical at low fields. In addition, the conductor positioning is much more critical, because it is not in close contact with an extra cooling tube so helium containment is necessary.

### **2.3 Objective and key elements of the thesis**

The study is directly linked to the large beam intensities of the FAIR project and the radiation hardness of the insulators involved in the superconducting magnet design. One advantage of this type of magnets is the smaller size in comparison to normal conducting magnets, which allows a more compact design. The more compact geometry and the planned high intensive beams will result in an enormous increase of the radiation level exposing materials close to the beam tube to high doses. This high radiation level is mainly caused by beam loss

processes where ions of the primary beam hit the beam wall. The fragmentation of the primary particles leads to a cocktail of radiation including gammas, protons, and neutrons but also heavier ions which enter into the magnet parts behind the beam tube.

While metallic materials exhibit rather good radiation hardness, polymer materials, e.g. insulators such as polyimide (Kapton) and fibre reinforced plastics (FRP) based on an epoxy polymer are exposed to a high risk of material breakdown. Especially the mechanical degradation and the failure of its insulation function are critical material properties which are influenced by radiation.

In this study the radiation hardness of Kapton as primary used insulating material of the superconducting magnets is tested and dose limits for life-time estimations are studied. Together with beam loss simulations, these limits can serve as safety margins for the operation of the new FAIR facility.

Furthermore the effect of irradiation concerning the material changes is still not totally understood. The role of high energetic particles as irradiation projectiles is not fully clarified in contrast to radiation experiments with gamma and neutron radiations. Therefore, the structural disintegration and transformation from a mechanically stable insulating polymer to an instable conductive carbon network has to be investigated as a function of radiation dose.

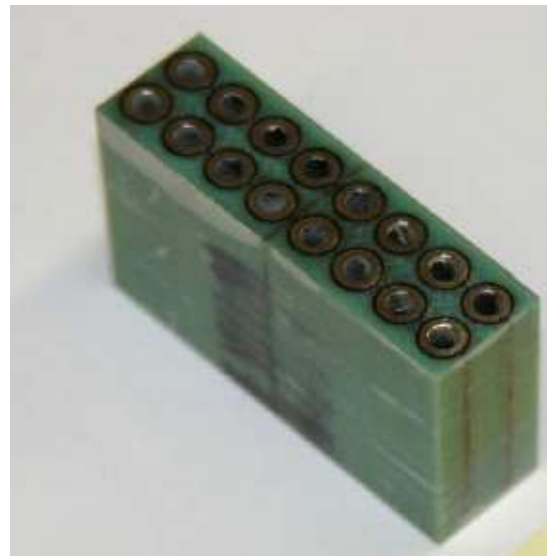


**Figure 7: Cross section of the nucletron magnet coil embedded in a FRP structure contains 16 Kapton-insulated cooling tubes wrapped with sc wires.**

For a first dose estimation, the experiments concentrate on irradiation with swift heavy ions to create a worst case scenario by depositing high energies into the material with a projectile range which extended the sample thickness. Therefore material irradiations with a variety of different heavy ions have to be carried out. It should point to a critical dose level with respect to the important material properties. For the intended application later on, especially the mechanical and electrical properties are of great interest. The project is also motivated to find a

correlation between fast and non destructive methods like optical spectroscopy which characterize the material degradation and the material changes concerning the macroscopic material properties followed by more complex analytical techniques. Additionally, the correlations would make it possible to transfer material degradation data of the literature.

Furthermore, the aspect of the working temperature of 4.5 K should be taken into account for the degradation analysis. Therefore the outgassing behaviour and the gas accumulation at low temperatures of the material have to be analysed. To verify the outgassing behaviour, in-situ analysis, i.e. online measurement during the irradiation by means of residual gas analysis, is necessary. Furthermore, the accumulation at low temperatures of some gases can be followed by transmission infrared spectroscopy.

## Chapter 3 :

# Theoretic background

### 3.1 Interaction of high energetic particles and matter

Focusing on the interaction of high energetic heavy particles and matter, the fact of a single particle depositing a large amount of energy in a localized small volume element of the target needs to be taken into account. This is the main difference to low ionizing radiation like gammas, X-rays, and UV light, where a homogenous dose deposition occurs.

The penetration process of a charged high energetic particle in condensed matter can be characterised by its trajectory. Along its way, the ion is slowed down and loses energy under formation of a so-called “latent track” [67]. The energy loss of the ion is defined as  $dE/dx$  which changes depending on the ion range.

#### 3.1.1 Energy loss of the particle

The energy deposition of an energetic particle is correlated to its velocity and mass and is dominated by two parts:

- **the electronic energy loss ( $dE_{el}/dx$ )**

The high velocity of the projectile particle leads to excitation and ionization of the target atoms. In a first stage energy is transferred from the projectile to single target electron. Afterwards, occurring electronic collision cascades, so-called delta electrons, distribute the energy along the trajectory. The range of these delta electrons can go up to  $1\mu\text{m}$ . Finally the remaining

positive charged ions in the trajectory undergo an expansion by Coulomb repulsion. These atomic collision cascades have a by far smaller range in the order of a few nanometres and ending up in displaced and/or excited atoms (point defects). The energy loss increases with the penetration depth having a maximum at a certain range called Bragg peak.

- **the nuclear energy loss ( $dE_n/dx$ )**

When the projectile had lost a lot of its energy the electron shell of the target atoms could no longer be penetrated. So the projectile loses its residual energy by elastic collisions with the target atoms, whereby a direct transfer of energy and momentum occurs. The transferred momentum leads to new energetic particles which start their own slow down cascade.

The total energy loss is the sum of both parts electronic and nuclear energy loss. Due to the fact that the discussed experiments are within the MeV and GeV regime the nuclear energy loss is negligible in contrast to the electronic part. So in the following, the energy loss is expressed only by the electronic energy loss which is defined by the Bethe-Bloch equation [68, 69]:

$$\left(\frac{dE}{dx}\right)_{el} = \frac{4\pi e^4 Z^{*2} Z_t N}{m_e v_p^2} \left[ \ln\left(\frac{2m_e v_p^2}{I}\right) - \left(\frac{v_p}{c}\right)^2 - \delta - U \right] \quad (1)$$

$Z^*$ : mean charge state of projectile

$Z_t$ : mean charge of target

$e$ : elementary charge

$m_e$ : electron mass

$N$ : atom density of target

$v_p$ : projectile velocity

$I$ : mean ionisation energy of target atoms

$c$ : speed of light

$\delta$ : relativistic correction (taking into account polarisability of target)

$U$ : correction due to the inner shell electrons of target

The Bethe-Bloch equation indicates that the deposited energy is proportional to the square of the mean charge state of the projectile which is proportional to the atomic number and to the projectile velocity.

### 3.1.2 Particle range

The particle range is given by

$$R = \int_0^R \left( \frac{dE}{dx} \right)^{-1} dz \quad (2)$$

To estimate energy loss and ranges, various codes are available. Here the SRIM2006 (Stopping and Range of Ions in Matter) code is used [70]. The code is mainly based on the law of Bragg taking into account the stopping power of the target atoms notwithstanding their molecular structure (binding properties). Figure 8 shows a calculated ion trajectory concerning the electronic energy loss of the projectile.

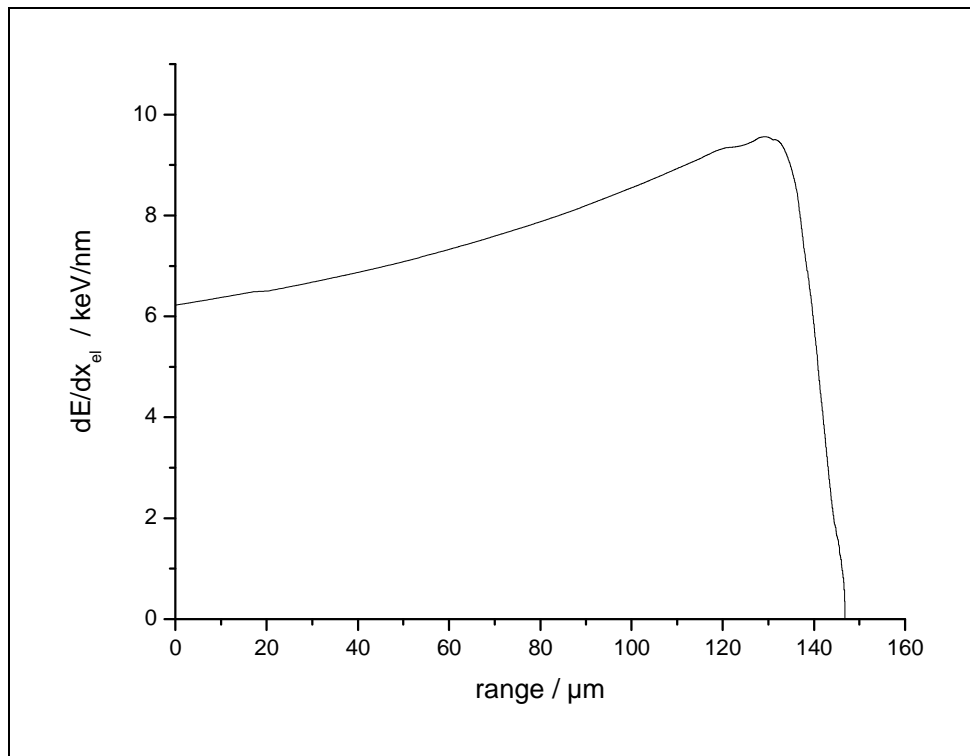


Figure 8: SRIM calculation of a Mo ion of 11.4 MeV/u in polyimide

### 3.1.3 Track formation

The track formation is sub-divided into two stages: In the first femto seconds energy transfer occurs on the atomic level meaning excitation and ionization of molecules and atoms when the charged projectile traverses the solid. Afterwards on the pico seconds scale secondary electron cascades produce further ionisation in the trajectory area. In a second stage the energy is transferred to the atomic system leading to defect creation in terms of amorphisation and/or bond breaking. Especially polymers with their hydro carbon matrix react under formation of high excited unstable molecules. Mostly, radicals stand at the end of relaxation paths which results in homolytic bond breaking.

The primary mechanism of track formation is not understood completely yet. There are two basic models describing the phenomena: the Coulomb explosion model and the Thermal-spike model [71, 72].

The Coulomb explosion model explains the track formation based on the high ionisation along the ion path. The remaining positive charged atoms and molecules reject each other leading to the Coulomb explosion. This process is the driving force for atomic collision cascades.

The Thermal-spike model assumes that the atomic collision cascades induced by the energy deposition of the projectile initiate a temperature increase in a small cylindrical volume surrounding the ion track. The local high temperature leads to heat diffusion which creates defects. These so-called frozen defects are based on fast quenching processes due to the very high temperature gradient.

## 3.2 Important units

### 3.2.1 Fluence and flux

The fluence ( $\Phi$ ) defines the particles per unit area. It is normally addressed to one square centimetre. This unit is used to quantify the number of ions as measured during the irradiation experiment.

$$\Phi = \frac{N}{A} \quad \left[ \frac{\text{ions}}{\text{cm}^2} \right] \quad (3)$$

The flux describes the particle per unit area and time, representing the beam intensity.

$$\frac{d\Phi}{dt} = \frac{\Phi}{t} \quad \left[ \frac{\text{ions}}{\text{cm}^2 \cdot \text{s}} \right] \quad (4)$$

### 3.2.2 Dose

The dose  $D$  has its origin in the field of classic radiation chemistry and defines the energy deposited per mass unit of the target material.

$$D = \frac{E}{m} \quad \left[ \frac{\text{J}}{\text{kg}} = \text{Gy} \right] \quad (5)$$

For the conversion of the fluence into the dose, it is necessary to implement information of the beam energy and target material. For this, the amount of energy ( $\Delta E$ ) which is deposited into a defined volume of the target has to be calculated. Therefore the computer code SRIM 2006 [73] is used to estimate the energy loss ( $dE/dx$ ) depending on the particle energy and sample density. The total energy can be calculated by integrating the energy loss  $dE/dx$  over the projectile range or the penetration depth ( $d$ ) in a given target.

$$D = \frac{e \cdot \Delta E \cdot \Phi}{d \cdot \rho} \quad (6)$$

e: elementary charge

$\Delta E$ : deposited energy

$\Phi$ : fluence

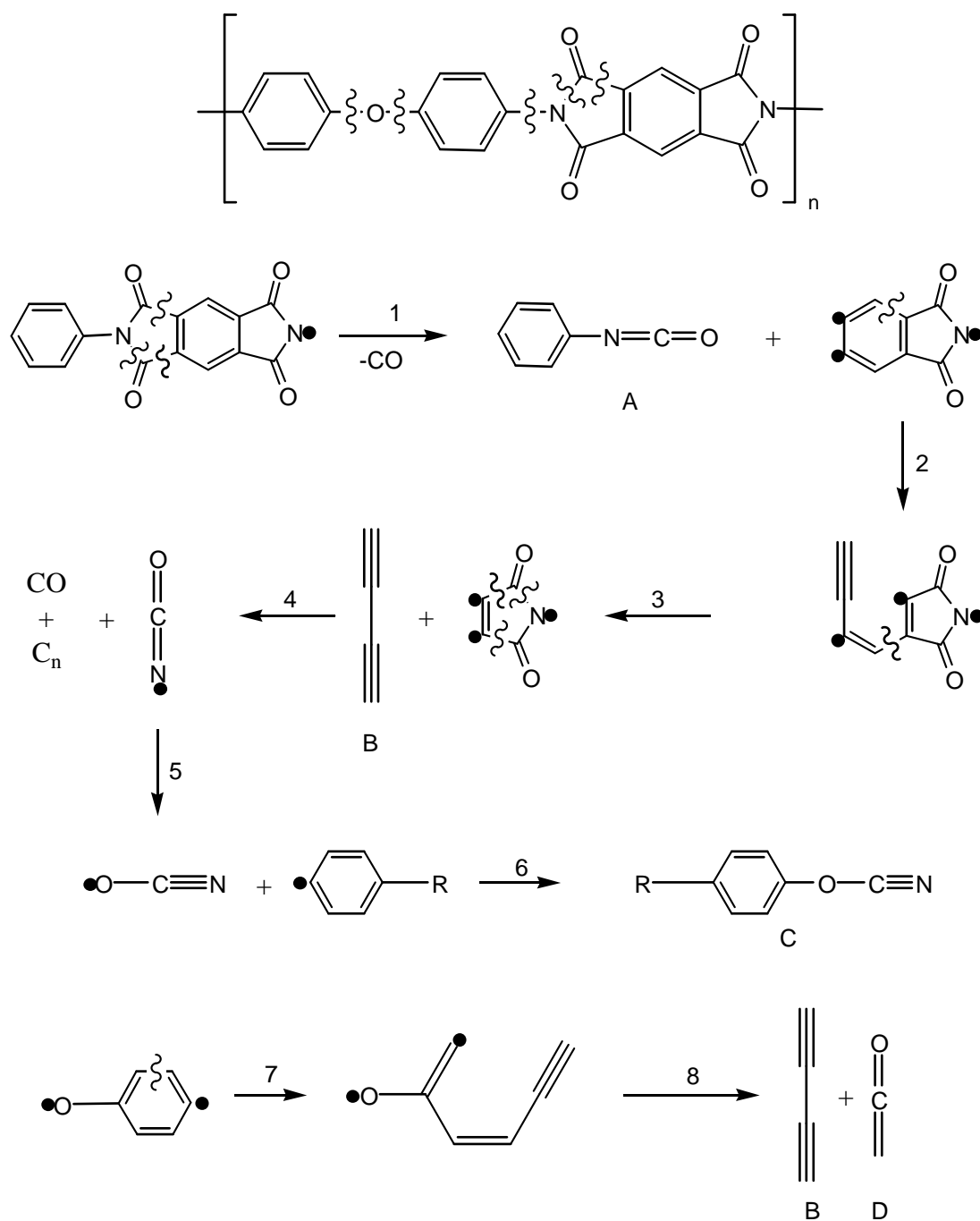
d: penetration depth

$\rho$ : target density

### 3.3 Degradation mechanism of polyimide

The described energy entry into the polymer induced by high energetic ion irradiation leads to a drastic material degradation. In the literature, a degradation mechanism is postulated which is deduced from degradation processes induced by high temperature or gamma radiation (Figure 9) [74].

The degradation process is initiated by homolytic bond breaking. In the first step a phenyle diradical and phenyle isocyanate (A) is formed under elimination of carbon monoxide. The diradical decays in two steps to butadiene (B) and a diradical imide group. Within step 4 the imide radical decomposes to carbon monoxide, graphitic carbon, and isocyanate radical. After a rearrangement of the isocyanate radical it reacts with a phenyl radical and forms the degradation product C. Alternatively, the phenyl radical may degrade (step 7 and 8) to butadiene (B) and to the ketenal (D).



$\curvearrowright$  = homolytic break

Figure 9: Proposed degradation mechanism of polyimide

# Chapter 4 :

## Experimental

### 4.1 Material

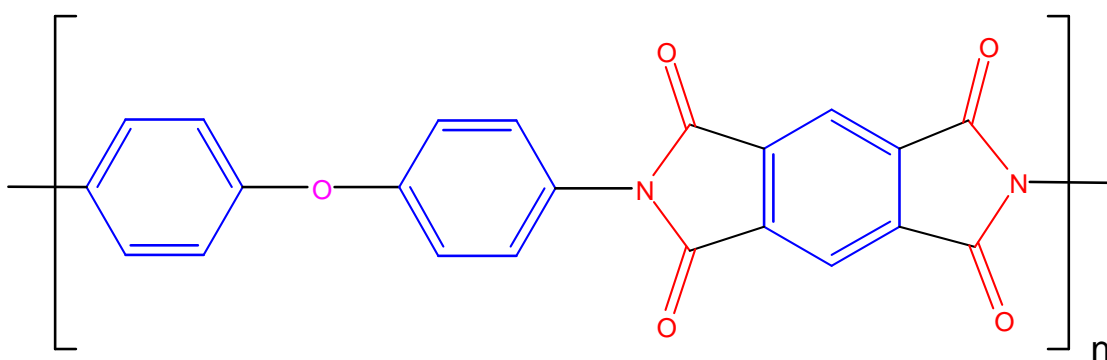
Polyimide is deemed to be one of the most radiation stable polymers. Additionally it has outstanding material properties which make polyimide to the most popular high performance polymer. Polyimide foil was established by DuPont under the trade name Kapton and is used mainly in the high tech industry e.g. in the aerospace, computer and automotive industry. Due to its very good mechanical and thermal properties (stable from 4 to 674 K) Kapton is often used as insulating material for the board production in the chip industry. Furthermore Kapton shows a very good resistance against organic solvents, acids and bases. Detailed information of the material properties are given in Table 1 [75].

Polyimide is produced in a bi-polycondensation reaction were 1,2,3,4,5-Benzotetracarboxylic dianhydride (Pyromellitic Dianhydride (PMDA)) and 4,4'-Diaminodiphenylether form *N,N'*-(p,p'-oxydiphenylene) pyromellitimide ( $C_{22}H_{10}O_5N_2$ )<sub>n</sub> which is in the following simply described as polyimide or Kapton.

**Table 1: Material properties of Kapton**

Density:	1.42 g/cm <sup>3</sup>
Melting point:	No melting
Glass transition temperature:	360 – 410 °C (2. Order)
Thermal conductivity:	0.12 W/m K
Tensile strength (max.):	231 MPa
Dielectric strength:	303 V/μm
(at 60 Hz; 6 mm electrodes with 500 V/s )	
Dielectric constant: (at 1 kHz)	3.4
Resistivity:	1.5x10 <sup>17</sup> Ω cm

Figure 10 shows the chemical structure of polyimide. It is characterised by two imide groups (red) which are connected via a phenyl ring (blue). Two more phenyl groups linked over an ether function (pink) are bonded to the nitrogen. The high radiation resistance and high temperature stability is given by the large  $\pi$ -system of the polymer. In combination with the hetero atoms the molecule has a high ability to transfer energy within the electronic system. This leads to an even distribution of the energy so that the local amount of energy is below the binding energy and does not induce bond breaking.

**Figure 10: Structure of polyimide**

For the study, Kapton HN from DuPont with different thicknesses of 12, 25, and 50 μm depending on the analytical method were irradiated.

## 4.2 Dose simulation

To get a rough estimation of the dose which beam losses will produce inside the superconducting magnets, calculations were performed using the transport code SHIELD [76]. This Monte Carlo code is used for simulations of high energetic charged particles transported in condensed matter. Here the code simulates one uranium ion which leaves the primary beam and hits the inner beam tube wall under an angle of 17 mrad with 1 GeV/u. The code considers the interaction of the U ions with the beam tube (stainless steel) including generation and transport of secondary particles and production of radio nuclides [77].

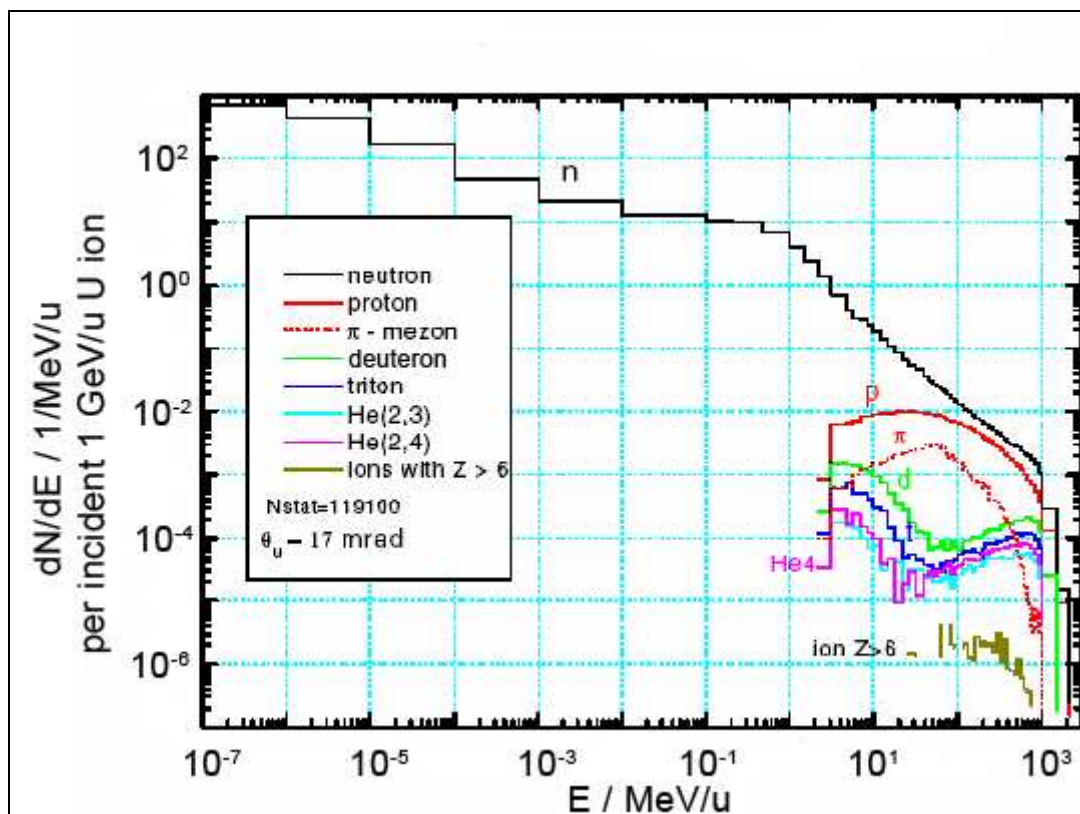


Figure 11: Spectra of particles entering into the insulator and superconducting wire zone of the SIS100 dipole magnet [78].

Figure 11 shows an energy spectrum for different fragments in the region of the insulators which surround the superconducting wires. In the calculations, the energy for the particles except for neutrons is cut off at 3 MeV/u because the ranges of these particles are negligible. The high energy tail of the spectra exceeds the energy of the incident ion (1 GeV/u) due to secondary processes. Especially the neutron spectrum is extended over the full range of the energy

scale and ends up at 2 GeV/u. The proton spectrum rises to a maximum at 250 MeV/u in contrast to the light ions (deuterium, tritium and helium ( $^3\text{He}$ ,  $^4\text{He}$ )) which show two maxima. The low energetic peak at 3 MeV/u is correlated to fragments of the target nuclei. The second peak at higher energy is due to the fragmentation of the projectile nuclei.

Around one per mille of ions with a Z larger than 6 occur in an energy regime between 100 and 1000 MeV/u induced by one uranium ion with 1 GeV/u hitting the beam tube. The ratio of these larger fragments is very small but it must be noted that these particles are responsible for more than 70% of the deposited energy in the polymer material due to their much higher energy loss values in comparison to the light ions (helium, proton) and especially neutrons [79].

### 4.3 Experimental approach for the irradiation

The dose simulations show that fragments with a Z larger than 6 are mainly responsible for the deposited dose inside the insulation materials even if their probability to penetrate the beam tube is low. So the study focused on ion beam irradiations with energies around 10 MeV/u with regard to the availability of beam. Furthermore the projectile mass region between 50 and 238 is intended to be represented.

The beam loss factors of the beams that have been used later on, are not sufficiently clarified which caused that the total dose deposit inside the magnets, even with the fragmentation calculations, could not be estimated in detail. Thus the dose for simulating the life-time irradiation of the magnets is not given. Consequently the irradiation parameters in this study are chosen in a way that the trend of material degradation depending on the dose can be followed. This approach gives a more general access to degradation phenomena in contrast to simple one point material limit tests.

## 4.4 Ion Radiation

### 4.4.1 Irradiation experiments at GSI, Darmstadt, Germany

The Gesellschaft für Schwerionenforschung (GSI) in Darmstadt, Germany operates a particle accelerator which consists of a universal linear accelerator (UNILAC) and a heavy-ion synchrotron (SIS) [80]. The ion sources, located in the front-end of the UNILAC, deliver any nuclide from hydrogen up to uranium with energies in the keV region [81]. The ions produced by the different sources are accelerated by the 120 m long UNILAC up to 11.4 MeV/u which is equivalent to about 20% of the speed of light. At a rate of about 1 Hz the ion beam (1 %) is injected to the heavy-ion synchrotron which further accelerates the ions up to 1.3 GeV/u corresponding to about 90 % of the speed of light. After the heavy-ion synchrotron the high energy beam is either extracted to one of the experiments or can be transported to the experimental storage ring (ESR). Due to the accelerator structure, GSI provides a discontinuous beam with a pulse structure. The normal beam mode for the UNILAC experiments (parasite beam) is 5-50 Hz with pulse durations of 2-10 ms.

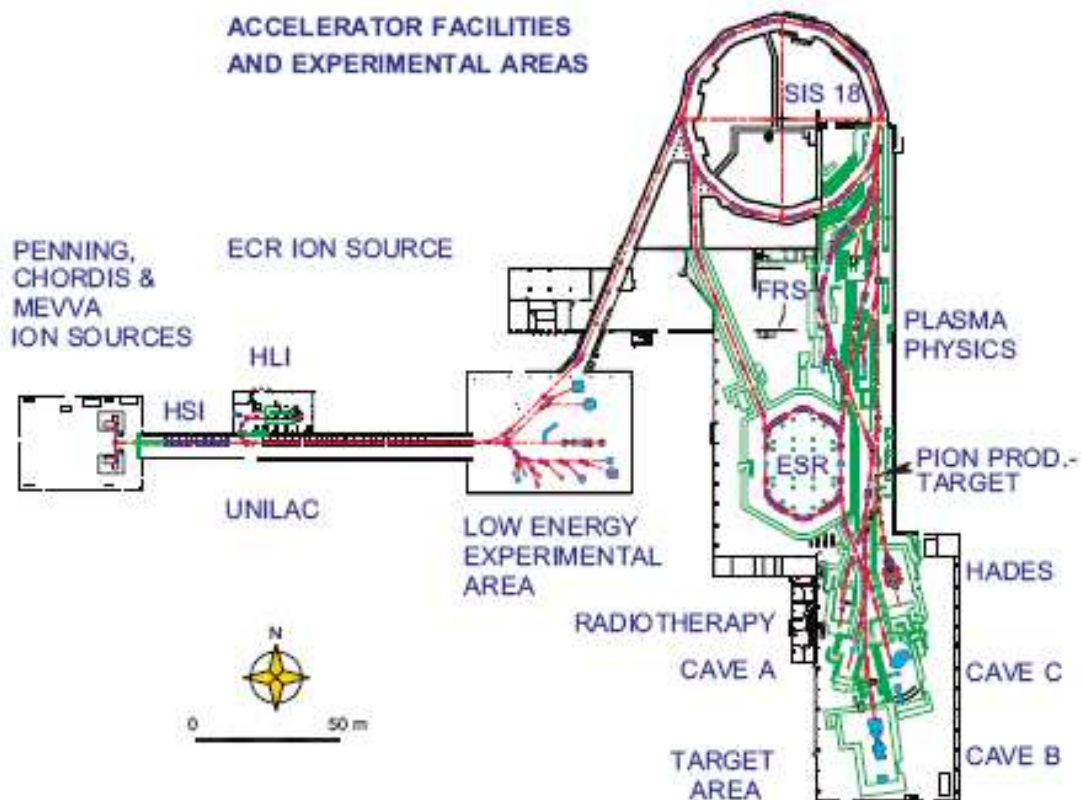


Figure 12: GSI accelerator facility

The irradiations were carried out at the cave X0 situated in the UNILAC experimental hall. The beamline provides a sample exchange system to irradiate, operated by remote control, up to twenty sample holders with respective a size of  $5 \times 5 \text{ cm}^2$ . After passing the beam diagnostic system (three-foil detector) the energy decreases to  $11.1 \text{ MeV/u}$ . The three-foil detector has to be calibrated by a Faraday cup which measures the absolute charge of the impinging ions. This measurement delivers the flux with respect to the known charge state of the beam. The sample irradiation takes place under a pressure of approx.  $10^{-4} \text{ Pa}$  and at room temperature.

The GSI beam is a pulsed beam which is caused by the accelerator structure. For a homogeneous irradiation of a large area ( $50 \times 50 \text{ mm}^2$ ) the beam is defocused on the sample. For heavy ions ( $> \text{Ag}$ ) the flux has to be controlled below a level of  $2 \times 10^8 \text{ ions/cm}^2\text{-s}$  to avoid sample heating. The error of the fluence measurement is in a region of 20 % mainly caused by the inhomogeneity of the beam.

The following Table 2 gives an overview of the sample irradiations. The fluence was varied between  $1 \times 10^{10}$  and  $5 \times 10^{12} \text{ ions/cm}^2$ .

**Table 2: Used ion beams for room temperature experiments (GSI)**

Ion	Mass / amu	$E_{\text{total}}^1 /$ MeV	Range <sup>1</sup> / $\mu\text{m}$	$dE/dx$ at impact <sup>1</sup> / keV/nm	Characterisation method				
					IR	UV	TS <sup>2</sup>	DRS	ML <sup>3</sup>
U	238	2642	148	18.9	X				X
Pb	207	2298	153	15.0	X				X
Au	197	2187	152	14.4	X	X	X	X	
Sm	152	1687	154	11.1	X	X	X	X	
Xe	132	1465	140	9.7	X				X
Mo	98	1087	140	6.6	X	X		X	
Kr	78	866	142	5.1	X	X			
Ti	50	555	175	2.2	X	X	X	X	

<sup>1</sup> calculated by means of TRIM (SRIM2006) [73]

<sup>2</sup> Tensile strength

<sup>3</sup> Mass loss analysis

Figure 13 shows a schematic of the foil stack. For later analysis only the first 100  $\mu\text{m}$  of the stack were used in order to guarantee homogenous  $dE/dx$  values inside the foils. The foils beyond 100  $\mu\text{m}$  were used for pre-tests of the analytical methods. Foil 1 (25  $\mu\text{m}$ ) is used for tensile strength tests, foil 2 (50  $\mu\text{m}$ ) is investigated by dielectric relaxation spectroscopy and mass loss analysis, and foil 3 (12.7  $\mu\text{m}$ ) is analysed by means of optical methods (FT-IR and UV/Vis spectroscopy).

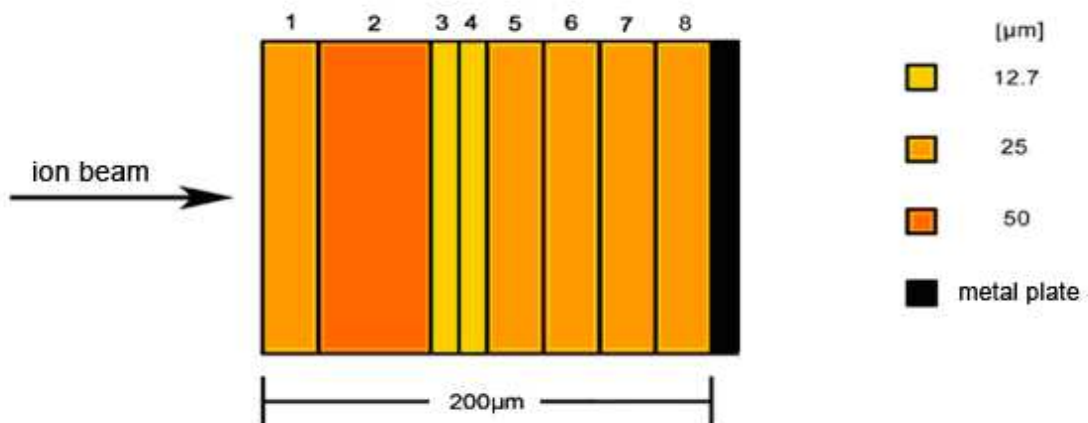


Figure 13: Foil stack (50x50 mm<sup>2</sup>) of polyimide for irradiation at GSI, X0

#### 4.4.2 Irradiation experiments at GANIL, Caen, France

The second ion beam facility used for this study is the GANIL (Grand Accélérateur National d'Ion Lourds) which is located in an institution of the CEA in Caen, France [82]. It also provides swift heavy ions but in contrast to the GSI, the GANIL uses one or two cyclotrons delivering a continuous beam (see Figure 14). After passing the first cyclotron (CSS1) the beam can be extracted for medium energy (3.7 – 13.7 MeV/u) experiments in the SME cave. For high energy experiments, the ions are injected in the second cyclotron (CCS2) reaching energies up to 96 MeV/u.

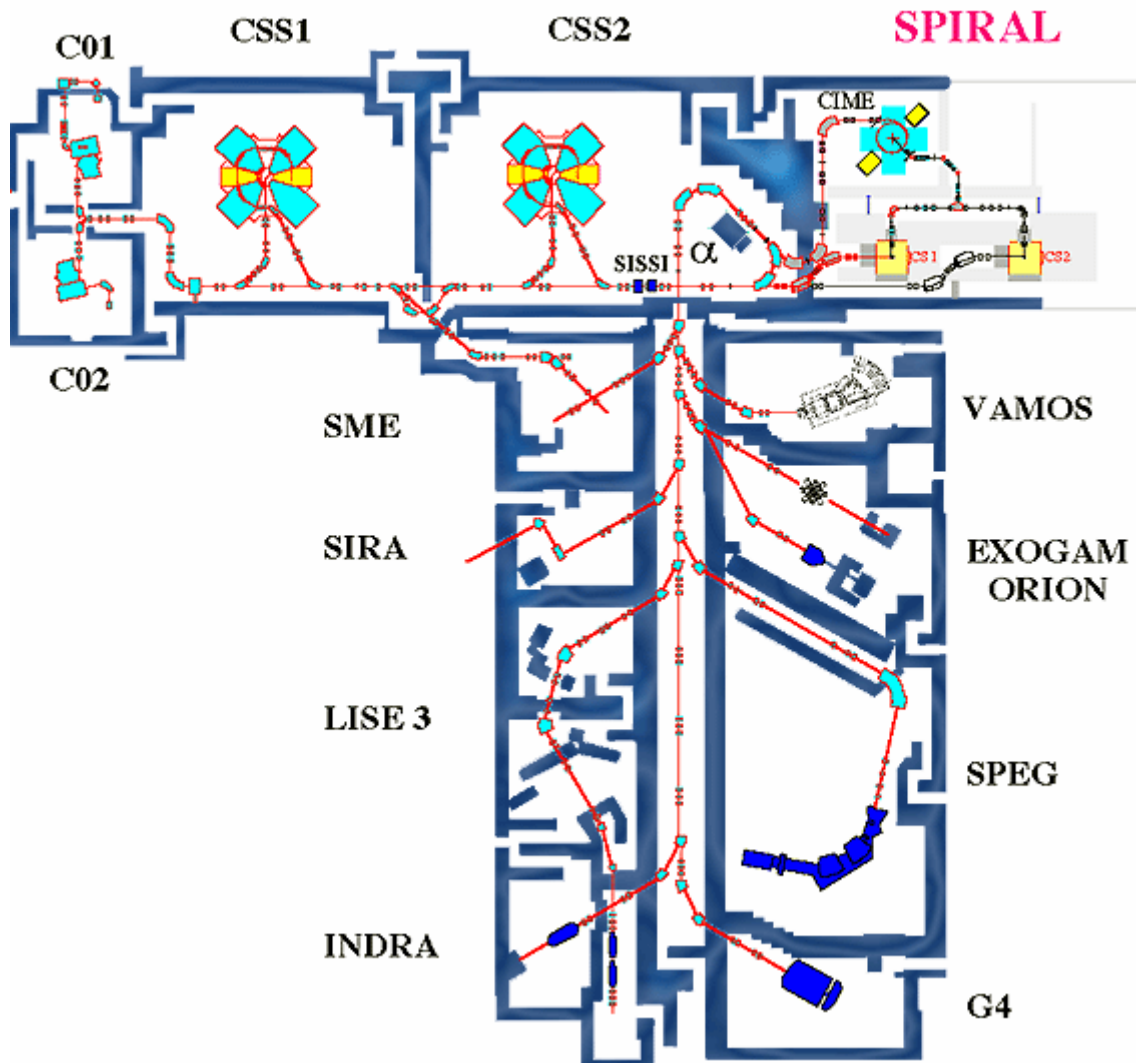


Figure 14: GANIL accelerator facility

The experiments were performed at the SME beam line using a beam scanner which homogeneously exposes a predefined sample area. The CASIMIR chamber (Chambre d'Analyse de Surfaces et Interfaces de Matériaux IRradiants) was applied which allows to analyse samples in-situ by means of transmission infrared spectroscopy. The setup was additionally equipped with a cryostat and a quadrupole mass spectrometer. The complete unit permits irradiations performed at low temperatures (13-20 K) under a pressure of  $10^{-5}$  Pa.

Table 3 indicates the beam parameters for the low temperature experiments. The Pb beam was used for outgassing experiments with energy of 4.3 MeV/u. The irradiated foils (50  $\mu\text{m}$ ) had a size of 18x40  $\text{mm}^2$  and were mounted on a cryostat. The in-situ infrared experiments were performed with a Kr beam (9.5 MeV/u). Therefore the polyimide foil (12  $\mu\text{m}$ ) was set on a ring cryostat sample holder which enables transmission measurements.

**Table 3: Used ion beams for low temperature experiments (GANIL)**

Ion	Mass / amu	$E_{\text{total}}^1$ / MeV	Range <sup>1</sup> / $\mu\text{m}$	dE/dx at impact <sup>1</sup> / keV/nm	Characterisation method	
					In-situ IR	MS
Pb	208	894	66	17.2		X
Kr	78	744	119	5.5	X	

<sup>1</sup> calculated by means of TRIM (SRIM2006) [73]

## 4.5 Analytical methods

### 4.5.1 Infrared spectroscopy

The infrared spectroscopy is a common analytical method to measure liquids, solids and (in specific cases) gases. The principle of optical spectroscopy is based on the detection of the absorption of electromagnetic radiation (Figure 15). The infrared spectroscopy operates in the wavenumber region between  $400 - 4000 \text{ cm}^{-1}$  equate to  $\lambda = 2500 - 25000 \text{ nm}$ . The analyte absorbs the radiation due to excitation of vibration and rotation levels which are specific for molecule groups.

For organic molecules the region  $> 1000 \text{ cm}^{-1}$  is typical for valence vibrations (change of bond length) which are characteristic for molecule groups like triple bonds, carboxyl or ether-functions. The region  $< 1000 \text{ cm}^{-1}$  is assigned to deformation vibrations (change of bond angle). These signals are specific for the entire molecular structure.

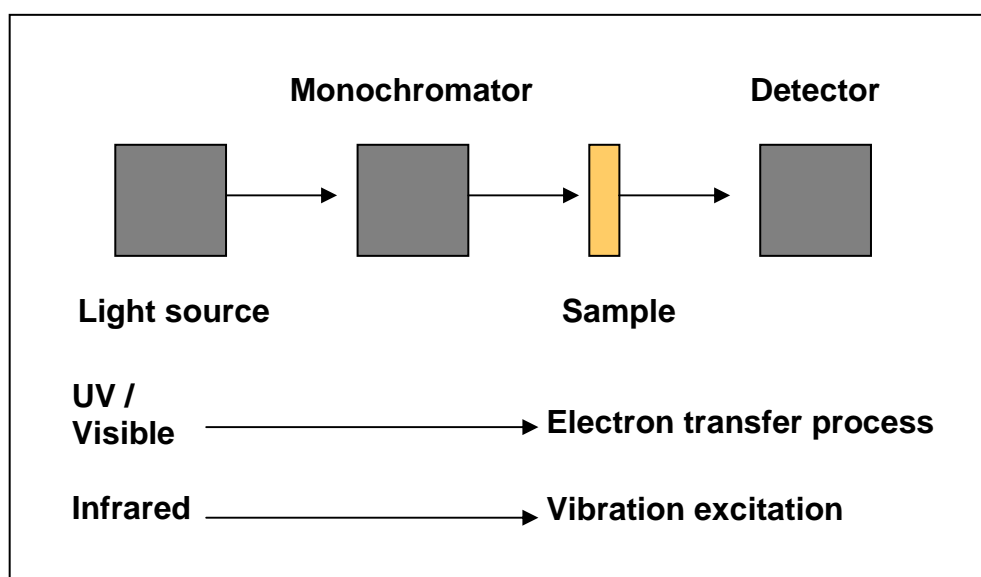


Figure 15: Principle of optical absorption spectroscopy

#### 4.5.1.1 *Experimental setup for room temperature infrared measurements*

The infrared measurements were performed with a Nicolet FTIR spectrometer (Magna-IR 550 with TGS detector) at GSI, materials research, Darmstadt (Germany). The infrared beam was centred in order to use the same region which was used for fluence calibration during the irradiation (centre square centimetre of the foil).

The analysed foils have a thickness of 12  $\mu\text{m}$  to obtain the best results related to the limited linearity of the detector signal which is set by absorption of 2. The infrared spectroscopy is used to follow the decrease of the imide group which is a typical group of the monomer (cp. Figure 10). Following the decrease of the signal of this group allows to follow the degradation of intact polymer chains. The peak height was used to evaluate the decrease. The evaluation of the peak height was done by the spectroscopy software OMNIC 4.1a by using an automatic background correction.

#### 4.5.1.2 *Experimental setup for low temperature infrared measurements*

The low temperature infrared spectroscopy measurements were performed on 12  $\mu\text{m}$  foils analysed with a Nicolet FTIR spectrometer (Magna-IR 550 with cooled TE DLaTGS detector) in the CASIMIR Chamber at CIRIL, Caen (France) in transmission mode (spectral resolution of 2  $\text{cm}^{-1}$ ). The sample was mounted to a ring that was connected to a cryostat inside the irradiation chamber allowing in-situ spectroscopy at temperatures between 13 and 300 K. The absorption bands were evaluated by determining the absorbance of the centroid height with the baseline method. In contrast to the room temperature measurements at GSI, the spectra were recorded under the Brewster angle ( $55^\circ$ ) to avoid interference effects at the sample/air interface. Under this geometry the effective foil thickness increases to 21  $\mu\text{m}$ . This has to be noticed by a comparison between measurements under different angles. The measurement under the Brewster angle was chosen for analyzing weak peaks in the region between 1700 and 3000  $\text{cm}^{-1}$  (triple bonds and small molecules like CO and CO<sub>2</sub>).

#### 4.5.1.3 Infrared spectrum of polyimide

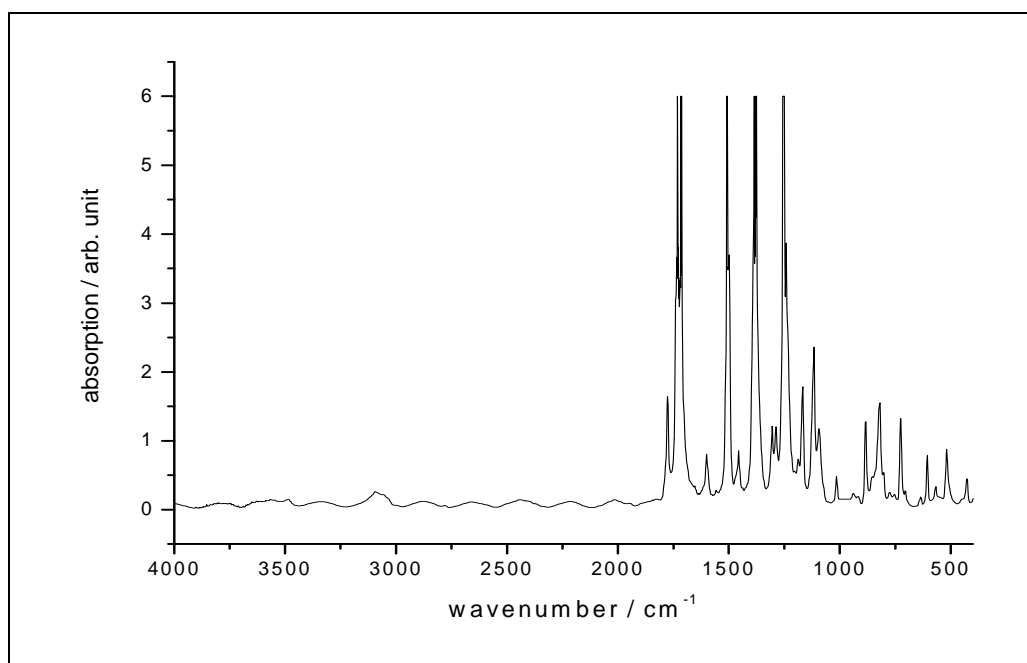


**Figure 16: Infrared spectrum of a virgin 12  $\mu\text{m}$  polyimide foil**

Figure 16 shows the infrared spectrum of a virgin 12  $\mu\text{m}$  polyimide foil. The vibration bands are identified and listed in Table 4. According to the literature, the identification of some of the bands is not unambiguous. Especially the weaker peaks which will be very important for the degradation analysis are differently interpreted. The mostly dominating bands of the spectrum are assigned to the fundamental valence vibrations of the functional groups of the polymer backbone: 1250  $\text{cm}^{-1}$  ether function, 1380  $\text{cm}^{-1}$  imide function, 1500  $\text{cm}^{-1}$  phenyl function and 1730  $\text{cm}^{-1}$  carbonyl function. In the region above 1800  $\text{cm}^{-1}$ , the interferences of the surface reflection are too strong to identify weak bands. An exception is the band between 3000 and 3200  $\text{cm}^{-1}$  representing the vibrations of the aromatic hydrogen atoms.

Table 4: Identification of the infrared signals of polyimide

band / $\text{cm}^{-1}$	intensity	Identification according to [83]	Identification according to [53] based on [84]
1775	m	$\nu_s(\text{C=O})$	$\nu_s(\text{C=O})$
1730	s	$\nu_{as}(\text{C=O})$	$\nu_{as}(\text{C=O})$
1601	m	$\nu_s(\text{aromatic})$	$\nu_s(\text{aromatic})$
1500	s	$\nu_s(\text{aromatic})$	$\nu_s(\text{aromatic})$
1456	m	$\delta(\text{aromatic})$	$\delta(\text{aromatic})$
1380	s	$\nu_{as}(\text{imide ring})$	$\nu_{as}(\text{imide ring})$
1306	w		
1288	w		
1250	s	$\nu_{as}(\text{C-O-C})$	$\nu_{as}(\text{C-O-C})$
1169	m	transversal vib. of the imide ring	$\delta(\text{in-plane})(\text{C-H})$ of the <i>para</i> -substituted phenyl
1117	s	transversal vib. of the imide ring	$\delta(\text{in-plane})(\text{C-H})$ of the <i>para</i> -substituted phenyl
1093	m		$\delta(\text{in-plane})(\text{C-H})$ of the <i>para</i> -substituted phenyl
1016	w	$\delta(\text{in-plane})(\text{C-H})$ of the <i>para</i> -substituted phenyl	$\delta(\text{in-plane})(\text{C-H})$ of the <i>para</i> -substituted phenyl
883	m		$\delta(\text{out-of-plane})(\text{C-H})$ of the phenyl between the imide rings
819	m		$\delta(\text{out-of-plane})(\text{C-H})$ of the <i>para</i> -substituted phenyl
725	m	$\delta(\text{out-of-plane})(\text{imide ring})$	Aromatic ring [85]
636	w		$\delta(\text{C=O})$
605	m	$\delta(\text{out-of-plane})(\text{C-H})$ of the phenyl between the imide rings	$\delta$ bending of the C-O-C
567	w		$\delta(\text{rocking})(\text{imide ring})$
518	m		$\delta(\text{out-of-plane})$ ring bending of the <i>para</i> -substituted phenyl

## 4.5.2 UV/Vis spectroscopy

The UV/Vis spectroscopy is based on the same principles as infrared spectroscopy (Figure 15). The source delivers light of wavelength between 390 nm (UV region) and 900 nm (visible light). The absorption is due to electron transfer processes between  $\pi-\pi^*$  or  $n-\pi^*$  levels in organic molecules (e.g. polymers) or due to charge transfer between ligand and centre atom in complex anorganic molecules.

### 4.5.2.1 *Experimental setup for UV/Vis measurements*

The spectroscopic measurements were performed with an ATI UNICAM double beam spectrometer (UV4) at GSI, materials research, Darmstadt (Germany) with a resolution of 2 nm. The analysing beam was centred on the sample in order to use the same region which was used for fluence calibration during the irradiation (centre square centimetre of the foil).

### 4.5.2.2 *UV/Vis spectrum of polyimide*

The UV/Vis spectrum of virgin polyimide is very simple and shows a transition from total absorbance in the UV region ( $\lambda < 450$  nm) to total transmission ( $\lambda > 550$  nm) (Figure 17). In the conversion region between 450 and 550 nm the spectrum shows a straight rise of transmission. The UV/Vis spectroscopy is used as an analytical method to follow the carbonisation of the polymer [86]. The degradation of the polymer leads to a formation of carbon clusters which causes a discolouration from yellow over brown to black. The technique allows to consequently follow the discolouration of the polymer.

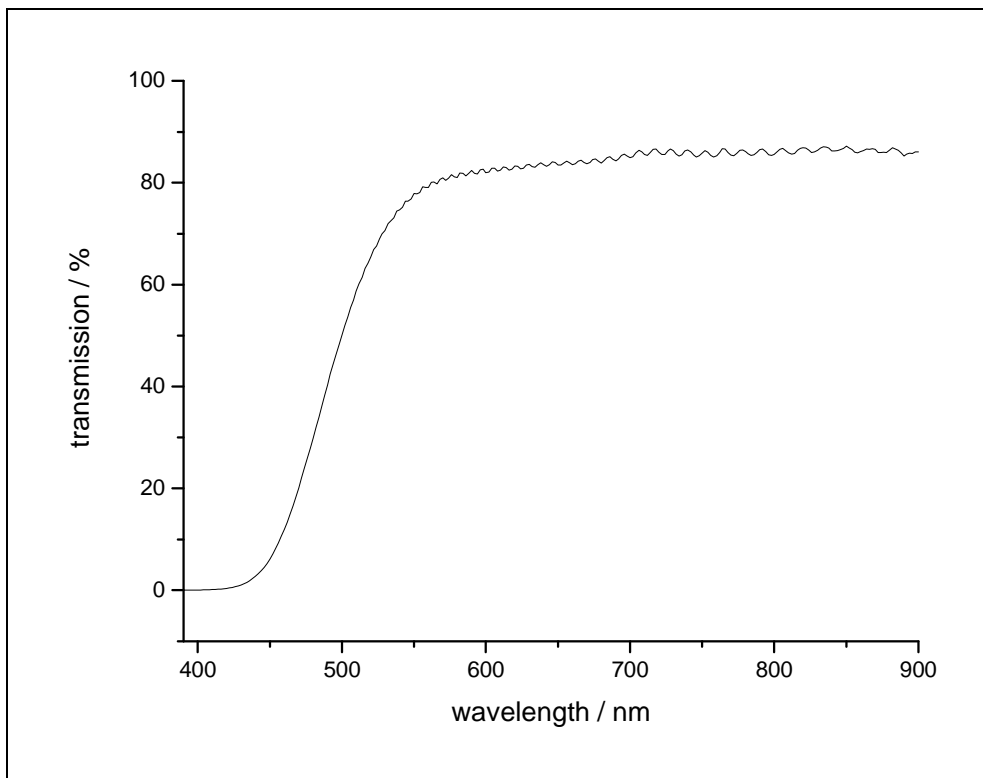


Figure 17: UV/Vis spectrum of a virgin 12 μm thick polyimide foil

### 4.5.3 Tensile strength

The tensile strength measurement is a standard method of the non oscillating stress test in contrast to dynamic mechanical analysis (DMA) [87] providing the characteristic stress/strain curve of a material (Figure 19). The stress is a synonym for the applied standard force also called tensile strength and strain is an equal expression for the elongation of the sample. The curve including information about tensile strength (yield strength)  $\sigma_B$ , tensile strength at break  $\sigma_R$ , elongation yield  $\varepsilon_B$ , elongation at break  $\varepsilon_R$  and the Young's modulus (modulus of elasticity)  $E_{\text{Young}}$ . The tensile strength at break and the elongation at break are given by the endpoint of the curve, representing the breaking point. The yield strength and the elongation at yield indicate the point of flowing. It has to be noted that only a few polymers show this flowing behaviour (especially thermoplastic polymers). Polyimide does not show it.

The Young's modulus can be calculated in the linear regime of the curve below the proportional limit with:

$$E_{\text{Young}} = \frac{\sigma}{\varepsilon} \quad (7)$$

based on the Hooke's law reflecting the gradient of the curve. It characterises the stiffness of the material.

#### 4.5.3.1 *Experimental setup for tensile strength measurements*

The tensile strength measurements were performed at the Deutsches Kunststoff Institut (DKI) in Darmstadt, Germany with a Zwick Z020TH<sup>2a</sup> (with macro setup). The total sample length was 50 mm with an effective measurement length of 30 mm and a width of 15 mm. It has to be noted that the sample geometry differs to the DIN geometry (bone form). The load cell was set to 500 N and the pneumatic clamps were set to 200 N.

Due to the fact that this macroscopic method has a large uncertainty each irradiated 50x50 mm<sup>2</sup> foil was cut into two pieces (50x15 mm<sup>2</sup>) so that one irradiation point was measured twice. Anisotropy behaviour related to the

orientation of the foil was excluded by measuring two virgin samples which were cut 90° to each other.

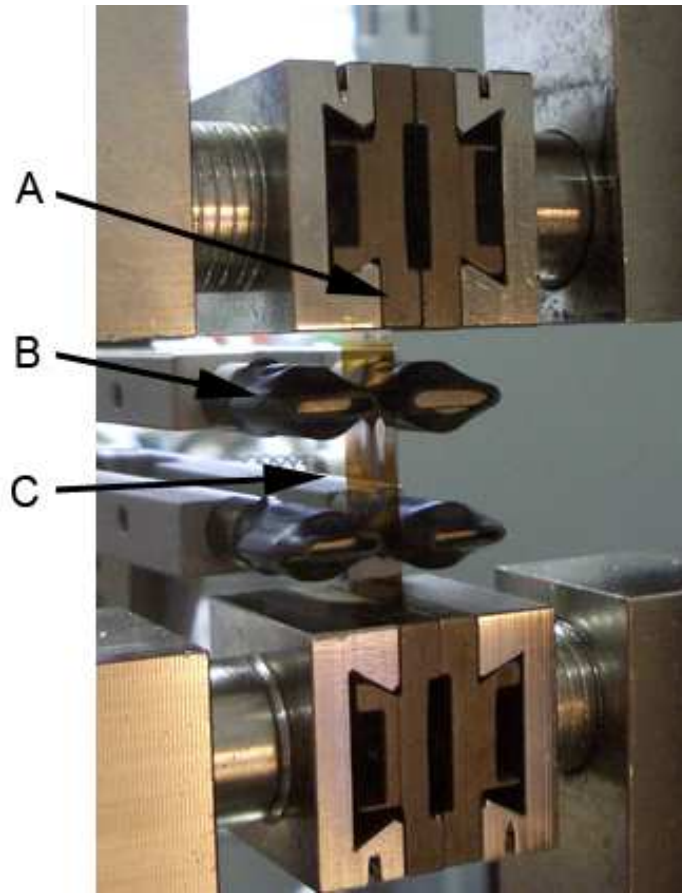


**Figure 18: Setup of a tensile strength measurement. (A) pneumatic clamps, (B) automatic macro clamps, (C) sample.**

The critical point of the measurement is the sample cutting and the clamping of the sample into the machine. Irregularities at the cutting edge (e.g. cracks) form weak points which cause a breaking of the sample before its material breaking point. The 25  $\mu\text{m}$  polyimide foils were cut with razor blades on top of a soft material (leather). Cutting tests have shown that this procedure leads to flat and straight edges. The macro setup allows that the foil is only prefixed between the pneumatic clamps and subsequently fixed by computer controlled macro clamps. Figure 18 shows the macro clamps, additionally covered with shrink hoses to avoid pre damaging of the foil at the clamps.

With respect to the described measurement setup and sample preparation technique the results are not comparable with literature value measured under DIN conditions because it was not possible to use the norm die-cutter to

prepare the sample strips out of the foil because the highly irradiated foils are too brittle.

#### 4.5.3.2 Stress/strain curve of polyimide

The stress/strain curve of polyimide shown in Figure 19 displays the measurements of two samples cut out of a virgin 25  $\mu\text{m}$  polyimide foil. The proportional limit is reached at 30 MPa. The linear increase below the proportional limit characterises the Young's modulus of a virgin Kapton foil measured under the described geometry with  $E_{\text{young}}=3.5 \pm 0.1$  GPa. The literature value for 25  $\mu\text{m}$  commercial polyimide foil (Kapton) given by DuPont is  $E_{\text{young}}=2.5$  GPa under DIN geometry. Due to this, the measurement is very close to the DIN method value. The difference in the sample geometry leads to the discrepancy of the Young's modulus values.

The end of the curve indicates the tensile strength at break  $\sigma_B=151.4$  MPa and the elongation at break  $\varepsilon_B=16.0$  %. The tensile strength at break of the irradiated samples is chosen as criteria to estimate the mechanical degradation of the material.

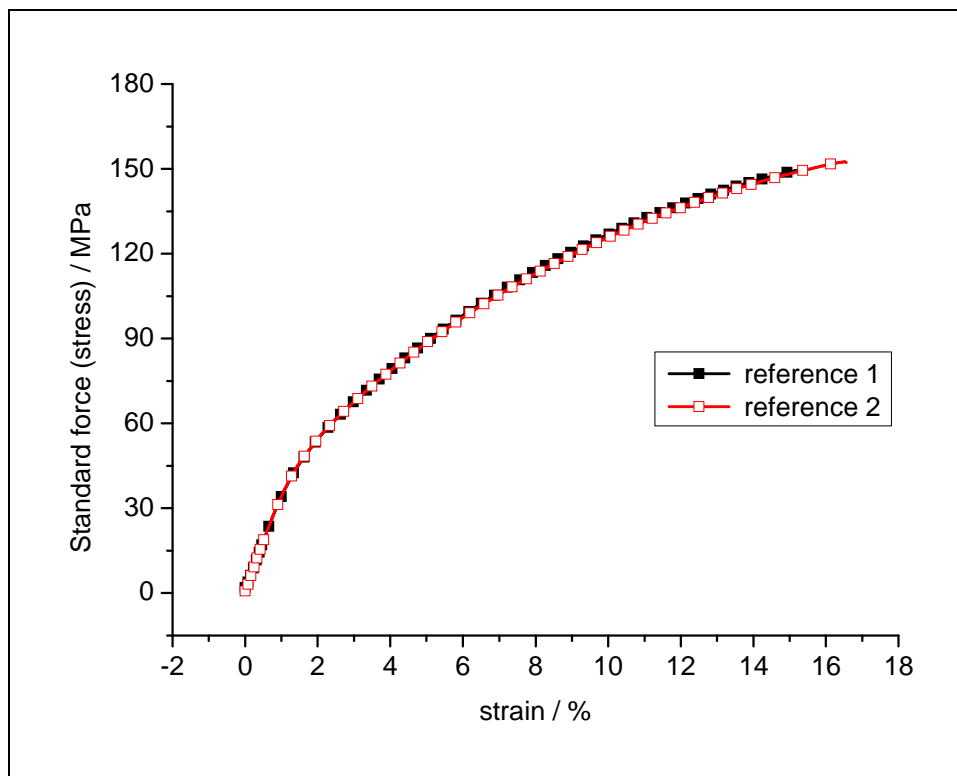


Figure 19: Stress/strain curve of a virgin 25  $\mu\text{m}$  polyimide foil

#### 4.5.4 Dielectric relaxation spectroscopy (DRS)

##### 4.5.4.1 Theoretical principle

The dielectric relaxation spectroscopy (DRS) also known as impedance spectroscopy allows frequency dependent measurements of conductivity ( $\sigma(\omega)$ ) and dielectric function  $\epsilon(\omega)$ . The results give indications about the long range mobility of charge carriers which basically are responsible for the transport mechanism. Thus the DRS is suited to characterise the electrical behaviour of materials but it is also used to measure the properties of electrical parts like ohmic resistances, inductors and capacitors.

The measurement is performed with the dielectric samples positioned between two plates similar to a capacitor. A frequency sweep of an ac voltage with low amplitude is applied. The ac voltage induces an ac current with the same frequency inside the sample. This current can be divided into two components: one is oscillating in phase and one is shifted by  $\pi/2$  related to the applied ac voltage. The real part of the complex conductivity is proportional to the amplitude of the induced in-phase current ( $I_{01}$ ). The following equation expresses the real part of the complex conductivity ( $\sigma'(\omega)$ )

$$\sigma'(\omega) = \frac{I_{01}}{U_0} \cdot \frac{d}{A} \quad (8)$$

where  $U_0$  denotes the applied voltage amplitude,  $d$  is the sample thickness and  $A$  is the sample area. The real part of the conductivity represents the dissipated energy (e.g. the amount of energy which is converted in heat). The imaginary part of the complex conductivity ( $\sigma''(\omega)$ ) indicates the electrical energy which is stored in the sample. It is proportional to the ac current ( $I_{02}$ ) phase shifted by  $\pi/2$  and can be expressed by:

$$\sigma''(\omega) = \frac{I_{02}}{U_0} \cdot \frac{d}{A} \quad (9)$$

The complex conductivity consists of the sum of these two parts and is given by:

$$\widehat{\sigma}(\omega) = \sigma'(\omega) + i\sigma''(\omega) \quad (10)$$

#### 4.5.4.2 Experimental setup and sample preparation for DRS measurements

The dielectric measurements were performed with a frequency response analysis at the DKI Darmstadt, Germany. The system consists of a Solartron SI 1260 Impedance/Gain phase analyzer and a Novocontrol broadband dielectric converter. Additionally the capacity was measured with a HP 4284 LCR. Figure 20 shows a simple schematic of the measurement setup. The frequency generator applies an ac current to a capacitor-like setup with the sample between the capacitor plates as a dielectric. The resulting voltage and current is measured.

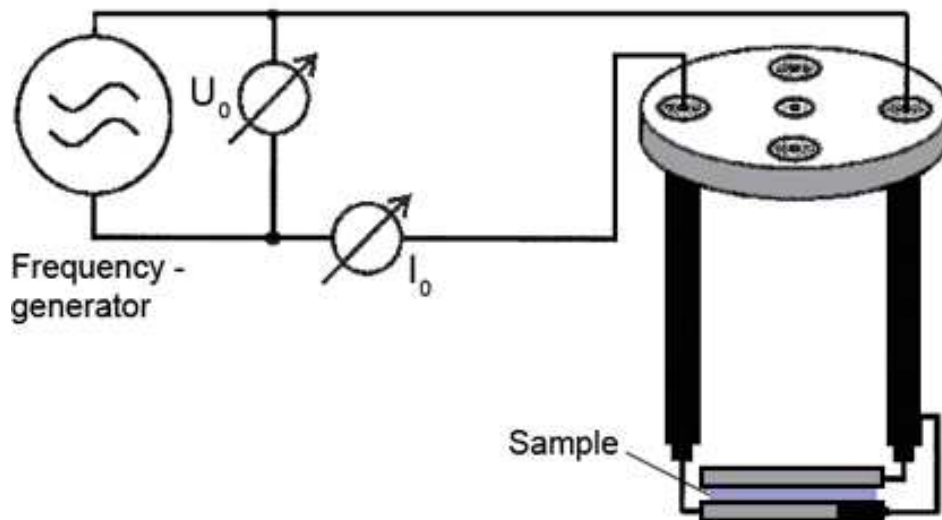


**Figure 20: Scheme of DRS measurement**

A circular sample with a diameter of 22 mm was punched out of the 50x50 mm<sup>2</sup> irradiated 50 μm thick foils. The foil surface was cleaned with ethanol. The dry foils were set into a mask with an open diameter of 20 mm and were afterwards sputter coated with gold to guarantee the sample contacting. Therefore a

sputter setup was used (10 Pa, 25 mA for 180 s). The prepared samples were placed between two gold plates by means of a spring to guarantee constant pressure condition during measurements. The whole setting was inserted into a stainless steel chamber for shielding. All the measurements were performed at ambient conditions.

To analyse the interface between the sputtered gold and the polymer surface, a SEM image including an EDX measurement was performed. Figure 21 shows a cross section of a gold-sputtered 50  $\mu\text{m}$  thick Kapton foil irradiated with  $1 \times 10^{11}$  Au ions/cm<sup>2</sup>. It clearly identifies the approx. 1  $\mu\text{m}$  thin gold layers with a sharp boarder at the foil side. The irregular structure of the lower boarder results from the cutting process during sample preparation. The measurement illustrates that no gold diffusion into the polymer foil occurs which is confirmed by an EDX scan across the sample.

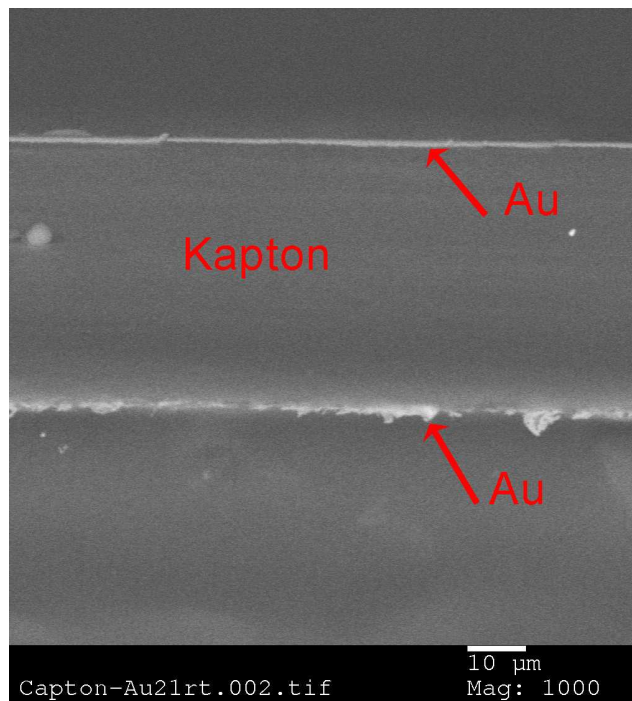


**Figure 21: SEM image of the cross section of an irradiated polyimide foil after gold sputtering for DRS measurements.**

#### 4.5.4.3 Dielectric spectrum of polyimide

Figure 22 shows the dielectric spectrum of a 50  $\mu\text{m}$  virgin polyimide foil including the conductivity  $\sigma'$  (red) and dielectric permittivity  $\epsilon'$  (black) as a function of the frequency of the applied AC voltage. The conductivity increases with the applied frequency which is scanned from 1 MHz to 0.1 Hz.

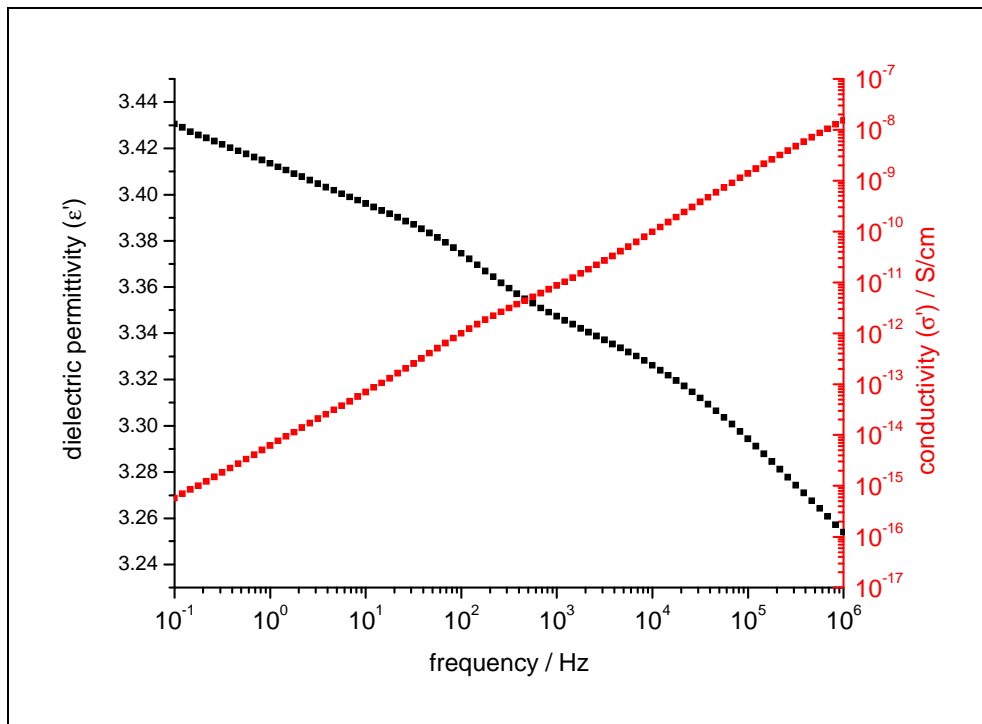


Figure 22: Dielectric spectrum of a virgin polyimide foil (thickness 50  $\mu\text{m}$ ) showing the conductivity ( $\sigma'$ ) and the dielectric permittivity ( $\epsilon'$ ) as a function of the frequency of the applied ac voltage.

### 4.5.5 Mass loss analysis

A simple technique was used by weighing the polymer foil before and after the irradiation to estimate the mass loss induced by the irradiation. Therefore the 50  $\mu\text{m}$  thick Kapton foils (50x50  $\text{mm}^2$ ) were weighed with an analytical balance from Scaltec (SBA32). Table 5 presents the absolute values of the analysed foils. It has to be mentioned that the error of the weighing is set to  $\pm 0.5$  mg due to errors of the analytic balance and due to minimal pollution of the samples during the transport from the irradiation cave to the balance.

**Table 5: Mass loss induced by ion irradiation. The values are due to 50  $\mu\text{m}$  thick Kapton foils of an area of 50x50  $\text{mm}^2$ .**

Ion	Fluence / $\text{n/cm}^2$	m (before irradiation) / mg	Mass loss / mg
Xe	$1 \times 10^{10}$	175.9	0.3
	$5 \times 10^{10}$	177.0	0.7
	$1 \times 10^{11}$	175.8	1.2
	$2 \times 10^{11}$	175.5	2.0
	$4 \times 10^{11}$	177.2	4.2
	$1 \times 10^{12}$	173.0	9.6
Pb	$1 \times 10^{10}$	176.3	0.0
	$5 \times 10^{10}$	178.7	0.4
	$1 \times 10^{11}$	180.0	1.0
	$2 \times 10^{11}$	172.8	1.7
	$4 \times 10^{11}$	177.7	3.1
U (1)	$1 \times 10^{10}$	178.5	0.6
	$5 \times 10^{10}$	176.3	1.2
	$1 \times 10^{11}$	184.1	2.9
	$2 \times 10^{11}$	178.2	4.6
	$4 \times 10^{11}$	174.6	9.4
U (2)	$5 \times 10^9$	182.9	(-0.5)
	$2.5 \times 10^{10}$	171.9	0.4
	$5 \times 10^{10}$	180.1	1.6
	$1 \times 10^{11}$	182.7	2.8
	$2 \times 10^{11}$	177.9	5.1

## 4.5.6 Residual gas analysis during irradiation

### 4.5.6.1 Theoretical principle

The residual gas analysis (RGA) is based on mass spectroscopic measurements of a gas atmosphere, usually by means of a quadrupole mass spectrometer (QMS). Neutral volatile molecules become charged by an ionizer. Electron impact ionization is the method of choice but leads to the problem of fragmentation. The energy of the electrons has to be high enough to ionize the molecule but under the threshold of fragmentation. With respect to the variety of different molecules usually a medium ionization voltage is selected. The charged particles are selected by the magnetic field of the quadrupole and afterwards detected with a secondary electron multiplier (SEM). The ability of a particle to pass the quadrupole depends on its mass-to-charge ratio ( $m/z$ ).

To record a spectrum over the entire mass range, the quadrupole is swept (analogue-scan-mode). The single-ion-mode provides the possibility to measure up to 64 selected masses stepwise to increase the sensitivity of the measurement.

### 4.5.6.2 Experimental setup for residual gas analysis

The residual gas in the irradiation chamber is monitored with a quadrupole mass spectrometer (QMS) from Balzer (Prisma QMS 200) operated in the scan mode for mass-to-charge ratio ( $m/z$ ) from 1 to 200. The head of the QMS was positioned 20 mm below the sample (Figure 23). During the entire experiment, the chamber was evacuated with a turbo molecular pump ( $p < 10^{-4}$  Pa). A typical measuring cycle consisted of monitoring the QMS signal during ion irradiation of a 50  $\mu\text{m}$  thick polyimide foil. The ion beam is scanned across the entire sample surface (18x40  $\text{mm}^2$ ).

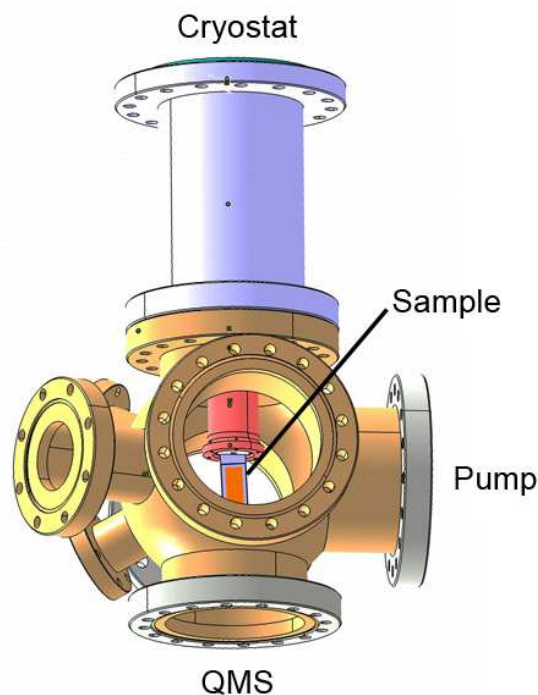


**Figure 23:** Irradiation chamber used for the residual gas analysis at the GANIL in Caen, France. The ion beam enters the chamber from the front and is scanned across the entire sample area.

#### 4.5.6.3 *Background spectrum*

Prior to the ion exposure of the Kapton sample, background measurements of the chamber were recorded without and with beam on the empty Copper sample holder. The sample holder which allows the mounting of a sample and a reference at the same time ensures equal conditions of both measurements. Figure 24 shows the QMS signal of a low temperatures (12 K) irradiation of the empty Copper sample holder (red curve) and of a 50  $\mu\text{m}$  polyimide foil (black curve). After  $\sim 300$  s the ion beam is switched on, leading to an increase of the mass signal ( $m/z=28$  shown exemplarily). In the case of the empty sample holder, the signal increases by one order of magnitude whereas the irradiation of the polyimide sample leads to an increase of three orders of magnitude. For the later analysis, each mass signal is corrected by subtracting the background signal taken from a reference measurement before each sample irradiation of the empty sample holder.

The small fluctuations of the recorded mass signals are ascribed to beam flux variations. Otherwise, the signal is rather constant during the entire irradiation of approx. 1 h.

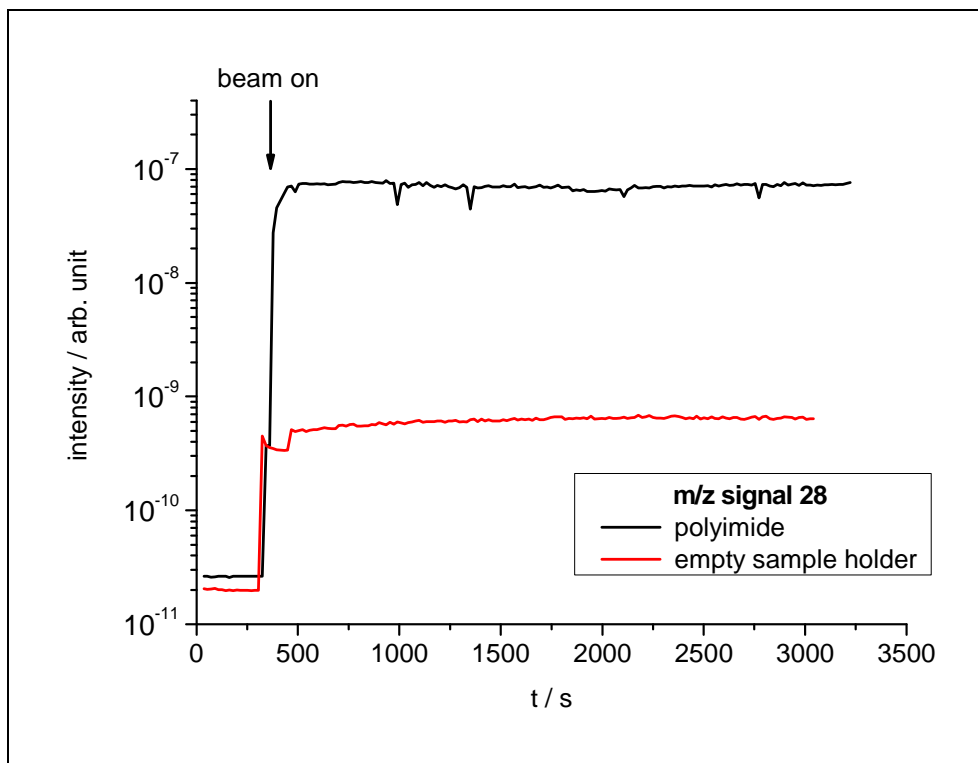


Figure 24: QMS signal of  $m/z = 28$  for a 50  $\mu\text{m}$  polyimide foil (black) and for the empty sample holder (red) during irradiation with Pb ions.

## 4.5.7 Residual gas analysis during heat-up cycles

### 4.5.7.1 Theoretical principle

A second characteristic of the outgassing species besides the  $m/z$  ratio is given by their specific outgassing temperature. Heat-up cycles give indications of the outgassing temperatures of a specific gas in the given setup related to its normal pressure boiling point. The calibration experiment was performed with several gases available at the GANIL laboratory. The cold chamber was filled with methane ( $\text{CH}_4$ ), propadiene ( $\text{C}_3\text{H}_4$ ) or carbon dioxide ( $\text{CO}_2$ ) which freeze onto the sample holder. Figure 25 displays the three calibration points. The calibration curve is not an absolute identification property but has to be seen as a complementary tool to the QMS information.

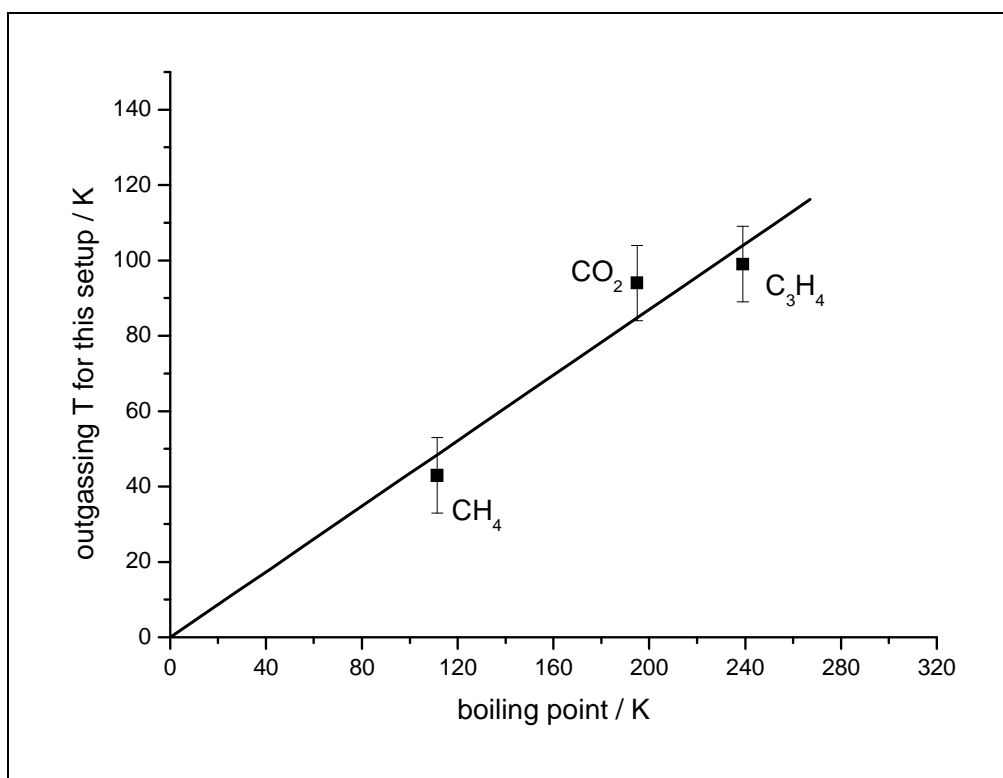


Figure 25: Relation between the normal pressure boiling point and the outgassing temperature.

#### 4.5.7.2 *Experimental setup for the residual gas analysis*

The measurement setup is shown in Figure 23. The polymer sample was irradiated at low temperature. After the irradiation, the sample holder was heated with a rate of 3 K/min and 30 W. A linear increase of temperature was assured by heating against the cooling of the cryostat. A thermal sensor at the sample holder guarantees constant heating while avoiding intensive heating spikes. A reference measurement of the empty chamber (irradiation of the sample holder without sample and heat-up cycle) was performed before each measurement. The QMS was operated in the single ion mode for selected masses with  $m/z$  between 2 and 149. The mass selection was done on the base of a test irradiation where the heat-up cycle was analysed in the analogue-scan-mode recording the full range up to  $m/z = 200$ .

#### 4.5.7.3 *Background spectrum*

Figure 26 shows the outgassing spectrum of the empty sample holder after irradiation at low temperature. The analysed masses represent the only intensive signal of the background measurement. The dominating mass fragment is  $m/z = 2$  corresponding to hydrogen. It rises with the beginning of the heat-up cycle and behaves independently of the temperature. The residual outgassing spectrum can be divided into three segments: a)  $m/z=18$  representing water in a temperature region between 140 and 180 K. b) the  $m/z$  values 28 and 32 is based on the outgassing of CO and O<sub>2</sub> represented by the peak between 30 and 60 K. c) The very weak peak of the masses 44 and 26 between 75 and 110 K indicates carbon dioxide (CO<sub>2</sub>) and ethyne (C<sub>2</sub>H<sub>2</sub>). These impurities are known from other residual gas analysis of measurements including vacuum chambers [88]. The outburst of water between 140 and 180 K restricts the method because of the large amount of volatile molecules which cause an overload of the mass detector. The overload is clearly notable in the background spectrum indicated by a rise of all masses below the water peak.

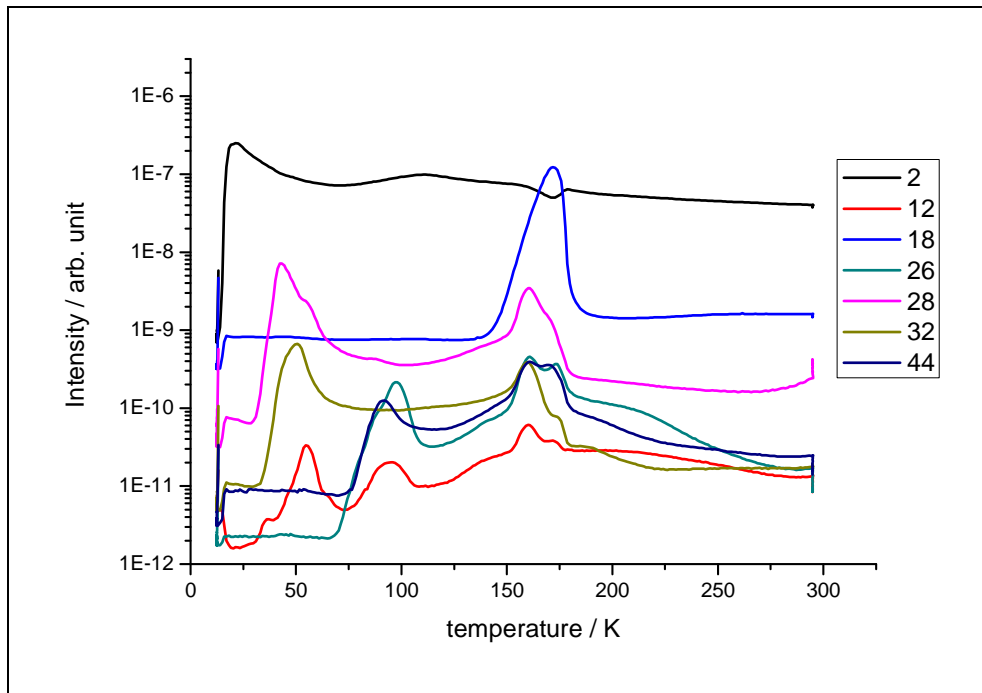


**Figure 26: Outgassing during the heat-up cycle after irradiation of the empty chamber.**

For the later analysis of the outgassing spectra after irradiation during the heat-up cycle, each mass is corrected by subtracting the intensity of the background run with the empty sample holder. The background measurements have been taken directly before the sample measurements with the sample conditions concerning vacuum, beam and temperature settings.

## Chapter 5 :

# Results and discussion

### 5.1 Room temperature experiments

#### 5.1.1 Infrared spectroscopy

Figure 27 shows the infrared spectrum of a 12  $\mu\text{m}$  thick Kapton foil irradiated with Mo ions ( $2 \times 10^{12}$  ions/ $\text{cm}^2$ ) in comparison with a virgin foil. The spectrum of the irradiated foil points to an expected decrease of absorbance of the polymer bands.

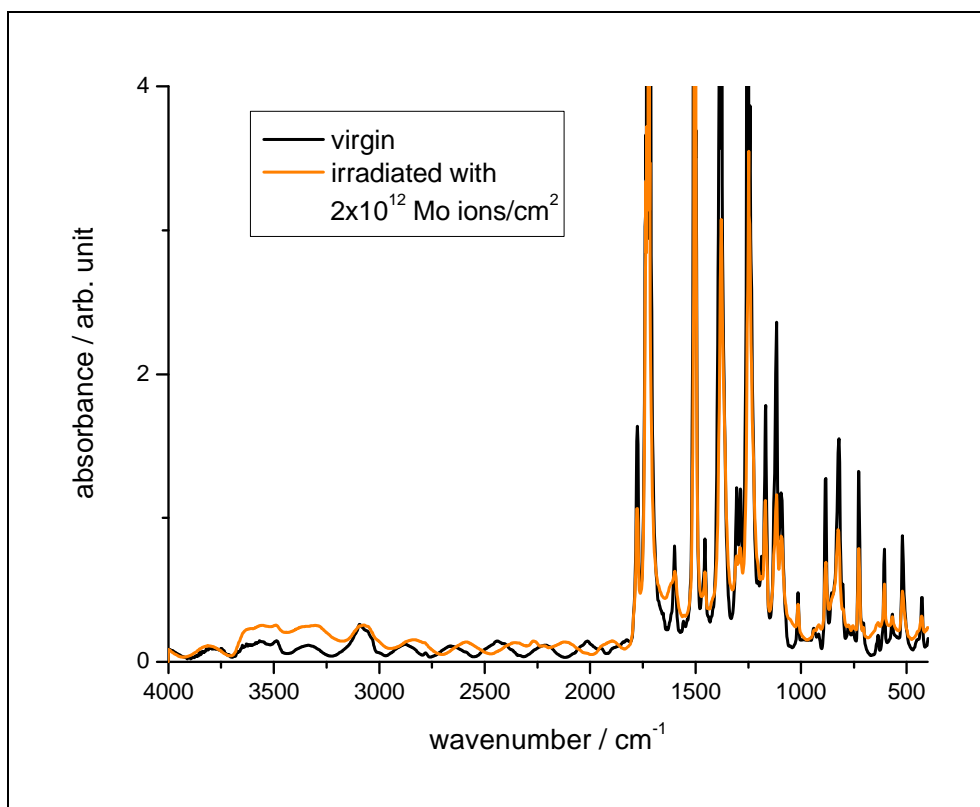
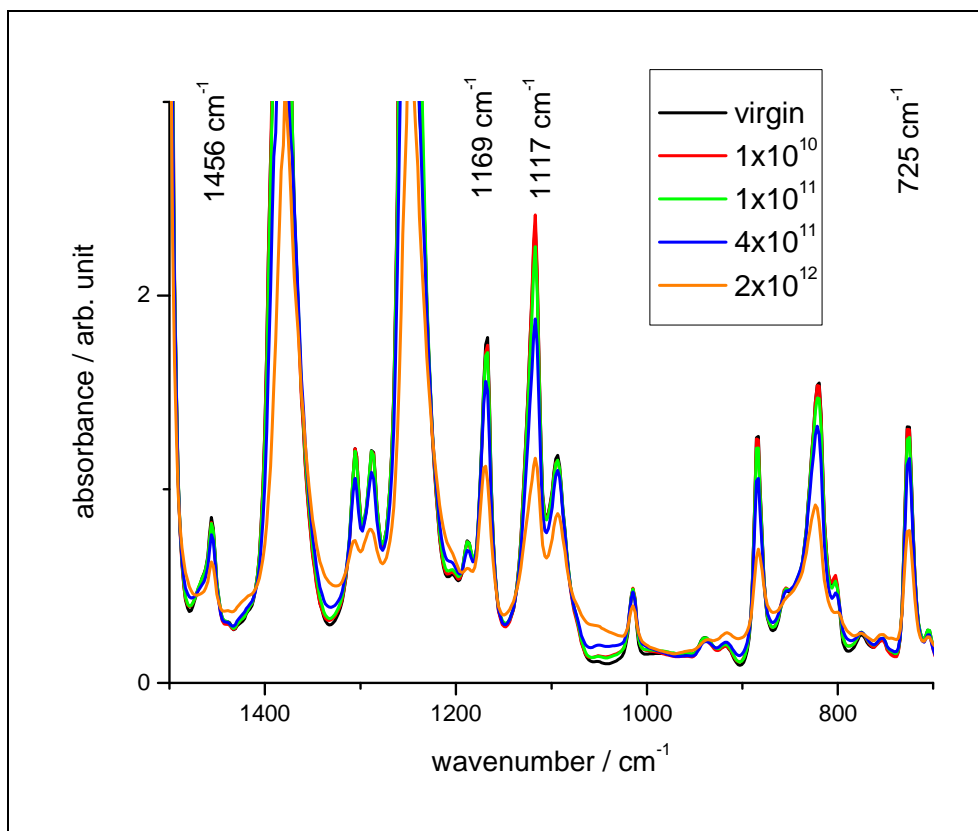


Figure 27: Comparison of infrared spectra of a virgin and an irradiated 12  $\mu\text{m}$  polyimide foil.

The region from 400 to 1800  $\text{cm}^{-1}$  can be assigned to specific polymer bands. The typical vibration bands of the aromatic ring (1456, 1500, and 1601  $\text{cm}^{-1}$ ), the ether (1250  $\text{cm}^{-1}$ ), and the carbonyl function (1730 and 1775  $\text{cm}^{-1}$ ) have an extreme high absorbance which extended the linearity of the detector leading to a cut-off saturation. From wavenumbers 1800 to 3000  $\text{cm}^{-1}$ , the spectrum is characterised by irregular ondulation. Due to this interference caused by reflections at the foil surface, it is very difficult to analyse bands of low absorbance in this region. Above 3000  $\text{cm}^{-1}$ , the absorption of the irradiated sample gives indications for the creation of hydroxyl groups (broad peak at 3500  $\text{cm}^{-1}$ ) and triple bonds (3295  $\text{cm}^{-1}$ ).



**Figure 28:** Infrared spectrum of 12  $\mu\text{m}$  polyimide foils irradiated with 5.2 MeV/u Mo ions.

To quantify the polymer degradation, four peaks below an absorbance of 2.5 are chosen as indicators (Figure 28). The limitation in absorbance is linked to the linear limit of the detector. The identification of some of the peaks is ambiguous due to the fact that the literature offers different interpretations (see also 4.5.1.3). The peak at 1456  $\text{cm}^{-1}$  is in literature clearly assigned to the phenyl group. The signal at 1169  $\text{cm}^{-1}$  and 1117  $\text{cm}^{-1}$  are linked to the

transversal vibration of the imide ring [89] but also interpreted as the C-H vibration of the *para* substituted phenyl ring [53]. The band at  $725\text{ cm}^{-1}$  belongs to the out-of-plane vibration of the imide ring [89] or to the deformation vibration of the aromatic ring [85]. In consideration of all literature data, the imide signal could not clearly be assigned to a specific signal except the main vibration at  $1380\text{ cm}^{-1}$ , but this band could not be quantified due to its large absorbance.

Figure 29 shows the evaluation of the four selected bands as a function of fluence  $5.2\text{ MeV/u Mo}$  ions. The three bands at  $1456$ ,  $1169$ , and  $725\text{ cm}^{-1}$  show the same degradation tendency. The band at  $1456\text{ cm}^{-1}$  exhibits a slightly weaker decrease in comparison to the other curves. A reason could be the small intensity of the band followed by a more drastic interference with the background noise which shows a little increase for the high fluence samples.

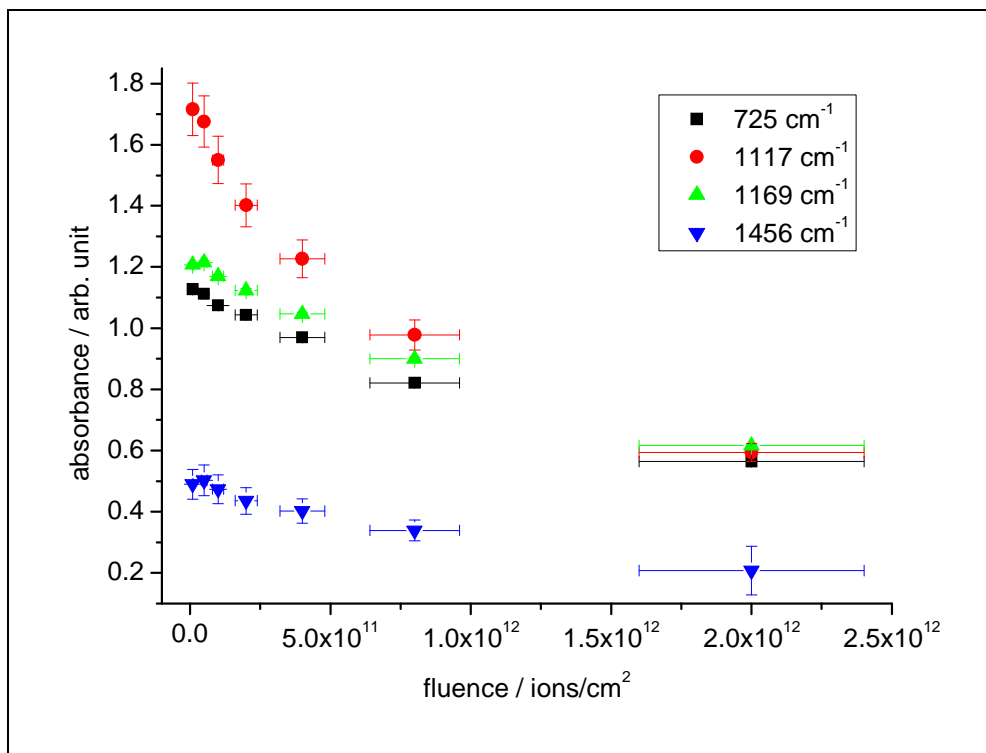


**Figure 29: Absorption of different infrared bands as function of the fluence of  $12\text{ }\mu\text{m}$  polyimide foils after irradiation with  $5.2\text{ MeV/u Mo}$  ions.**

The peak at  $1117\text{ cm}^{-1}$  indicates a different decrease by showing a sharp decline in the fluence region up to  $5 \times 10^{11}\text{ ion/cm}^2$ . This different behaviour points to another degradation path which could be explained if the band at  $1117\text{ cm}^{-1}$  represents a specific part of the polymer backbone degrading faster than the structure parts linked to the other infrared signals. Due to the proposed

degradation mechanisms [90] the imide ring will be the first structure element which will be destroyed. It has also to be noted that a chain fraction of the polymer backbone at the imide ring leads to disappearance of the infrared signal of the imide ring. In contrast to that, the chain fraction at the ether bridge for example does not interact with the phenyl signals.

These points lead to the conclusion that the signal at  $1117\text{ cm}^{-1}$  represents, most probable, the imide ring and the other three peaks are associated to the phenyl structure of the polymer.

For further discussions, the peak at  $1117\text{ cm}^{-1}$  is assigned to the imide degradation and the signal at  $725\text{ cm}^{-1}$  is ascribed to represent the aromatic part of the polymer.

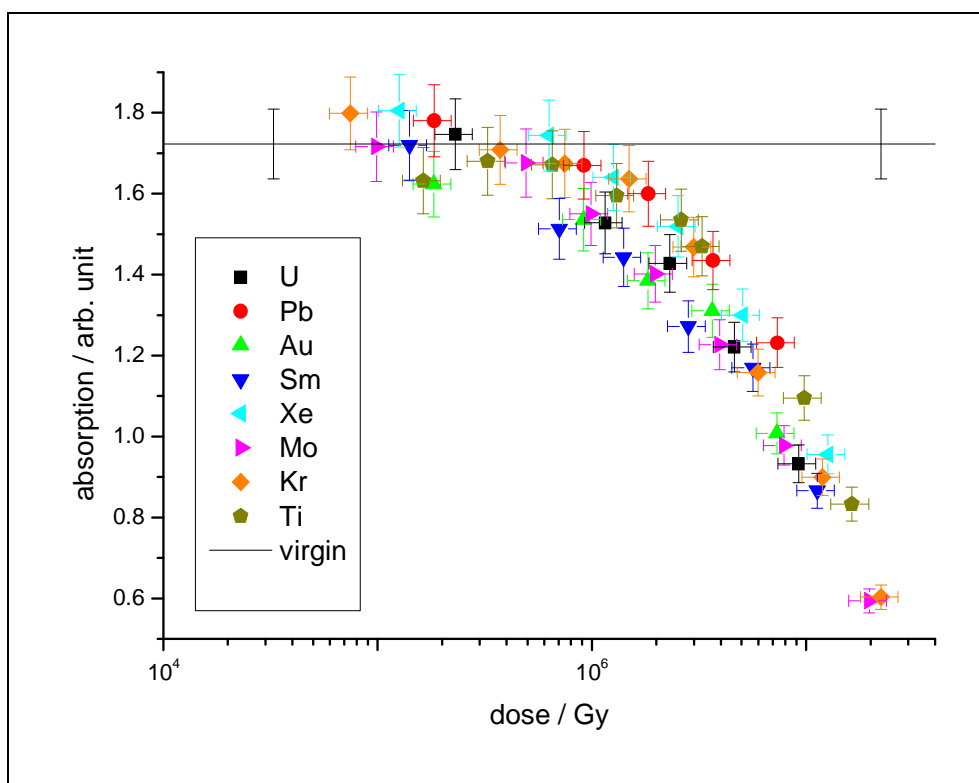


**Figure 30: Absorption of imide band ( $1117\text{ cm}^{-1}$ ) as a function of dose from irradiation with various ions and energies.**

Figure 30 represents absorption vs. dose plot of the infrared band at  $1117\text{ cm}^{-1}$  which is assigned to the imide group. The uniform trend indicates that the decay is scalable by the deposited energy and independent of the projectile mass. Up to a dose of  $\sim 1\text{ MGy}$ , the imide signal scatters around  $\pm 10\%$  of the initial absorbance. Above this dose all irradiations result in a significant decrease of absorbance

Figure 31 shows also the degradation of the polymer indicated by the infrared band at  $725\text{ cm}^{-1}$  which is most probably addressed to the phenyl groups of the polymer. The diagram indicates the same uniform tendency as discussed for Figure 30 and underlines that the analysed degradation process is independent of the projectile ion mass and scaleable by the dose.

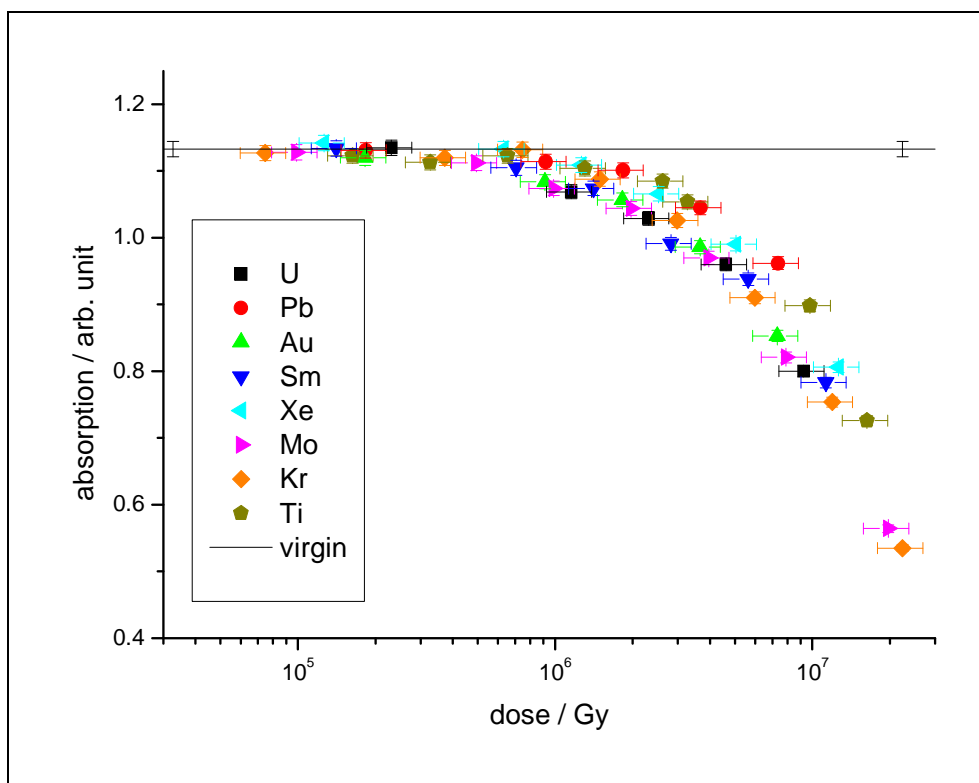


**Figure 31: Absorption of imide band ( $725\text{ cm}^{-1}$ ) as a function of dose from irradiation with various ions and energies.**

Furthermore the decay of the absorbance measured for the imide band at  $1117\text{ cm}^{-1}$  shows more straggling in comparison to the signal at  $725\text{ cm}^{-1}$  probably related to the more complicated analysis of the  $1117\text{ cm}^{-1}$  signal (double-peak shape). The more pronounced degradation of the imide band is consistent with the proposed degradation mechanism where the imide ring is opened in the first step in contrast to the phenyl ring structure (see 3.3).

### 5.1.2 UV/Vis spectroscopy

The irradiation induced degradation of polyimide leads to a discoloration of the material. The initial amber-coloured polyimide obtains a dark graphite luster with dose increase. Figure 32 shows photos of Kapton foils before (a) and after an irradiation with  $2 \times 10^{12}$  Mo ions/cm<sup>2</sup> (d). This discoloration appears in the UV/Vis spectra.

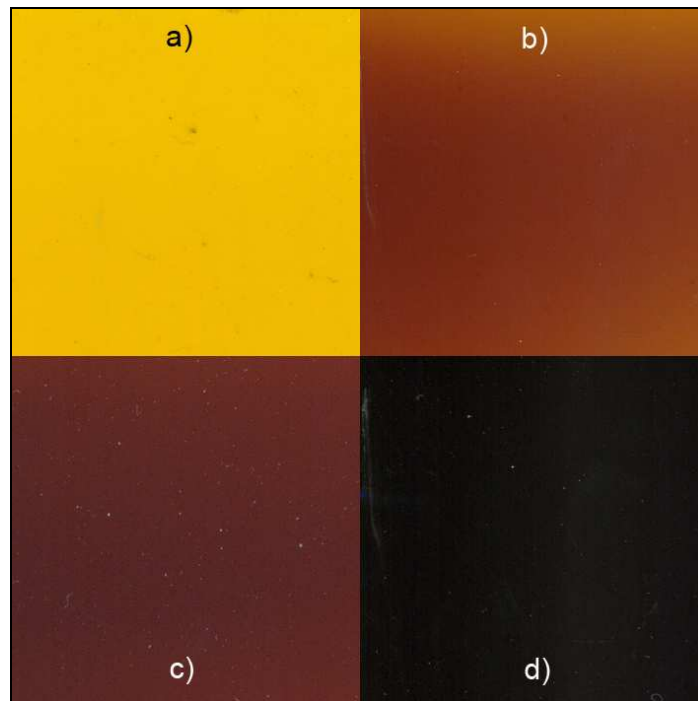
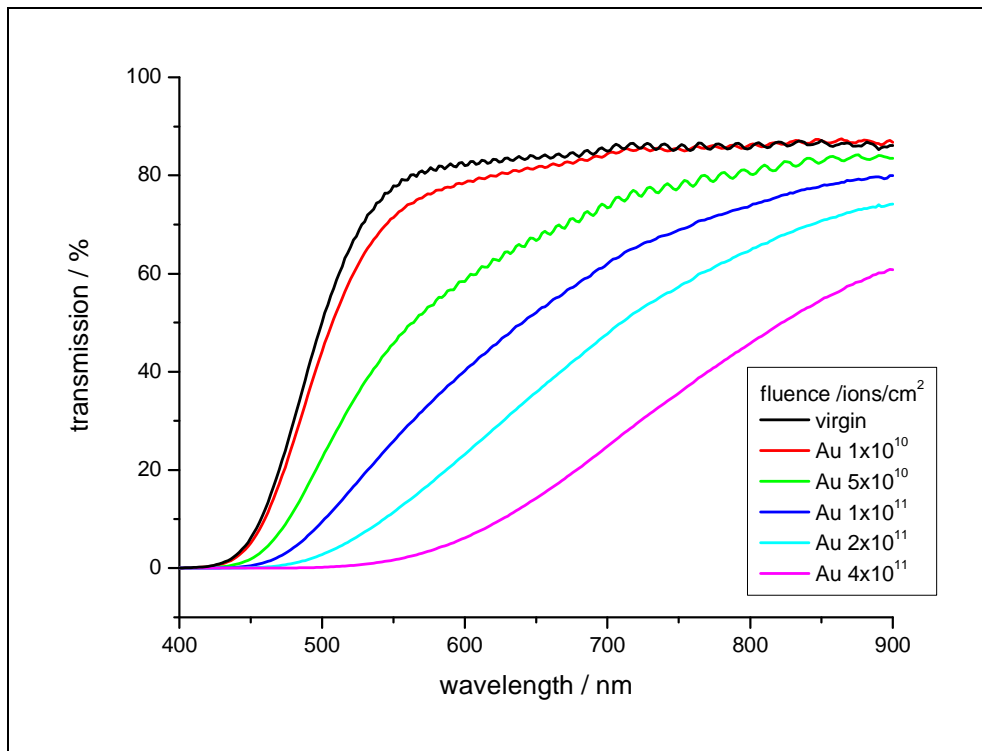


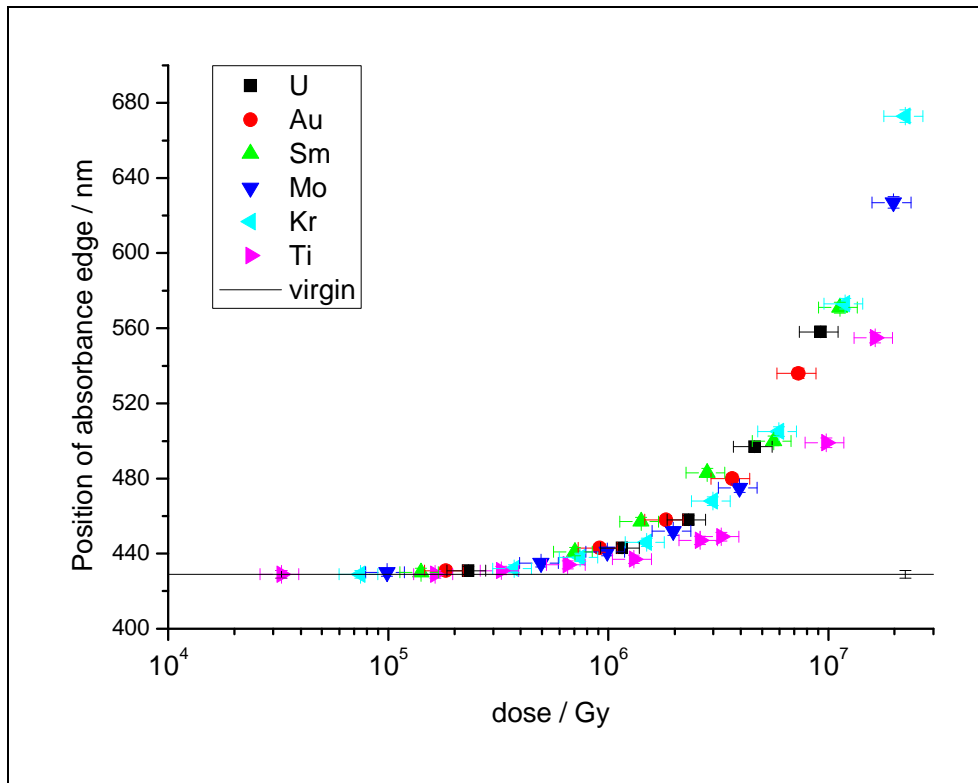
Figure 32: Photos of Kapton foils (12  $\mu\text{m}$  thick): virgin (a) and after irradiation with Mo ions with 5.2 MeV/u at different fluences:  $2 \times 10^{11}$  ions/cm<sup>2</sup> (b),  $4 \times 10^{11}$  ions/cm<sup>2</sup> (c), and  $2 \times 10^{12}$  ions/cm<sup>2</sup> (d).

Figure 33 presents the UV/Vis transmission spectra of virgin and irradiated polyimide foils. There is a total absorbance in the ultraviolet region which merges into an absorbance edge at 425 nm for virgin polyimide. The total transmission abates and the absorbance edge shifts to higher wavelengths under irradiation. The shift of the absorbance edge points to a carbonization of the material [86, 91].



**Figure 33: UV/Vis spectrum of 12  $\mu\text{m}$  polyimide foils irradiated with different fluences of 5.2 MeV/u Au ions.**

There are different analysing methods of the full spectrum to exemplify the absorbance edge shift and consequently the degradation process. One method is to use the inflection point of the spectrum to evaluate the absorbance-to-transmission transition [92]. Another approach is to fix a wavelength and to follow the increase of absorption compared to the virgin foil [53]. Especially this method is important for fitting the degradation process based on the theory that each ion impact creates new chromophores which absorbs at the evaluation wavelength. The third method, which is used here, indicates the shift of the absorbance edge by analysing the wavelength at which the transition starts to increase. In contrast to the other methods, this evaluation method has the advantage that it can also be used for highly degraded material and larger wavelength shifts.



**Figure 34: Position of the absorbance edge analysed with transmission UV/Vis spectroscopy of Kapton foils after irradiation with different ions plotted versus the dose.**

Figure 34 shows the evaluated UV/Vis spectroscopy data which indicate the wavelength of the absorbance edge as a function of dose. The uniform trend points to a clear dependency of the deposited energy. Only the high fluence sample irradiated with Ti ions which represents the lowest tested projectile mass, show a slightly weaker rise of the curve. A significant material change occurs above 1 MGy. The results confirm the analysis of the infrared spectroscopy. The UV/Vis spectroscopy presents a very homogenous degradation curve showing a clear correlation between the analysed degradation and the dose.

### 5.1.3 Tensile strength

Figure 35 exemplarily shows samples exposed to different ion beams (Au, Sm, and Ti) and analysed by tensile strength measurements, stress/strain curves of 25  $\mu\text{m}$  thick Kapton foils irradiated with Au ions of various fluences. The measurements of the other ion irradiations indicate similar trends. The stress/strain curve of non-irradiated Kapton foils are characterised by a short linear region up to a strain of approx. 1 % followed by continuous flatten rise until the breaking point. After irradiation, all samples exhibit an elongation of the linear part of the stress/strain curve up to a strain region between 1.5 and 1.8 %. With increase of fluence, the stress/strain curves of the irradiated samples show a weaker rise with a constant gradient. The high fluence samples ( $4 \times 10^{11}$  Au ions/ $\text{cm}^2$ ) become extremely brittle and indicate a different curve shape ending up at break directly after a proportional rise.

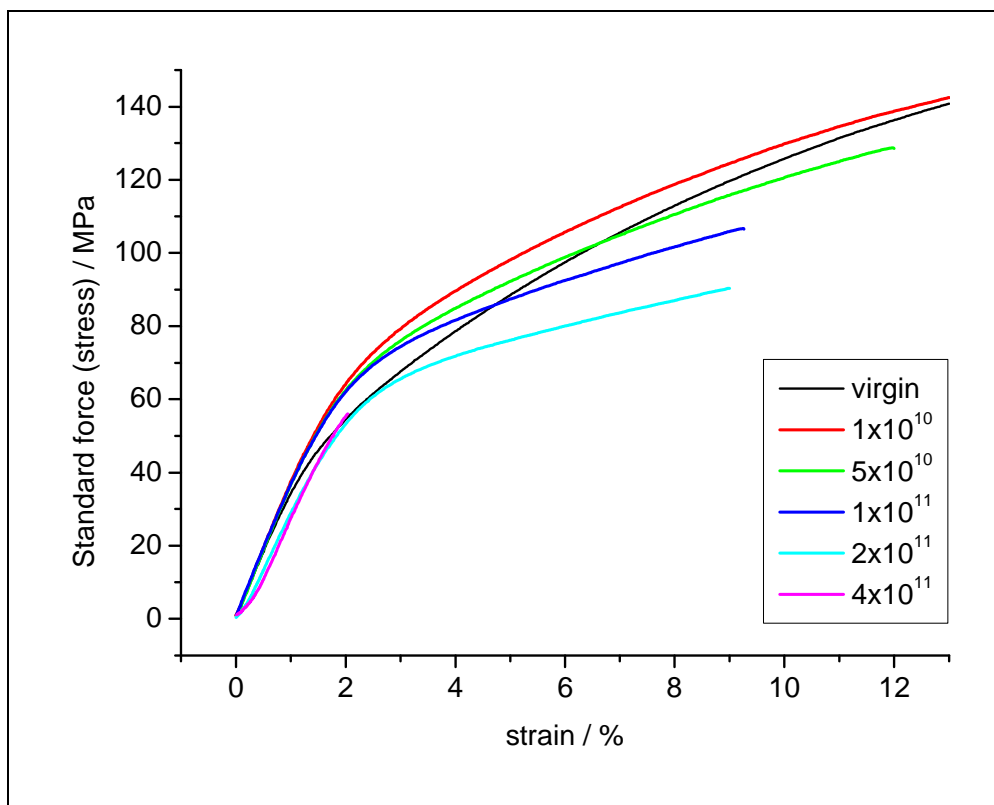


Figure 35: Stress/strain curves of polyimide foils (25  $\mu\text{m}$ ) after irradiation with 11.1 MeV/u Au ions.

In the following, the stress/strain curves are analysed with respect to breaking stress, breaking strain and the Young's modulus. In order to compare the effects of different beams, the results are plotted as a function of dose instead of fluence. The uniform behaviour demonstrates that the material modification concerning the mechanical properties as characterised before, is basically dependent of the deposited energy.

Figure 36 shows the breaking stress values of the different irradiation series as a function of dose. A significant change over all irradiation series occurs at a dose of 1 MGy. At a dose of 10 MGy the breaking stress decrease has decreased by a factor of 2.5 from originally 150 MPa to approx. 60 MPa.

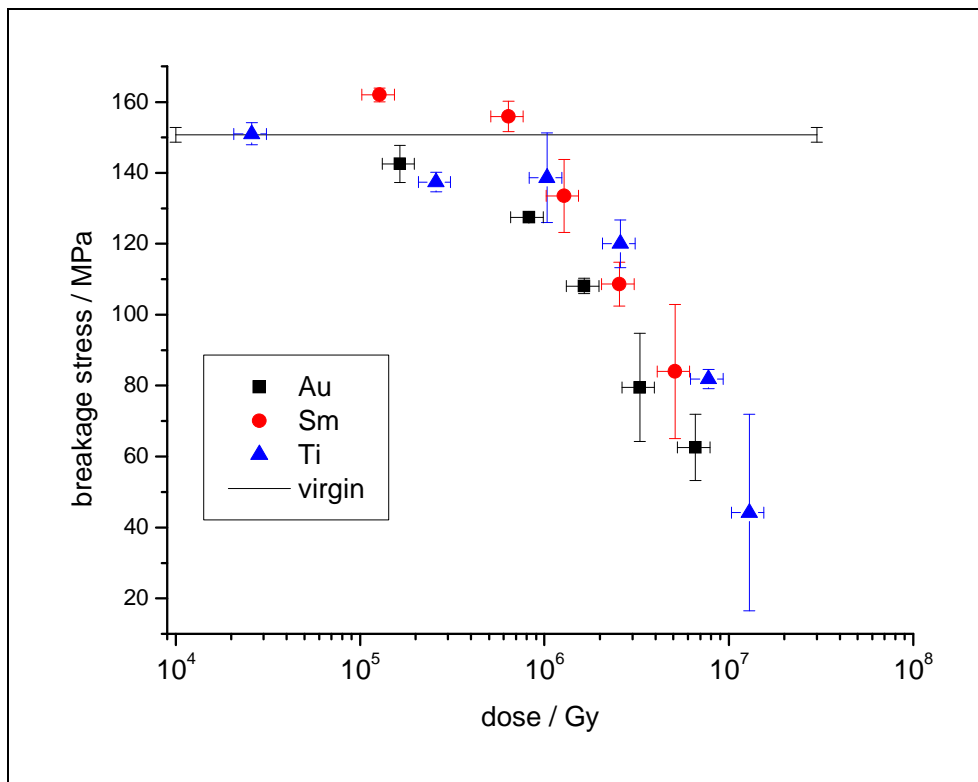


Figure 36: Breaking stress of 25  $\mu\text{m}$  thick Kapton foils after irradiation with different ions.

The corresponding breaking strain is displayed in Figure 37 exhibiting a similar trend. The large fluctuation of the values at doses below 1 MGy is not understood. At 1 MGy the breaking strain decreases to 75 % of the virgin measurement. For higher doses data follow an exponential decrease.

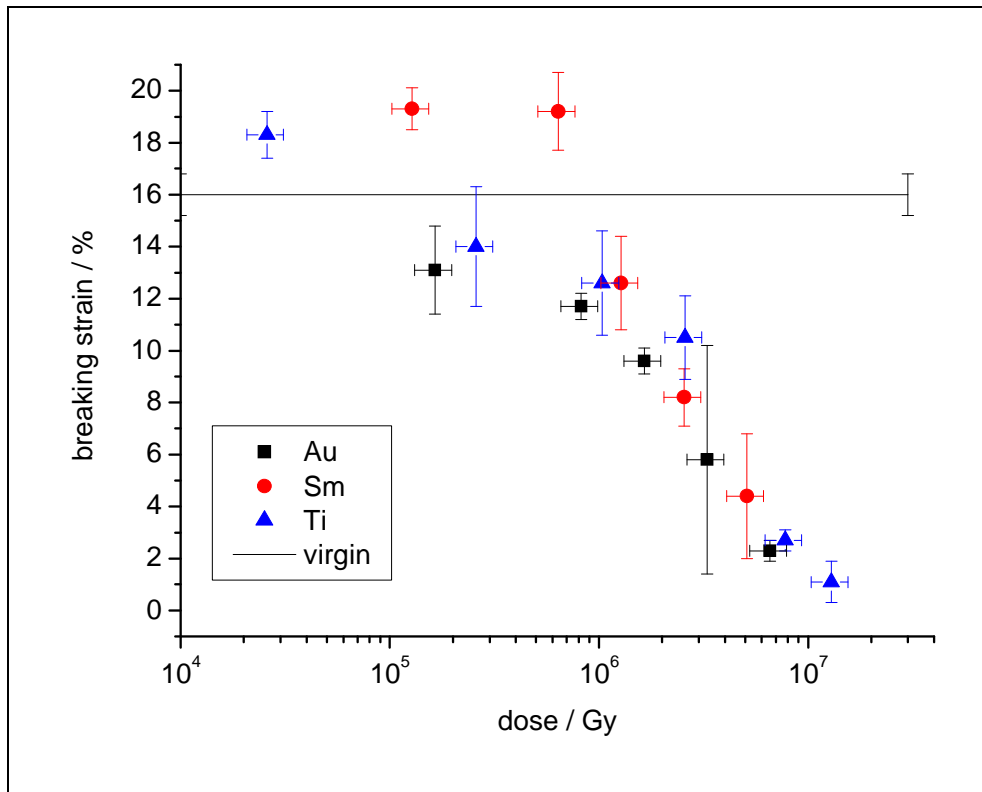


Figure 37: Breaking strain of 25 μm thick Kapton foils after irradiation with different ions.

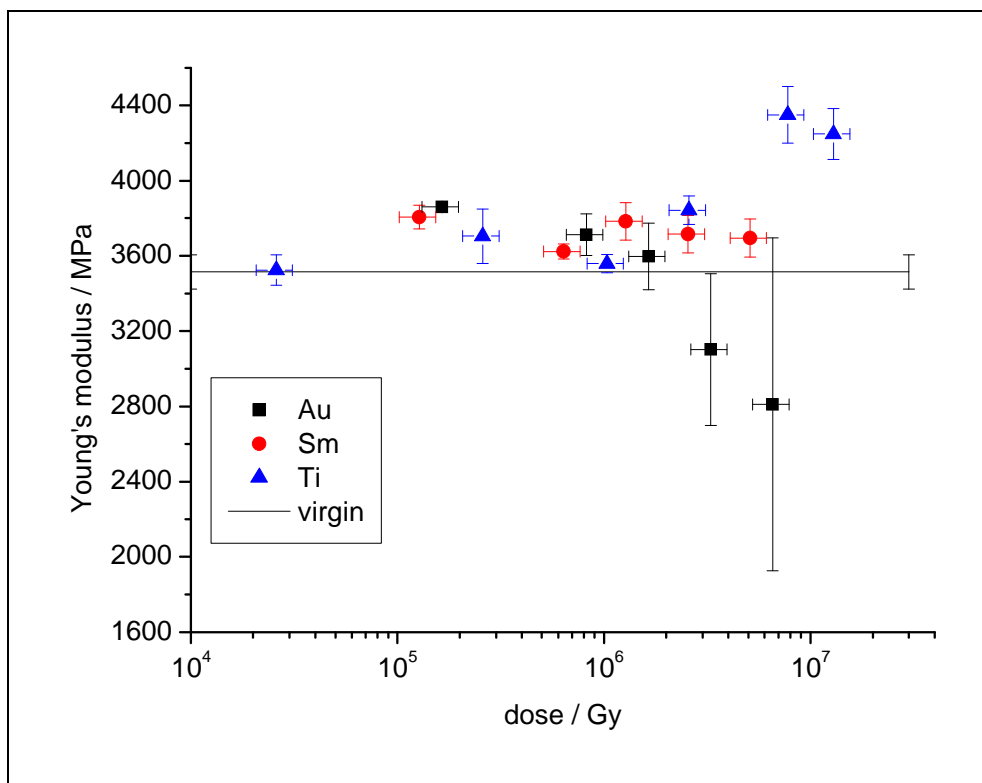


Figure 38: Young's modulus of 25 μm thick Kapton foils after irradiation with different ions.

Figure 38 shows the Young's modulus calculated based on the gradient described by linear part of the beginning stress/strain curve. The Young's modulus indicates no clear trend with respect to the irradiation. This is also reflected in the stress/strain curves (see Figure 35) by presenting similar gradients in the proportional regime. Only the high fluence samples of the Au and the Ti series show opposed tendencies whose causes are not understood yet. An explanation could be the algorithm of the evaluation method. It was based on a DIN method normally used for thicker and stiffer material samples.

#### 5.1.4 Dielectric relaxation spectroscopy

The following four figures show the dielectric relaxation spectra of 50  $\mu\text{m}$  polyimide samples irradiated with various fluences of Ti, Mo, Sm, and Au. The permittivity  $\epsilon'$  (a), the complex permittivity  $\epsilon''$  (b), and the conductivity  $\sigma'$  (c) are plotted for each fluence. The results of the dielectric relaxation spectroscopy are presented and discussed separately for each irradiation series due to the fact that the results can not be scaled by the dose.

##### *Ti irradiation (Figure 39)*

The permittivity shows a slight decrease with increasing frequency (Figure 39 a). The irradiation up to a fluence of  $2 \times 10^{11}$  ions/cm<sup>2</sup> leads to a decrease of  $\epsilon'$  compared to the virgin material curve. After passing this minimum the increase of fluence causes an increase of the permittivity curves. The fluctuation of the curves could be related to the error of the method. Due to the fact that the effect of decrease of the permittivity below the virgin material is very small, it is not interpreted as a result of the irradiation. The value of the virgin polyimide foil at 1 kHz ( $\epsilon = 3.35$ ) is in good agreement with the literature value ( $\epsilon = 3.4$ ).

The complex permittivity displayed in Figure 39 b indicates a different behaviour of the virgin foil in comparison to the irradiated polymer independently of the fluence. The virgin polymer shows a maximum around 30 and 800 Hz which disappears after irradiation. It could not be identified without measuring dielectric relaxation in temperature dependence. The peak could be a matter of a polymer relaxation or a surface polarization effect (Maxwell-Wagner). Furthermore, all spectra show the tendency of a second maximum at high frequency which is not changed by irradiation. The irradiated samples indicate an over all increase of  $\epsilon''$  with an increase of fluence.

The conductivity tends to increase with increasing frequency (Figure 39 c). The irradiation leads again to an overall increase of the conductivity curves. The curves show no plateau behaviour at 0.1 Hz which indicates that the DC conductivity is not reached. Nevertheless, the high fluence irradiation causes a conductivity which is 20 times higher at 0.1 Hz than it is compared to the virgin polyimide.

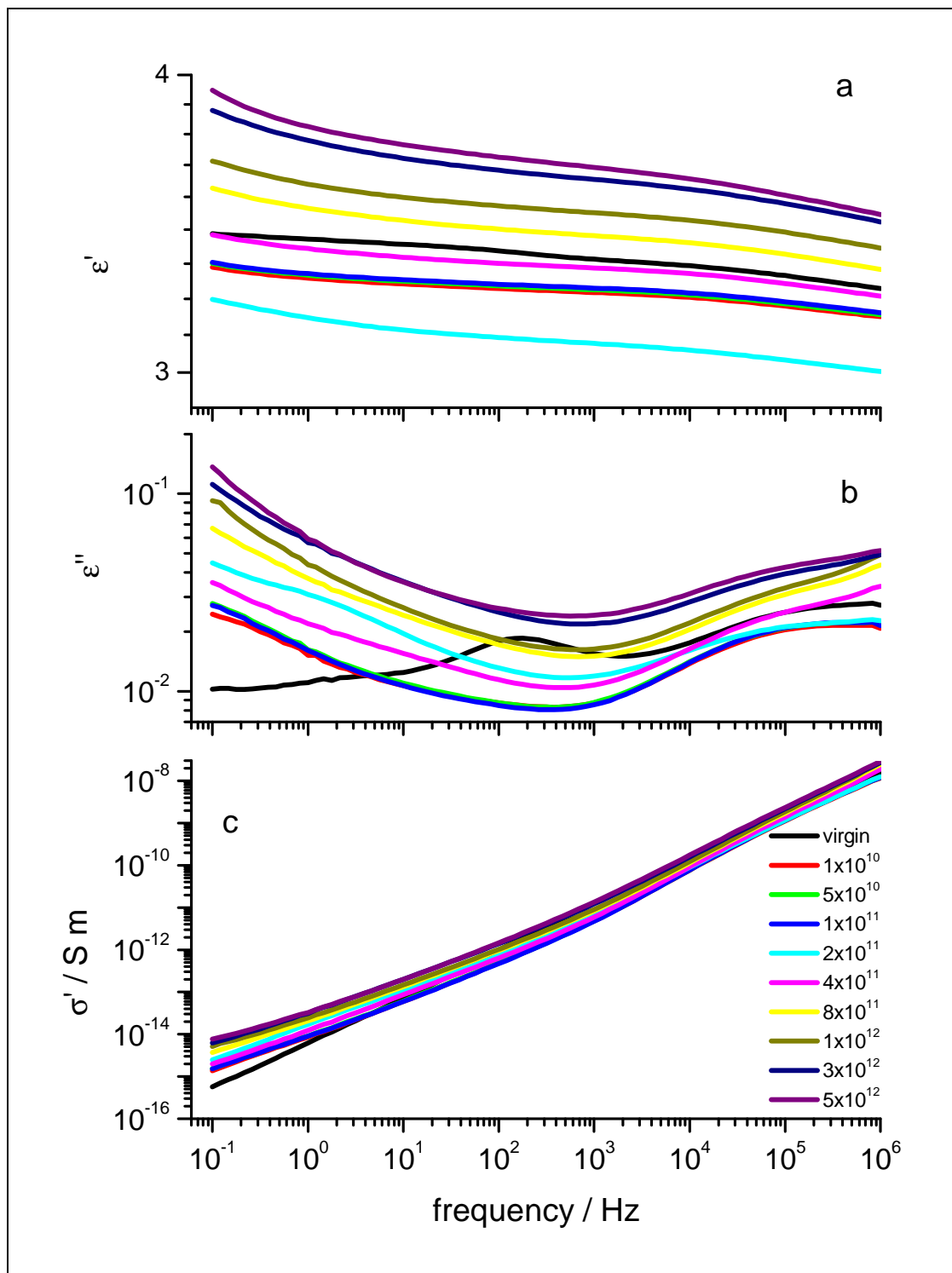


Figure 39: Dielectric properties as a function of frequency of 50  $\mu\text{m}$  polyimide foils irradiated with Ti ions: permittivity  $\epsilon'$  (a), complex permittivity  $\epsilon''$  (b), and conductivity  $\sigma'$  (c).

### *Mo irradiation (Figure 40)*

The permittivity of the virgin polyimide shows the same trends as discussed for the Ti irradiation but due to the scaling of the diagram it seems to be independent of the frequency. The permittivity increases considerably above an irradiation level of  $2 \times 10^{11}$  ions/cm<sup>2</sup> primarily indicated at low frequency (Figure 40 a). At 0.1 Hz,  $\epsilon'$  increases up to a value of 12 which is an increase by a factor of 4 in comparison to non-irradiated polyimide.

Figure 40 b illustrates the  $\epsilon''$  curves of the Mo irradiation series. The diagram clearly shows the relaxation peak at 200 Hz which disappears under irradiation. The red curve ( $1 \times 10^{10}$  ions/cm<sup>2</sup>) still shows a slight peak shape, but at a fluence of  $5 \times 10^{10}$  ions/cm<sup>2</sup> the peak has disappeared completely. The second maximum at high frequency is not influenced by irradiation though leads the irradiation with rising fluence to an over all increase of the curves. It is especially clarified at low frequencies where  $\epsilon''$  increases up to three orders of magnitude.

The conductivity measurement of the non-irradiated foil points also to a maximum at 200 Hz illustrated in the  $\epsilon''$  curves. The conductivity curves demonstrate expected trends: a) the conductivity increases with the frequency and b) the conductivity also increases with increasing fluence (Figure 40 c). The Mo irradiation series indicates a straightforward, nearly linear dependency between the fluence and the conductivity.

### *Sm irradiation (Figure 41)*

The permittivity measurements of the Sm irradiated samples (Figure 41 a) show a similar trend in comparison to the lighter ion irradiation, but the absolute increase of the permittivity after an irradiation with  $2 \times 10^{12}$  ions/cm<sup>2</sup> at 0.1 Hz reaches a value over 100 which is by far the highest value measured. The sequence of the medium fluences ( $1 \times 10^{11}$  –  $4 \times 10^{11}$  ions/cm<sup>2</sup>) does not reflect exactly the expected tendency.

The  $\epsilon''$  spectra exhibit an increase induced by the irradiation (Figure 41 b). The small dip in the curve of the virgin foil at 50 Hz results from the power supply system frequency and thus is consequently a systematic error (this also applies also for the 50 Hz dip in the virgin conductivity curve). Remarkable is the tremendous increase already at low fluences. The sample irradiated with  $1 \times 10^{10}$  ions/cm<sup>2</sup> (red curve) shows again a peak form at 200 Hz which

resembles that one of the virgin sample. The peak form becomes weaker but is still observable. After an irradiation with  $5 \times 10^{10}$  ions/cm<sup>2</sup> the peak shape disappears completely.

Figure 41 c shows the conductivity measurements of the Sm irradiation. The tendency has already been discussed above in context with the  $\epsilon''$  values. Particularly remarkable is the increase of conductivity at 0.1 Hz by nearly five orders of magnitude for the high fluence sample ( $2 \times 10^{12}$  ions/cm<sup>2</sup>). Also remarkable is the curve shape of this sample: it nearly reaches a plateau at low frequency which means that the measured conductivity is close to the DC conductivity.

#### *Au irradiation (Figure 42)*

The permittivity measurement results of the Au irradiation are displayed in Figure 42 a. The two high fluence samples with  $2 \times 10^{11}$  ions/cm<sup>2</sup> and  $4 \times 10^{11}$  ions/cm<sup>2</sup> exhibit an unexpected behaviour due to the fact that the curves stay underneath the blue  $1 \times 10^{11}$  ions/cm<sup>2</sup> curve. In comparison to the other curves, the two high fluence measurements run flatter in the low frequency region.

The irregularities of the high fluence samples can also be seen in the  $\epsilon''$  curves (Figure 42 b). The curve-shape of these samples shows an unusual form which differs from the other samples. Nevertheless, the measurements indicate the expected general trend, that  $\epsilon''$  shows even after low fluence irradiation a massive increase primarily at low frequency.

The conductivity curves plotted in Figure 42 c show a tremendous increase already at low fluences. Unusual is the sequence of the curves: the curves of the foil irradiated with  $1 \times 10^{10}$  ions/cm<sup>2</sup> (green) and  $1 \times 10^{11}$  ions/cm<sup>2</sup> (blue) stay on top of each other and the two high fluence samples (turquoise and pink) progress beneath.

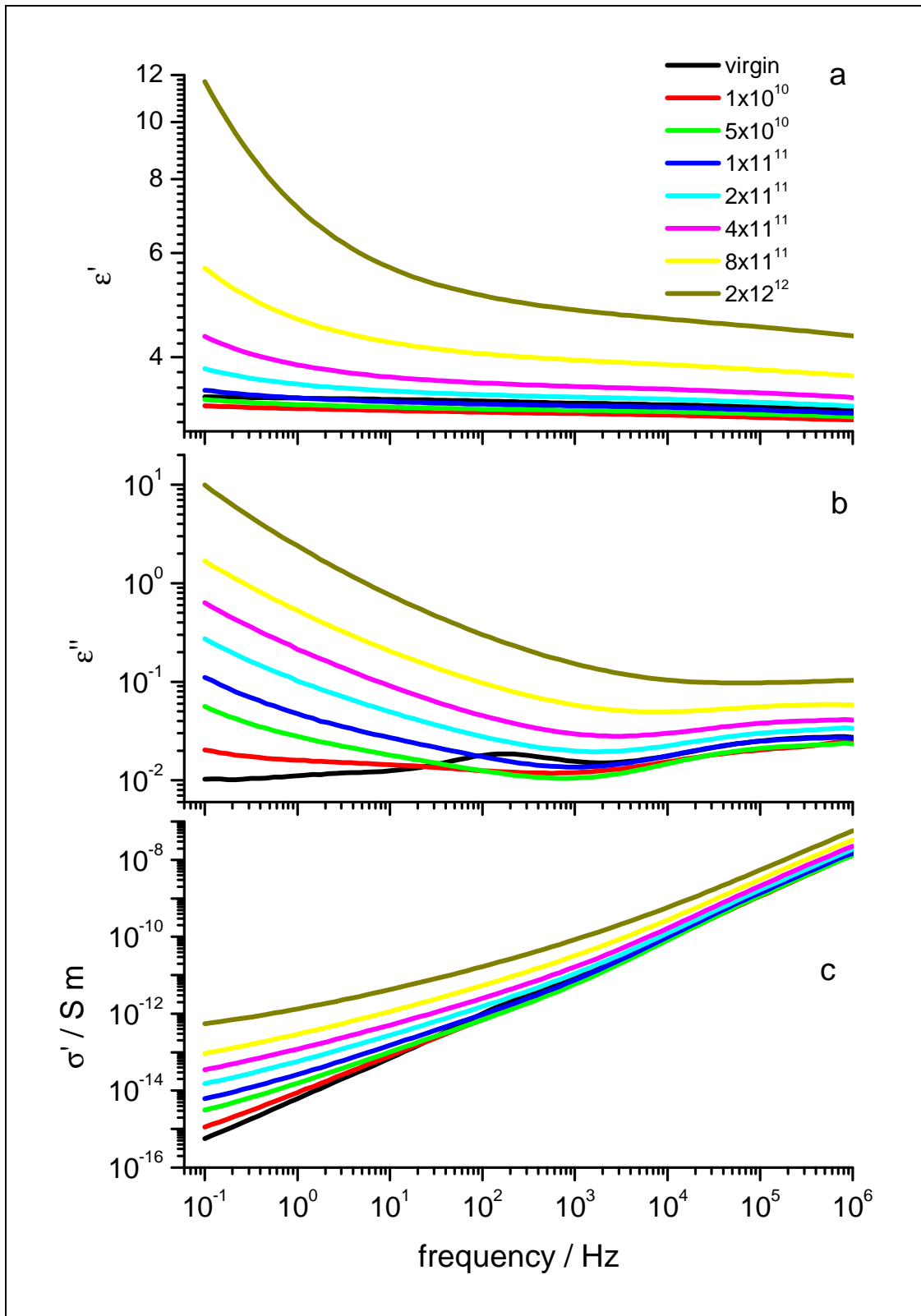


Figure 40: Dielectric properties as a function of frequency of 50  $\mu\text{m}$  polyimide foils irradiated with Mo ions: permittivity  $\epsilon'$  (a), complex permittivity  $\epsilon''$  (b), and conductivity  $\sigma'$  (c).

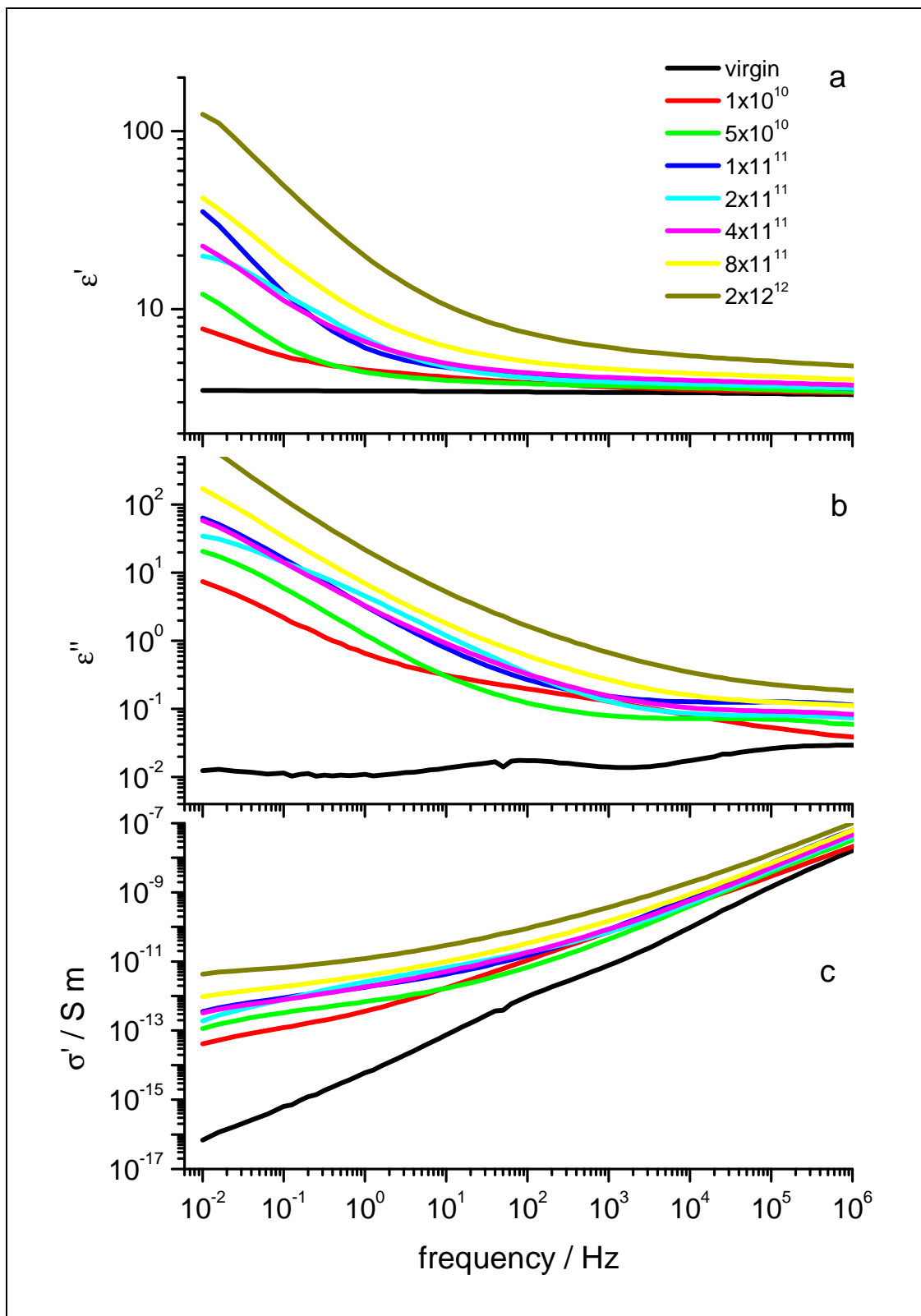


Figure 41: Dielectric properties as a function of frequency of 50  $\mu\text{m}$  polyimide foils irradiated with Sm ions: permittivity  $\epsilon'$  (a), complex permittivity  $\epsilon''$  (b), and conductivity  $\sigma'$  (c).

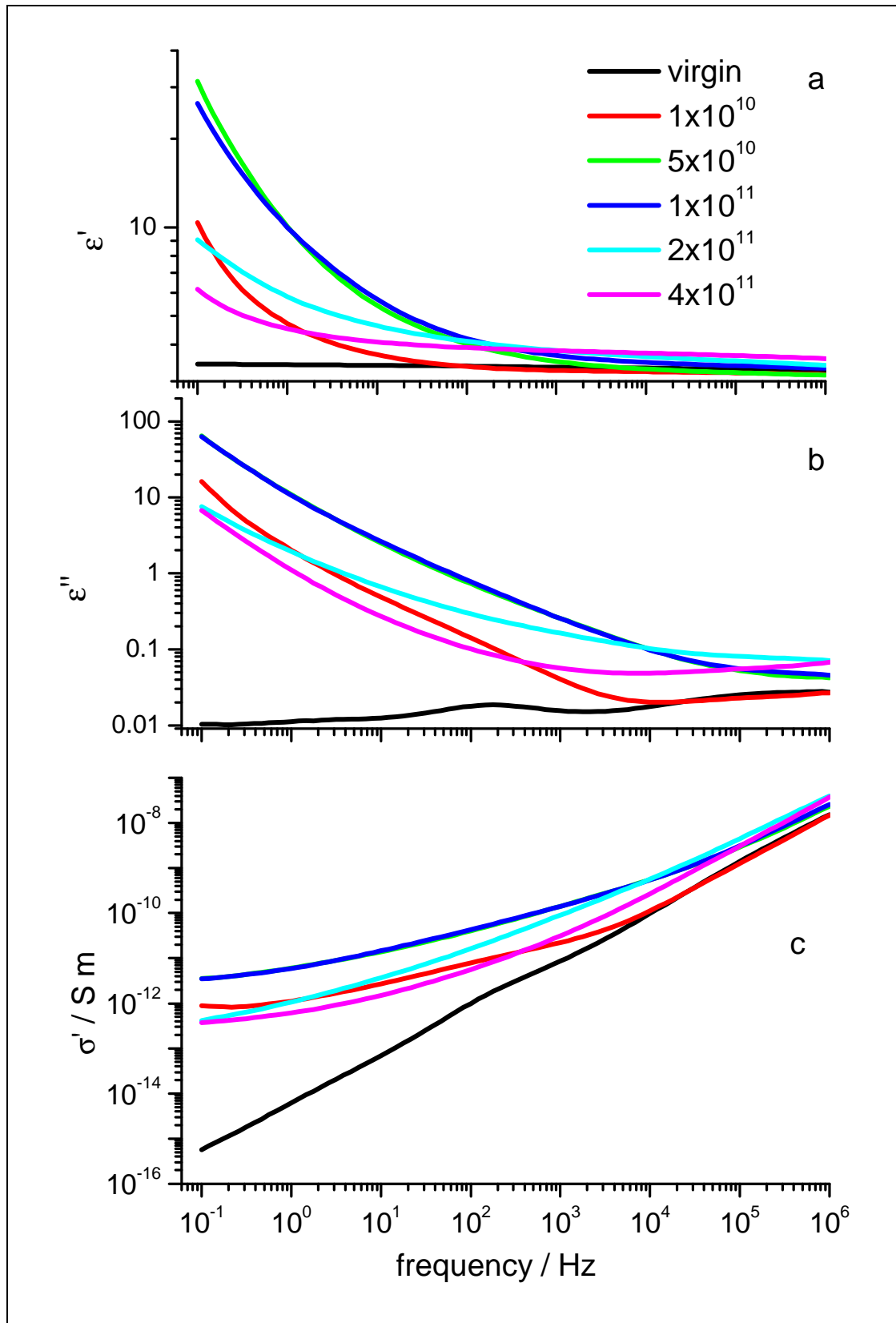


Figure 42: Dielectric properties as a function of frequency of 50  $\mu\text{m}$  polyimide foils irradiated with Au ions: permittivity  $\epsilon'$  (a), complex permittivity  $\epsilon''$  (b), and conductivity  $\sigma'$  (c).

Because the polymer will be used as an electric insulator, the conductivity results of the dielectric measurements are of main interest. The following two figures 43 and 44 show a cut along the conductivity values at 0.1 Hz and at 1 kHz. The results at 0.1 Hz represent the lowest frequency measured and thus are as close to the DC conductivity as possible. The real DC conductivity could not be measured because a plateau region at low frequencies could not be reached in the measured range. The cut along 1 kHz defines the AC conductivity. The virgin sample possesses a value below some irradiated samples of the Ti and Mo irradiation series which have been traced back to the radiation induced disappearance of the relaxation peak at 200 Hz. The tail of the peak leads to an increase of the AC conductivity (at 1 kHz) of the virgin sample.

Both figures indicate projectile specific material modifications induced by the irradiation. The light Ti ions merely show a slight linear increase of conductivity which ends up by a negligible raise of the AC conductivity compared to the virgin polymer. The Mo irradiation series revealed a behaviour of a strong fluence dependent increase of conductivity. At fluences above  $1 \times 10^{12}$  ions/cm<sup>2</sup> the AC conductivity increases by one order of magnitude but the conductivity at 0.1 Hz shows a tremendous increase of three orders of magnitude. The Sm irradiated samples (red) already indicate an excursive increase at a fluence of  $1 \times 10^{10}$  ions/cm<sup>2</sup>. At both frequencies measured (0.1 Hz and 1 kHz) the conductivity keeps rather stable in a region clearly above the value of the non-irradiated foil. Only the sample irradiated with a fluence of  $1 \times 10^{12}$  ions/cm<sup>2</sup> indicates a significant increase. The Au samples display a similar trend. But the measurements portend to a decrease in conductivity after passing a maximum, especially displayed in the AC conductivity plot (Figure 44).

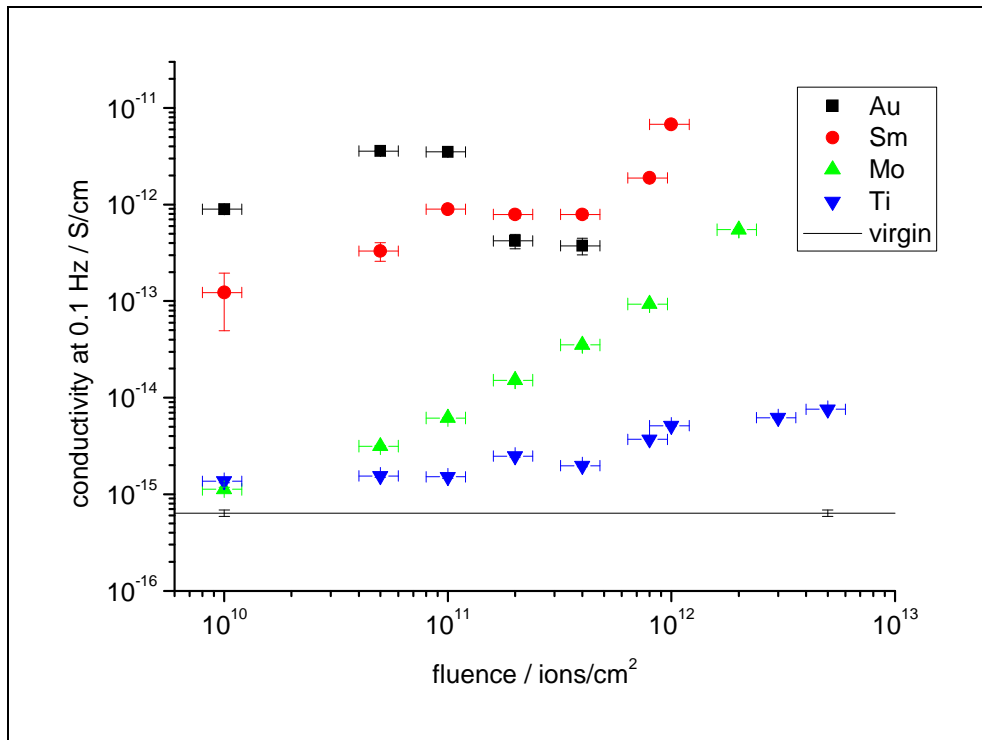


Figure 43: Conductivity measurements at 0.1 Hz of 50 μm thick Kapton foils after irradiation with different ions.

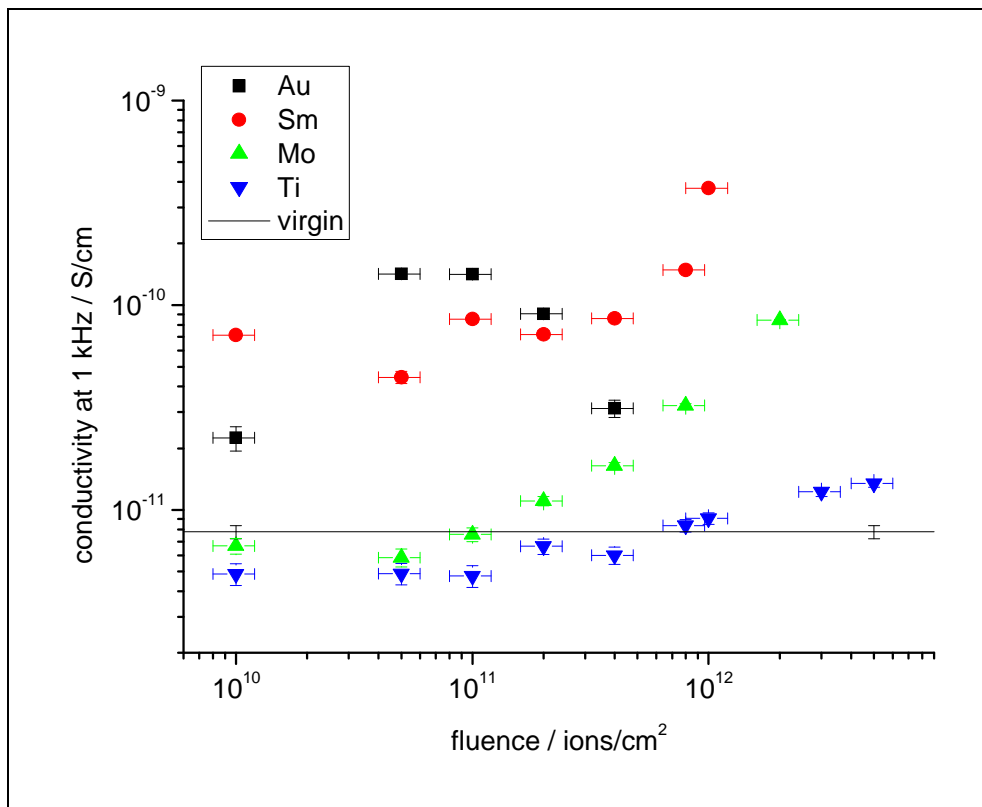
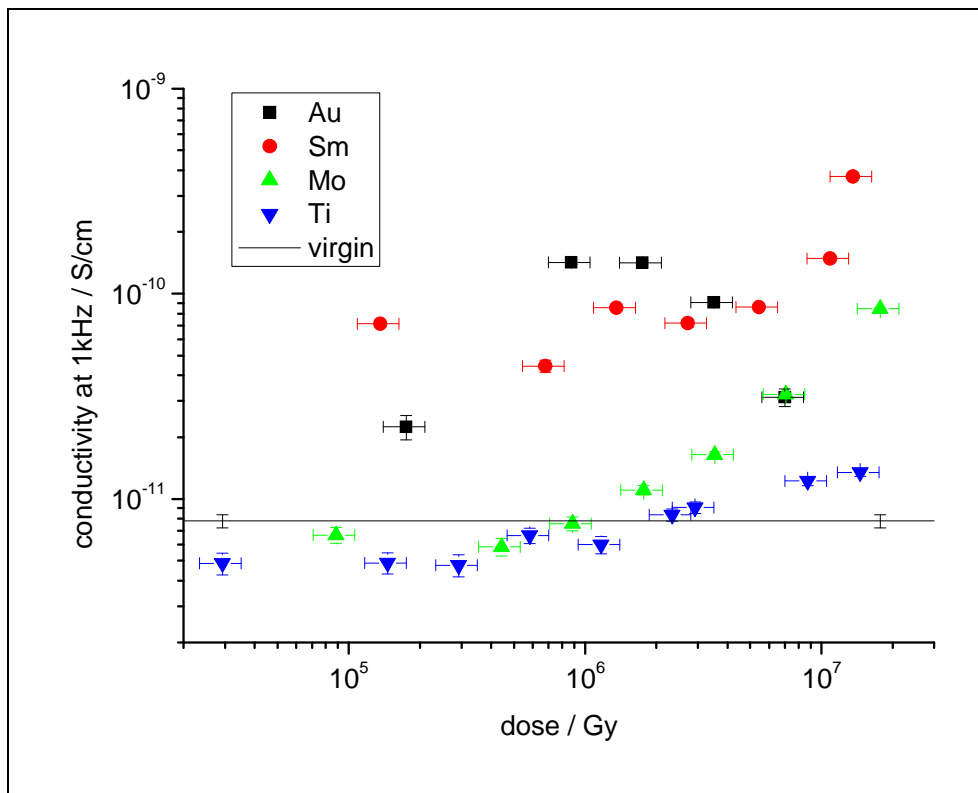


Figure 44: Conductivity measurements at 1 kHz of 50 μm thick Kapton foils after irradiation with different ions.

Figure 45 shows the AC conductivity depending on the dose. In contrast to the other analytical techniques applied, the plot of material change versus dose does not lead to a uniform trend. The AC conductivity indicates a clear dependence of the projectile on the radiation induced material modification. Particularly remarkable is the high AC conductivity of the samples irradiated with Sm and Au. It cannot be clearly distinguished which general trend would appear at higher doses, because the respective tendencies of the high dose Sm and Au samples go into different directions. It is important to note that due to the brittleness of the foils after irradiation, it was not possible to prepare samples with higher doses.



**Figure 45: Conductivity measurements at 1 kHz of 50  $\mu\text{m}$  thick Kapton foils after irradiation with different ions in plotted versus dose.**

The results of the electrical investigation introduce another kind of degradation which – in contrast to the optical and mechanical measurements – is not scalable with the dose. This kind of degradation behaviour is not understood yet. Therefore, an intensive comparison of the results with similar studies of the literature is absolutely necessary. In the past 15 years, several investigations about the radiation induced conductivity change are published [91, 93-96]. Costantini et al. present comprehensive measurements of the conductivity

modification after irradiation with several ions in the 1-MeV/u range. They show an increase in conductivity up to 18 orders of magnitude and process a new scale by taking the  $dE/dx_e$  square ( $S_e^2$ ) multiplied by the fluence ( $\Phi t$ ) and divided by the density square ( $\rho^2$ ). Costantini splits the insulator to conductor transition for the low energetic irradiation into four stages: (I) isolated paramagnetic centres appear without influencing the conductivity; (II) the polymer behaves like a semi-conducting polymer matrix filled with radiation defects and graphitic clusters; (III) hopping between the graphitic clusters dominates the conductivity process; (IV) a true 3D percolation of the disordered  $\pi$ -bonded clusters occurs. The interpretation is in basically confirmed by the results of ESR and Raman spectroscopy.

In his latest publication Costantini presents a comparison of foils after high energetic heavy ion irradiation like 1.1 GeV Ta with the results of the 1-MeV/u irradiation experiments [93]. The results do not fit into the insulator-to-conductor curve observed for the 1-MeV/u irradiated samples because even after high dose irradiation, the conductivity keeps a plateau in the region of  $10^{-7}$  S/cm. Costantini assumes the origin of this unexpected behaviour to be in the ion-velocity effect on damage which leads to a dilution of the deposited energy in the ion track. According to Costantini this induces a smaller  $sp^2$  cluster density prohibiting conductivity.

Figure 46 shows the measured results of this study in comparison with the Costantini data scaled with  $\Phi t \rho^{-2} S_e^2$ . Also this scale does not show an uniform trend of the irradiation series which differs in the projectile mass. The points of Constantini's experiments fit into the values measured for the heavy ions like Au and Sm. Even for low fluences, they show an increase of one order of magnitude and end up in an enormous increase in conductivity.

In an overall view of all studies, a more general explanation can be given by assuming two basic modifications induced by the irradiation: the creation of  $sp^2$  clusters is leading to a more graphite-like material (graphitisation). This process is well described by the four stage model of Costantini and counts by the 1-MeV/u insulator-to-conductor transition. Additionally it must be noted that for high energetic irradiation ( $\sim 10$  MeV/u) the deposited energy plays an important role. Even irradiation with low fluences leads to a dramatic increase in conductivity if the projectile passes a certain threshold of the deposited energy

( $dE/dx$ ). This would explain the excursive rise in conductivity for Sm, Au, and for the Ta irradiation of Costantini.

A second process is the destruction of the afore modified material occurring especially in case of irradiation with heavy ions under high velocities. A second hit could lead to a destruction of the formed 3D percolation of graphite-like clusters leading to a decrease of conductivity. This would explain the plateau region of the Sm and Au series where the growth of the graphite-like conductive structure and the destruction of this structure are in balance. It could also be an explanation for the downside trend of the high fluence Au samples.

The assumed explanation could not entirely explain the measured behaviour. In particular it remains unclear whether an increase or a decrease would follow at higher doses of irradiation with high energetic ( $\sim 10$  MeV/u) heavy ions ( $Z > 150$ ).

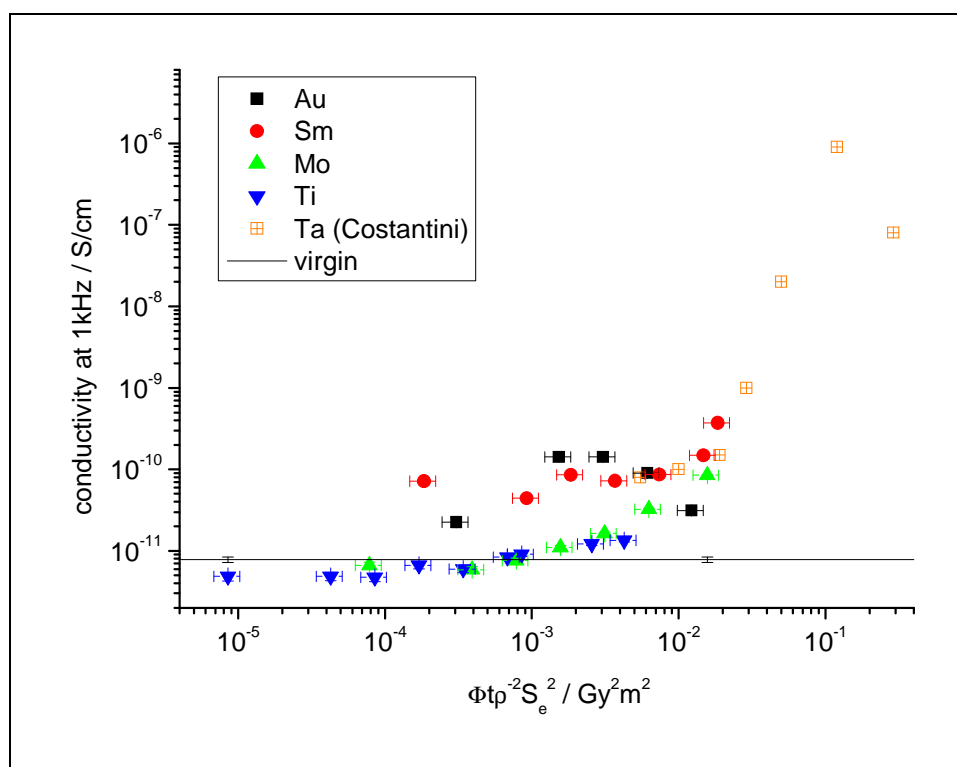


Figure 46: Conductivity measurements at 1 kHz of 50  $\mu\text{m}$  thick Kapton foils after irradiation with different ions in dependence of the  $\Phi t p^{-2} S_e^2$ . Also displayed are the results of Costantini [93] (AC conductivity after irradiation with Ta ions of 1.1 GeV total energy of 25  $\mu\text{m}$  polyimide foils).

Eventually it is important to note that the material modification concerning the conductivity induced by irradiation with ions in the regime of 10 MeV/u depends on the deposited energy. Even a rescaling to the dose or the Costantini scale

---

$\Phi t p^{-2} S_e^2$ , which captures the variably deposited energy, does not lead to a scale which explains the different trends of the different ion irradiations. Further on to note is the huge increase of conductivity after irradiation with Sm or heavier ions even at low fluences.

### 5.1.5 Mass loss analysis

Figure 47 shows the results of four irradiation series indicating the mass of the samples scaled by the dose. The results indicate a degradation trend which is clearly linked to the dose. This uniform trend points to an independency of the projectile mass. A significant material change occurs above 1 MGy where the mass is only lowered by  $\sim 0.7\%$ . After 10 MGy, the mass loss rises to round about 5.5%. The Pb irradiated samples are showing a slightly lower mass loss compared to the other samples.

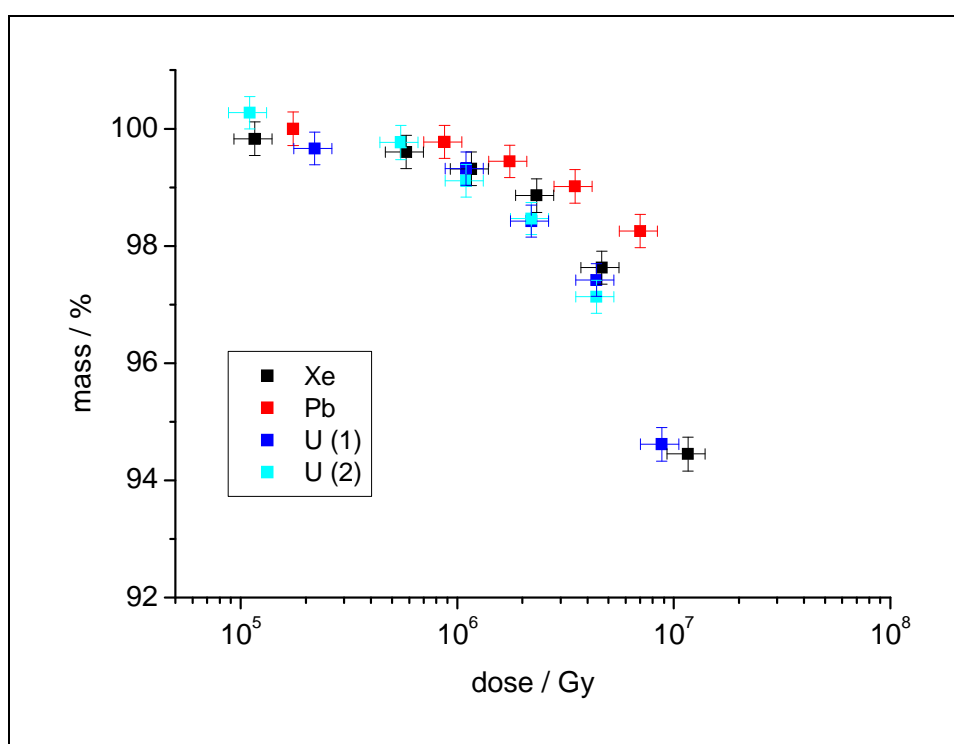


**Figure 47: Mass loss analysis performed by weighing the Kapton foils (50  $\mu\text{m}$ ) before and after irradiation with different projectile ions.**

The results confirm the analysis of the optical spectroscopy and the tensile strength tests. The mass loss analysis presents a very homogenous degradation curve but the percentage of mass loss or material change is lower than indicated with the other methods. This can be explained by the fact that the totally degraded or changed material will still have a residual mass.

It has to be noted that this methods need to be confirmed by additional irradiation experiments to deliver precise information about the absolute mass loss. Nevertheless, the first results show the feasibility of the experimental approach.

## 5.2 Low temperature experiments

### 5.2.1 In-situ FTIR spectroscopy

The cryogenic irradiation of 12  $\mu\text{m}$  thick Kapton foils with Kr ions basically shows the same overall degradation of the material as known from room temperature experiments (cp. 5.1.1). In the absorption FTIR spectra, this is indicated by a fluence dependent decrease of specific polymer bands. Bond breaking also leads to the creation of numerous unsaturated bonds.

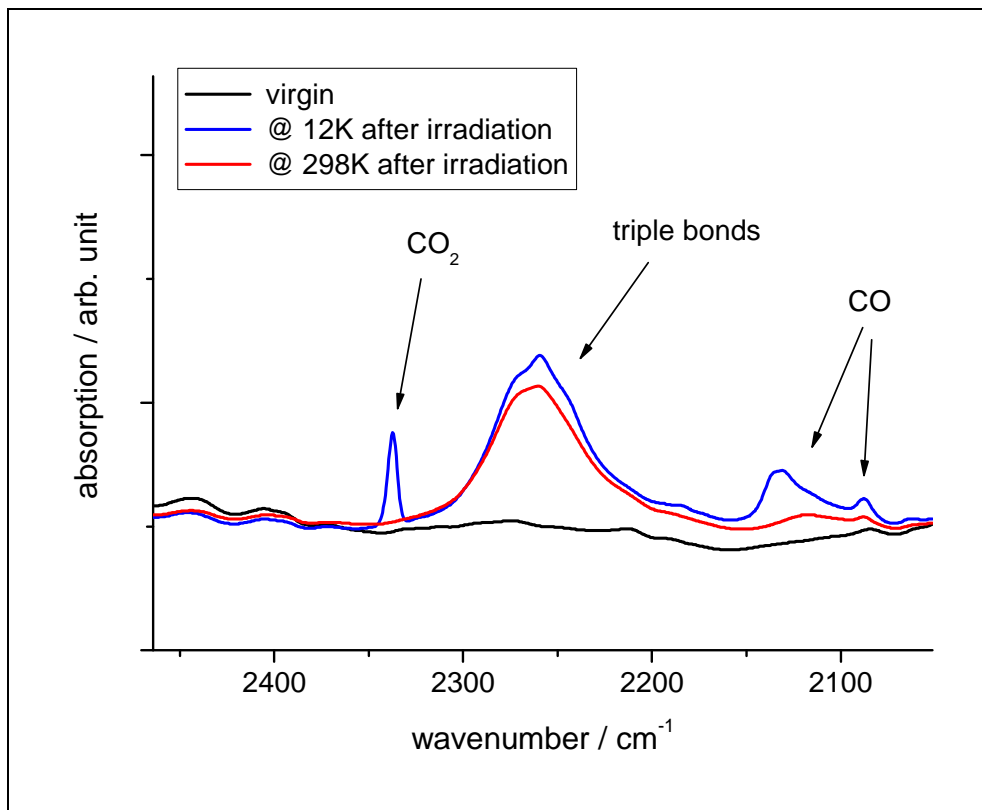


Figure 48: FTIR spectra of Kapton foils (12  $\mu\text{m}$ ) irradiated with  $1.6 \times 10^{12}$  Kr ions / $\text{cm}^2$  at 12 K before and after heat-up cycle in comparison with the spectrum of the sample before irradiation. Spectra were recorded under the Brewster angle ( $55^\circ$ ) to avoid surface interferences.

Figure 48 shows the infrared spectra between 2050 and 2450  $\text{cm}^{-1}$  recorded at the Brewster angle (avoiding interference undulations). Four bands appear in this wavenumber region at 2087, 2133, 2260, and 2337  $\text{cm}^{-1}$  after irradiation. The spectra give clear evidence of the formation of  $\text{C}\equiv\text{C}$  and  $\text{C}\equiv\text{N}$  by the absorption band at 2260  $\text{cm}^{-1}$ . This band intensity increases with fluence and is observed for RT as well as for cryogenic irradiation temperatures (Figure 48). Earlier studies under room temperature conditions demonstrated that

particularly swift heavy ions of sufficient energy loss can induce triple bonds such as  $C\equiv C$  and  $C\equiv N$  [97].

The spectra reveal new broad absorption bands at  $2087$  and  $2133\text{ cm}^{-1}$  arising from the stretching vibration modes of carbon monoxide (CO) and at  $2337\text{ cm}^{-1}$  from the asymmetric stretching mode of carbon dioxide ( $CO_2$ ). These peaks are only detected for samples irradiated and analysed at cryogenic temperatures. The intensities of these three bands increase with the fluence applied (Figure 49). The rise of the band shows that  $CO_2$  is formed and accumulated in the polymer during the irradiation because the molecule is immobilized inside the polymer. During the heat-up cycle, the band intensity decreases and finally disappears at around  $200\text{ K}$ . The continuous outgassing over a longer temperature range could be an evidence of  $CO_2$  diffusion from inside the bulk material towards the surface.

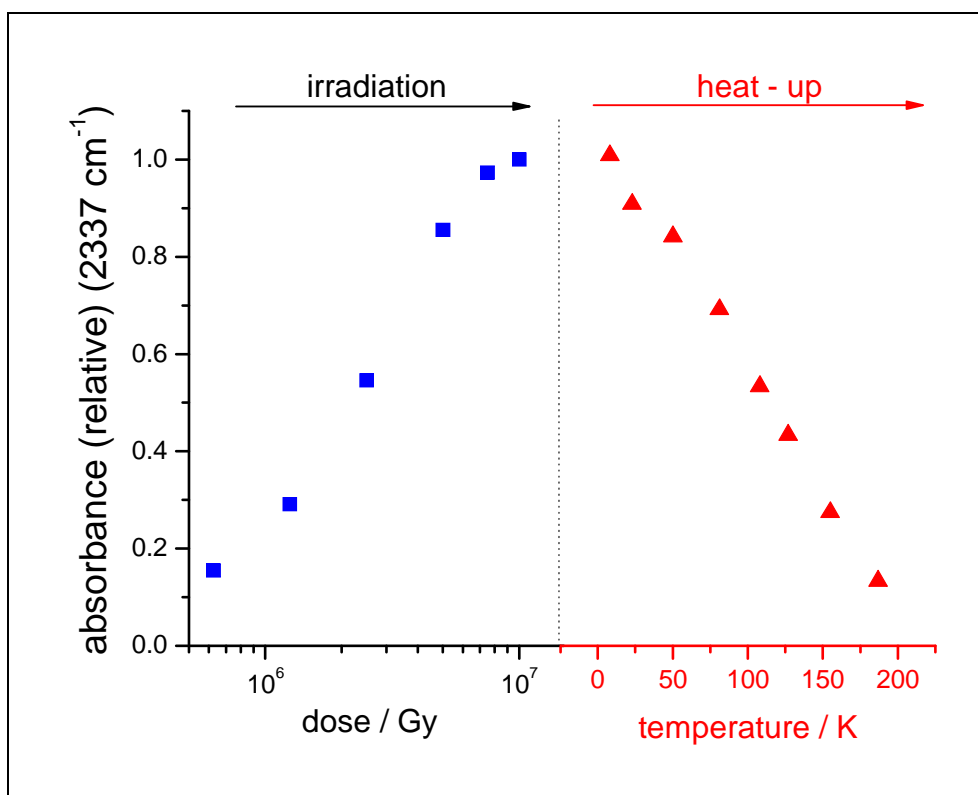


Figure 49: Intensities of the  $CO_2$  band (normalized to maximum intensity). Left: the blue squares increasing as a function of dose; right: the red triangles decreasing during the heat-up cycle.

### 5.2.2 Residual gas analysis during irradiation

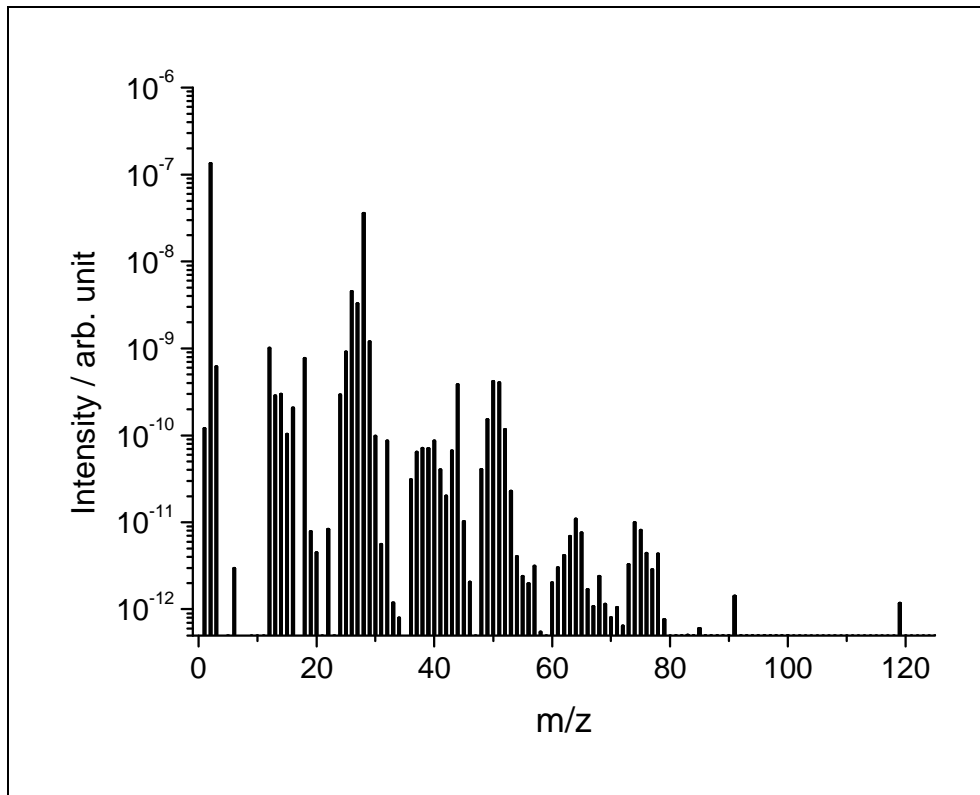


Figure 50: Online outgassing spectrum of Kapton foil (50  $\mu\text{m}$ ) during irradiation with 4.3 MeV/u Pb ions at 13 K.

A typical outgassing spectrum recorded during cryogenic irradiation ( $\sim 13$  K) with 4.3 MeV/u Pb ions is shown in Figure 50. The spectrum can be divided into three  $m/z$  sections:

- a.  $m/z < 35$  - *atoms and small molecules*: The most dominant outgassing masses are light ions in particular  $m/z = 2$  hydrogen ( $\text{H}_2$ ) and  $m/z = 28$  assigned to a mixture of carbon monoxide ( $\text{CO}$ ), ethene ( $\text{C}_2\text{H}_4$ ), and nitrogen ( $\text{N}_2$ ). Additionally, the mass signal  $m/z = 12$  from carbon exhibits large intensities resulting from fragmentation of  $\text{CO}$  and of short hydrocarbons ( $\text{C}_x\text{H}_y$ ). The group of signals from  $m/z = 24$  to 29 is assigned to  $\text{C}_2\text{H}_x$  hydrocarbons indicating the degradation of the aromatic ring system of the polyimide. The results of the heat-up cycle analysis lead to the conclusion that  $m/z = 28$  predominantly corresponds to  $\text{CO}$ .
- b.  $35 < m/z < 90$  - *molecules of medium-mass*: This region is characterised by masses grouped around the phenyl ring, hydrocarbon fragments  $\text{C}_n\text{H}_x$

(with  $n = 3-7$ ), and combinations of these molecules with nitrogen and oxygen.

- c.  $m/z > 90$  – *large polymer fragments*: Molecules with these high masses originate from large fragments of the main polyimide chain. The signal of  $m/z = 119$  can be assigned to benzoxazole which undergoes fragmentation into  $m/z = 91$  under elimination of CO. The observation of both mass signals confirms the proposed degradation mechanism [98]. This reaction path leads to CO as main outgassing product. Concordantly, signals of higher masses were not observed which indicates that larger polymer fragments are either not able to leave the bulk polymer or fragment before detection in the mass analyser.

Figure 51 focuses on the lower mass region up to  $m/z = 55$  and illustrates the differences between cryogenic and room temperature irradiations. Under cryogenic irradiation conditions, most of the mass signals are significantly smaller than at RT either due to reduced radiation damage or because the gaseous fragments are immobilized and thus stored in the polymer foil. The effect is in particular evident for the small hydro carbons ( $C_2H_x$ ) with  $m/z = 26$  and 27 but also occurs for  $m/z = 28$  and 44.

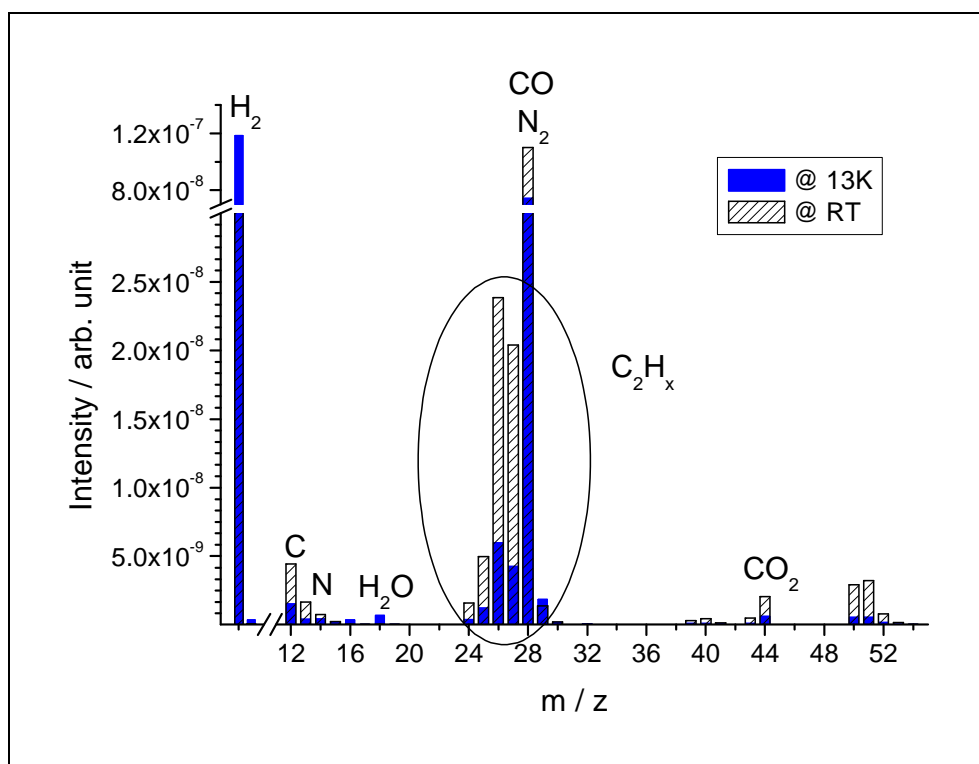


Figure 51: Outgassing spectra of Kapton foil (50  $\mu\text{m}$ ) at RT and 13 K recorded online during irradiation with 4.3 MeV/u Pb ions.

### 5.2.3 Residual gas analysis during heat-up cycles

After reaching the maximum fluence of  $1 \times 10^{12}$  ions/cm<sup>2</sup>, the sample holder with the irradiated foil was slowly heated while simultaneously monitoring the RGA signal. Figure 52 shows the outgassing of the most intensive fragments up to a temperature of 200 K (above this temperature the signal was negligible). The absence of the signal of  $m/z = 2$  is probably due to the fact that the boiling point of hydrogen molecules is very low and thus H<sub>2</sub> is not immobilized at the temperature and pressure given in our experiment.

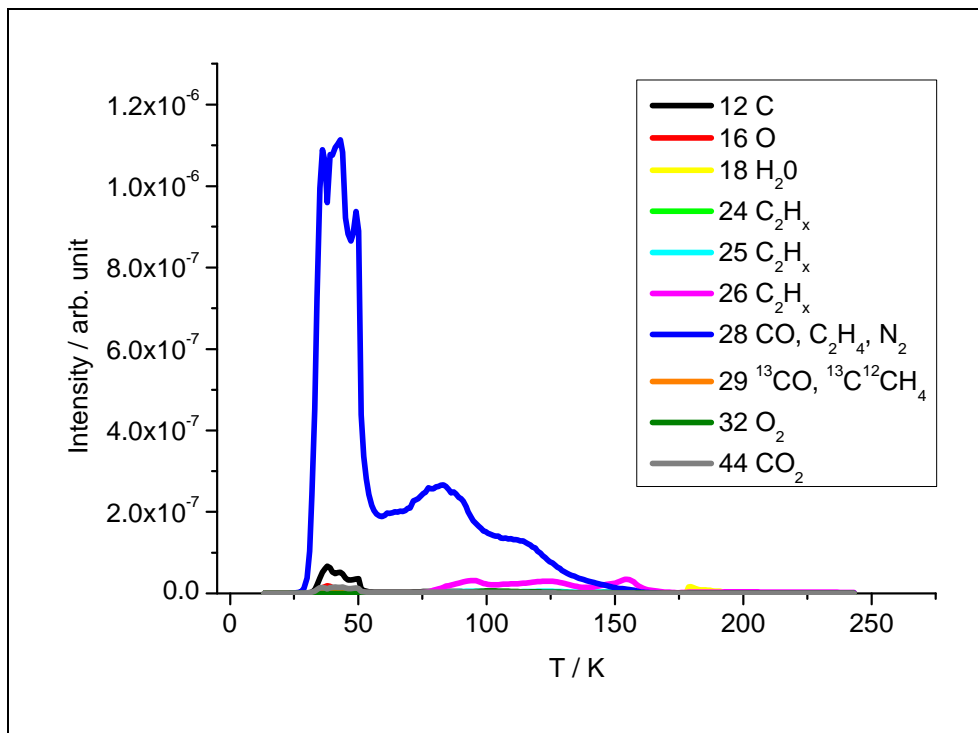
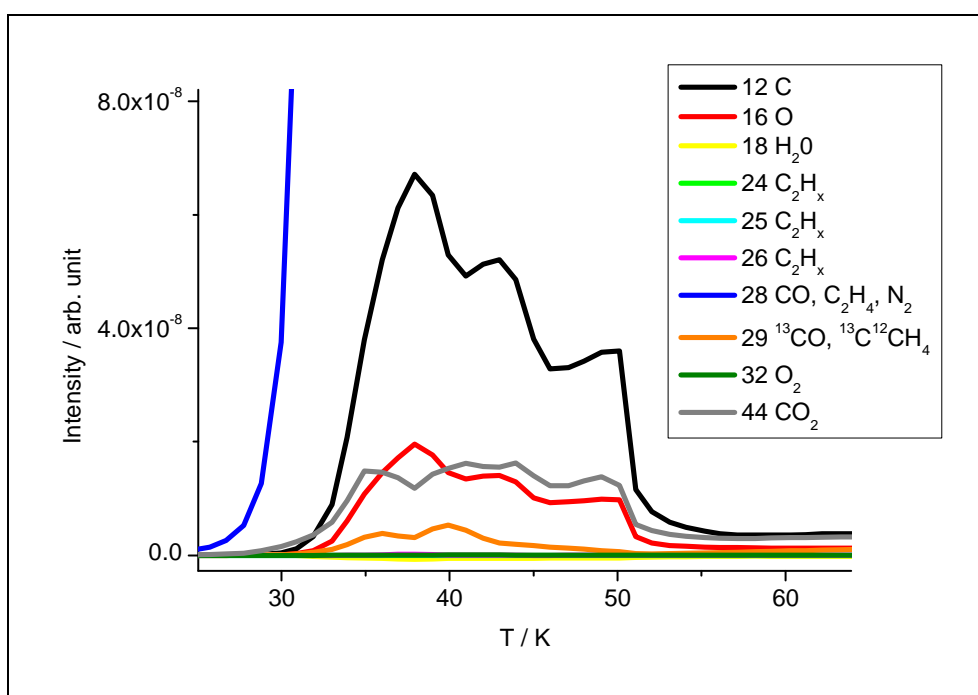


Figure 52: RGA spectrum of fragments outgassing during heat-up cycle of Kapton foil (50  $\mu$ m) after being irradiated with  $1 \times 10^{12}$  Pb ions/cm<sup>2</sup> (4.3 MeV/u). The Spectrum is background-corrected by subtraction of the heat-up cycle outgassing spectrum of an empty sample holder irradiation.

During the heating,  $m/z = 28$  represents by far the dominating outgassing product indicating that a large quantity of these molecules is accumulated in the sample during the cryogenic irradiation. The release predominantly occurs in a temperature range between 35 and 55 K. The large width of outgassing peak and its substructure probably result from a temperature gradient of the sample holder in the irradiation chamber. The outgassing temperature between 35 and 55 K supports the postulation that the  $m/z = 28$  peak corresponds to CO due to the fact that the boiling temperature of carbon monoxide (at normal pressure

bp = 81.5 K) is much smaller than the boiling temperature of ethane (at normal pressure bp = 169.5 K). This assumption is supported by the comparison with the calibrated gases CH<sub>4</sub>, CO<sub>2</sub>, and C<sub>3</sub>H<sub>4</sub> and their outgassing temperatures related to their boiling temperature at normal pressure. The outgassing temperature of CO should be at 36 K and the outgassing temperature of C<sub>2</sub>H<sub>4</sub> at 73 K. The slight and brought increase of the m/z signal 28 between 70 and 90 K indicates the outgassing of ethene.



**Figure 53:** RGA spectrum of fragments outgassing during heat-up cycle focused to the temperature region up to 60 K of Kapton foil (50  $\mu\text{m}$ ) after being irradiated with  $1 \times 10^{12}$  Pb ions/cm<sup>2</sup> (4.3 MeV/u). The Spectrum is background-corrected by subtraction of the heat-up cycle outgassing spectrum of an empty sample holder irradiation.

As illustrated in Figure 53, the signals of mass 12 (carbon), 16 (oxygen), and 29 (<sup>13</sup>CO) follow the same temperature evolution as mass 28 indicating that their origin is directly related to carbon monoxide. The ratio of the m/z = 29 to 28 signal is 1.40 – 1.45 which is close to the natural isotopic ratio of <sup>13</sup>C and <sup>12</sup>C (1.1 %). The isotopic ratio between the masses 28 and 29 is a strong indication for the molecule <sup>13</sup>CO. Figure 54 shows the comparison of the two signals on a logarithmic scale. The signal of mass 29 follows exactly the trend of mass 28 but is smaller by two orders of magnitude. Besides, the expected increase of the ratio for ethene (outgassing region of 80 K) based on the content of two carbon atoms could not be seen. The two carbon atoms in the ethene double

the probability of the  $^{13}\text{C}$  inside the molecule which leads to an increase of the ratio between the mass signals  $m/z = 28$  and  $m/z = 29$ .

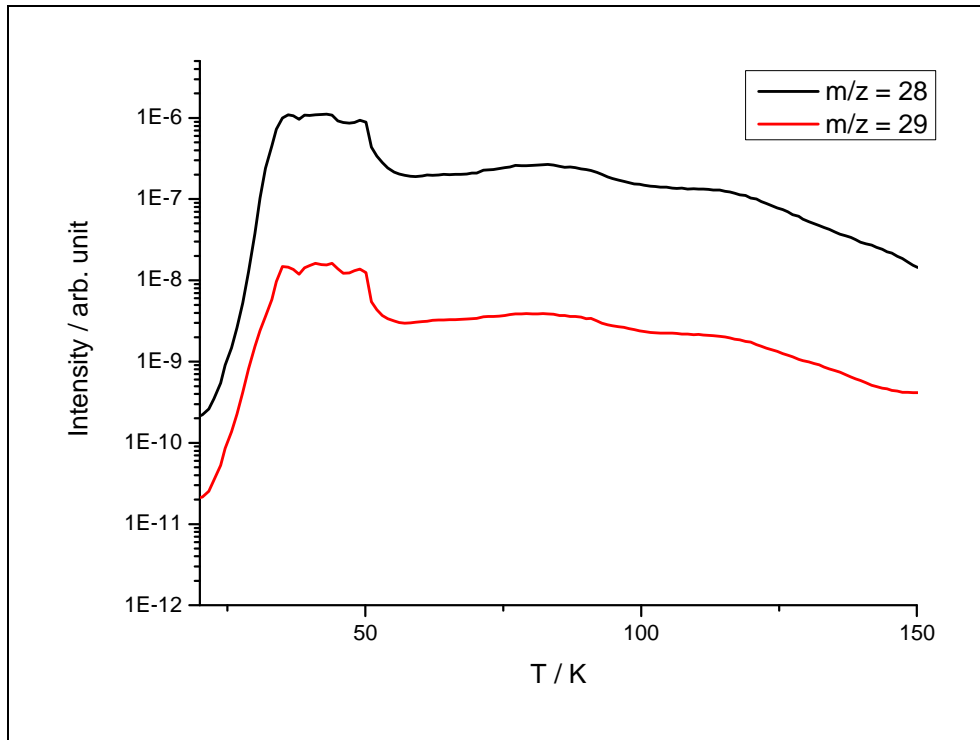


**Figure 54:** RGS signals  $m/z = 28$  and  $m/z = 29$  as a function of temperature during heating of a Kapton foil ( $50\ \mu\text{m}$ ) irradiated with  $1 \times 10^{12}$  Pb ions/ $\text{cm}^2$  ( $4.3\ \text{MeV/u}$ ). Spectrum is background-corrected by subtraction of the heat-up cycle outgassing spectrum of an empty sample holder irradiation.

Figure 55 shows the outgassing profile of  $m/z = 26$  ( $\text{C}_2\text{H}_2$ ) and its hydrogen-subtracted fragments with mass 25 and 24. The outgassing spectrum has again a triple peak structure similar to the most dominant outgassing fragment ( $m/z = 28$ ). It seems reasonable to assume that the sample holder has a temperature profile which leads to the broadening and finally to the splitting of the outgassing signals.

Carbon dioxide ( $\text{CO}_2$ ) represented at the mass-to-charge ratio 44 outgasses in the temperature region between 90 and 130 K. The reason for the very small signal of carbon dioxide is the strong tendency of fragmentation. The fragmentation appeared during the irradiation process but could also appear during the ionisation of the mass spectrometer. The two fragmentation processes could not be resolved with the experimental setup.

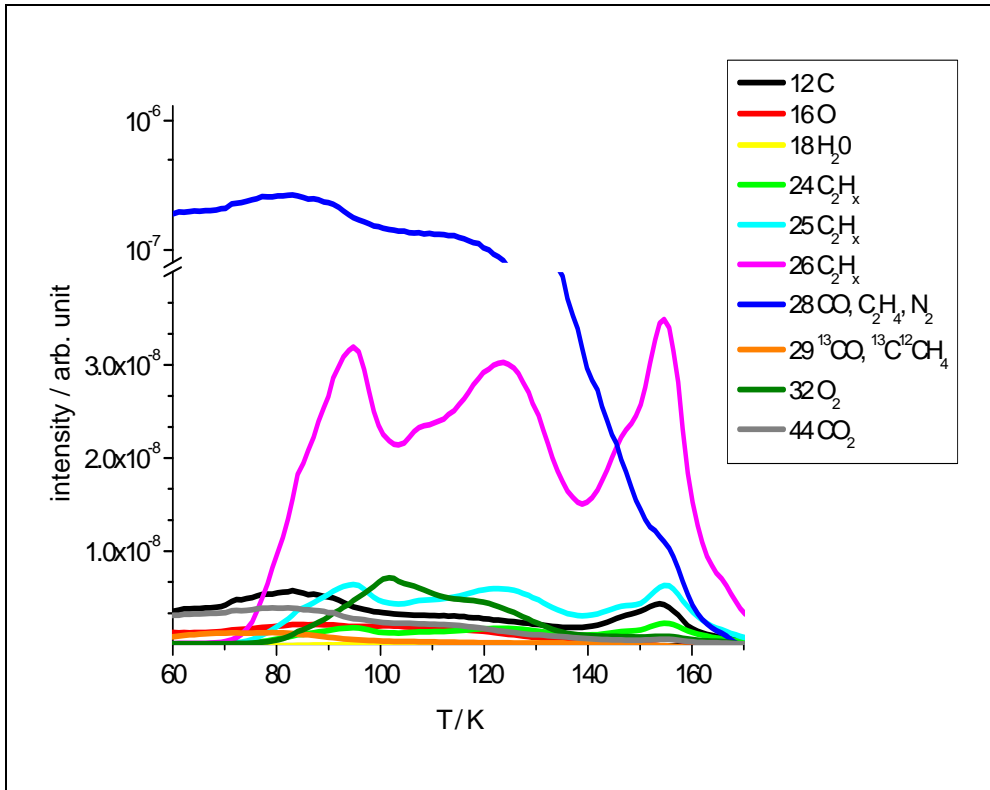


Figure 55: Enlargement of the temperature region from 60 K to 150 K of the RGA of the outgassing fragments during a heat-up cycle of a Kapton foil (50  $\mu\text{m}$ ) after irradiation with  $1 \times 10^{12}$  Pb ions/ $\text{cm}^2$  with 4.3 MeV/u. Spectrum is corrected by subtraction of the heat-up cycle outgassing spectrum of an empty sample holder irradiation.

## Chapter 6 :

# Conclusions

### 6.1 Room temperature experiments

The offline analysis by mass loss, optical spectroscopy, and by tensile strength test of the polymer degradation exhibits very similar trends: Above a critical dose region of about 1 MGy, the material properties experience change.

Figure 56 shows the results of the mass loss investigation (a), and of the three other methods (b) following the irradiation induced degradation as a function of the dose. The data points of each method are normalized to a non-irradiated sample indicating the relative degradation.

The data of all four methods underline the similar trend concerning the dose and show also that the optical and mechanical methods are scaleable with a uniform dimension given by the material change ratio (Figure 56 b). The high correlation between the optical spectroscopy and the mechanical test concerning the dose dependency as well as the quantitative material change ratio point to the possibility to use the non-destructive optical spectroscopy to predict the mechanical stability. The mass loss analysis needs a different scale due to the fact that the change of the remaining mass fraction is smaller in comparison to the other techniques (Figure 56 a).

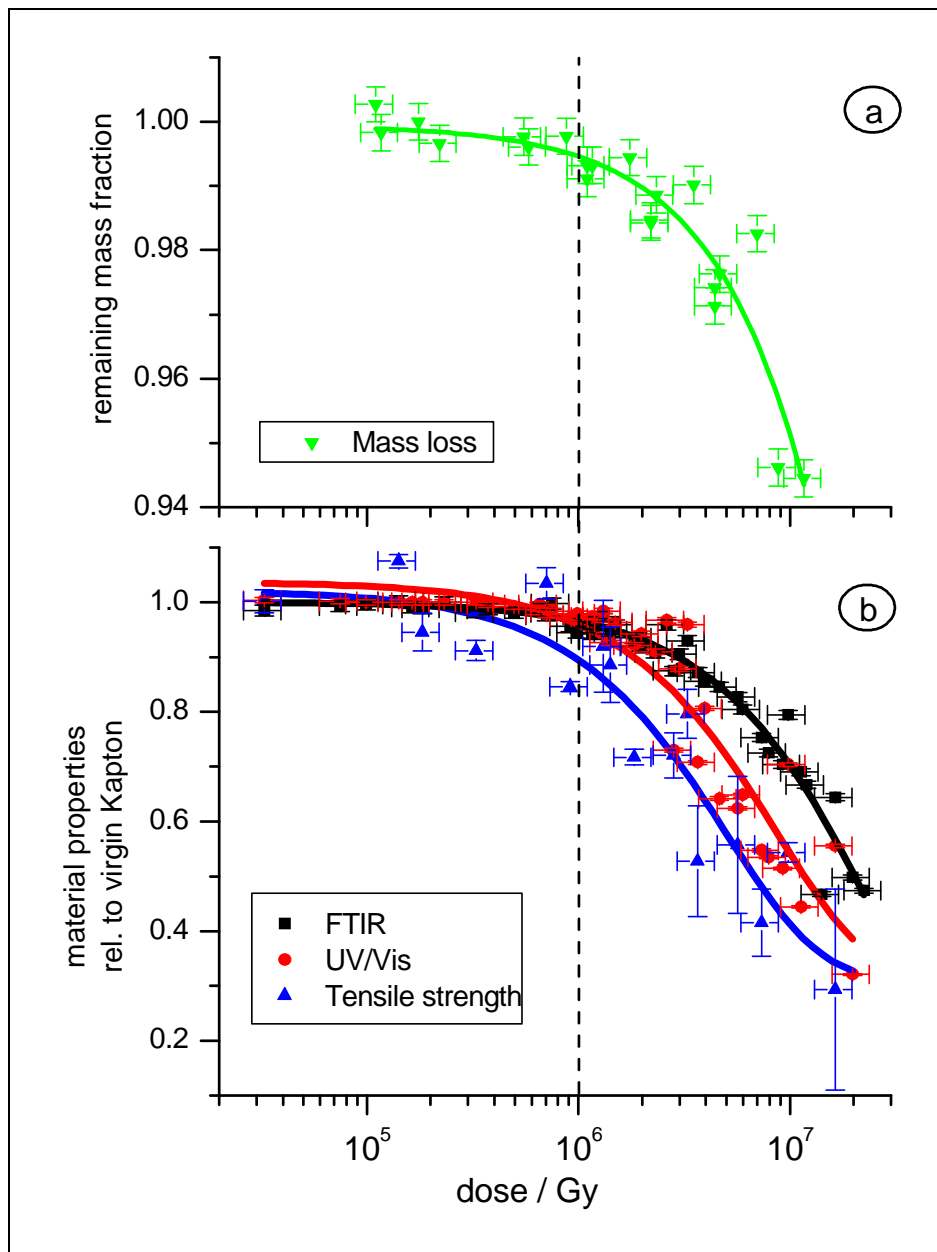


Figure 56: Material stability of Kapton described as mass stability i.e. the ratio  $m_{\text{irradiated}}/m_{\text{virgin}}$  (a) and material properties (b) analysed by infrared spectroscopy, UV/Vis spectroscopy, and tensile strength measurements (here shown the breaking stress) normalized to virgin Kapton. The lines are fitted to the data points based on an exponential function.

The points are fitted with the following exponential function [99]:

$$A = A_0 e^{-a\Phi} \quad (11)$$

where  $A$  denotes the decrease of non-irradiated area,  $A_0$  the initial sample area,  $\Phi$  the fluence, and  $a$  the effective cross section of the ion track. The equation describes the degradation process based on the assumption that each

ion degrades a defined area by a single hit and that a second hit of the same area leads to no further degradation. The exponential curve shape points to the so-called one hit process. In contrast to the two hit process where only the second hit leads to the material modification which is characterised by a s-curve shape of the degradation curve.

Fits to the results of all four methods follow this one hit rule. Especially the infrared spectroscopy is used to estimate the effective cross section of the ion track by fitting the degradation curve [100]. The track radius can be calculated based on the assumption of cylindrical tracks. Figure 57 shows the effective radii of different projectile ions related to the decrease of the infrared band at  $1117\text{ cm}^{-1}$  representing the imide ring. The values indicate an expected tendency: After a rise up to mass 100, the radius increases slightly with the projectile mass.

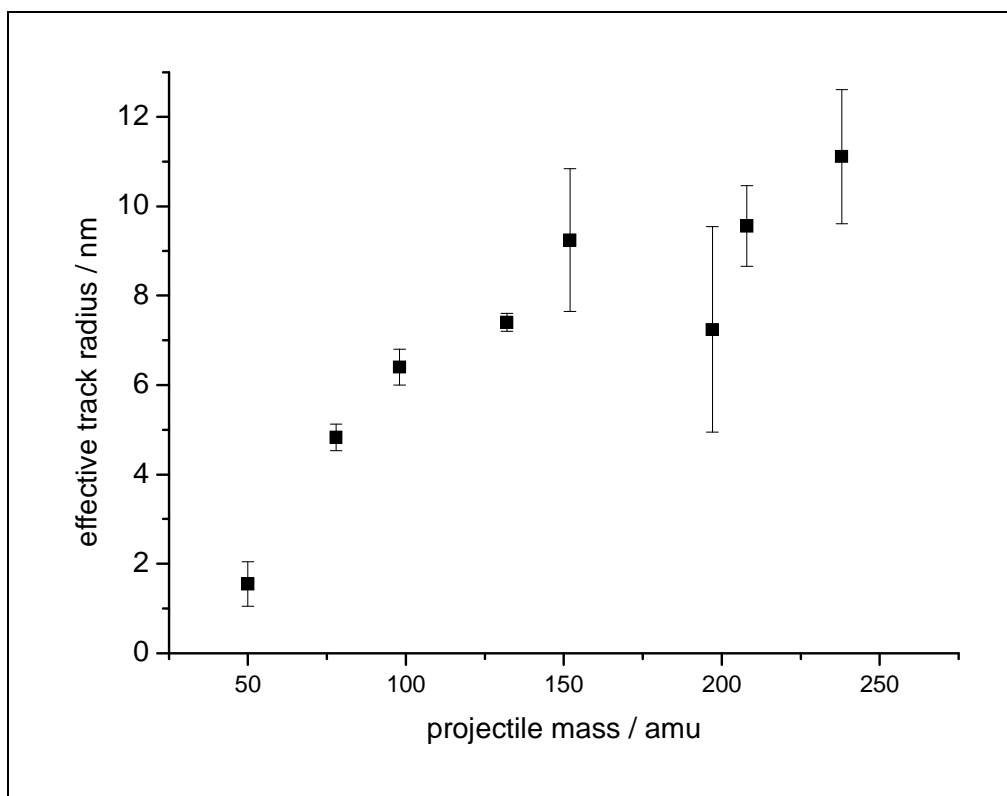


**Figure 57: Effective track radius estimated from the FTIR data for different projectiles.**

The combination of the mass loss data and the information concerning the outgassing analysis permits an estimation of the produced gas volume which is set free according to the irradiation dose. The mass loss investigations allow a calculation of the amount of gas under the assumption that only carbon

monoxide is formed as degradation fragment. Figure 58 shows the amount of CO formed out of 1 g Kapton as a function of the dose. The gas volume is calculated for normal pressure and room temperature conditions. The results exhibit nearly no gas evolution below 1 MGy. Beyond this threshold, the amount of gas which leaves the polymer increases.

It has to be clarified that this documentation provides a more concrete view to the outgassing phenomena but includes also the basic assumption that only CO is produced during the irradiation. A 50  $\mu\text{m}$  thick Kapton foil sheet with the dimensions of  $14 \times 14 \text{ cm}^2$  releases a gas volume of 44 mL during an irradiation with 10 MGy high energetic ions.

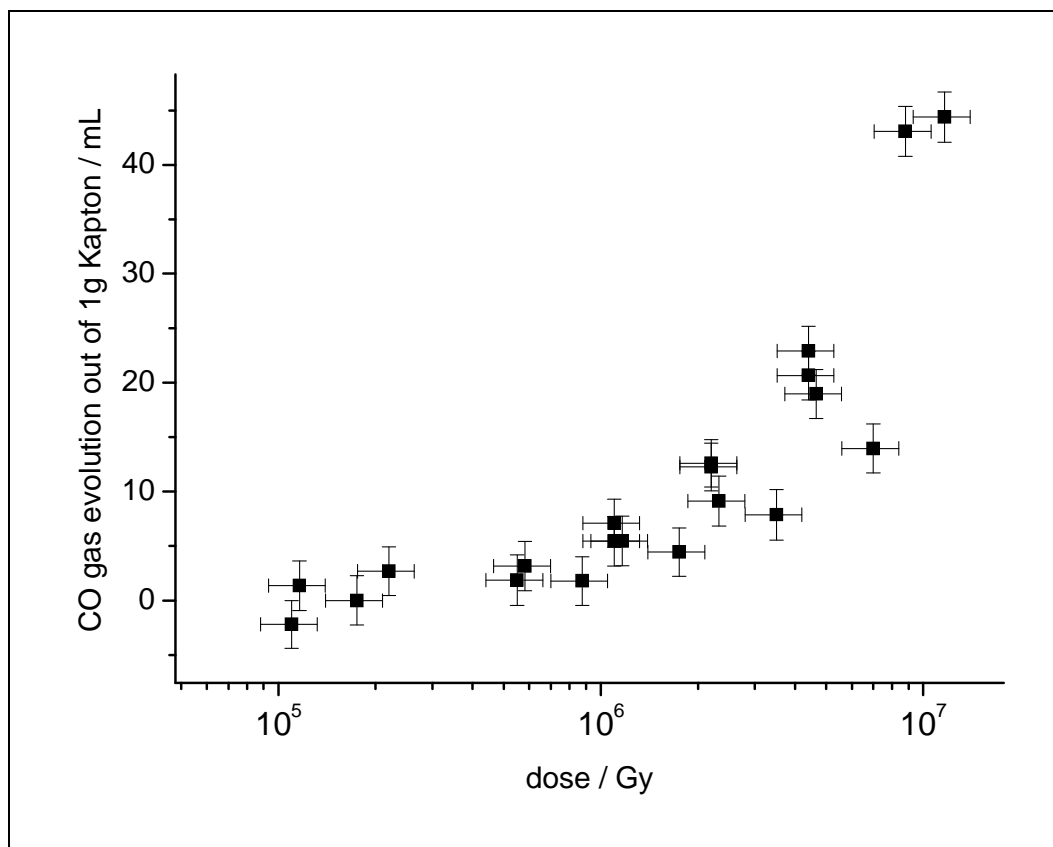


**Figure 58:** Gas evolution of 1 g Kapton calculated under the assumption that the lost mass totally outgases as carbon monoxide.

The electrical data from the DRS measurements points to a different degradation trend. Figure 59 a illustrates the material modifications concerning the conductivity on a logarithmic scale. It points out that the conductivity increases by four orders of magnitude but the data scatters dramatically without any systematic trend for the conductivity values related to the applied dose.

Heavy projectiles (Au, Sm) induce an increase to a large conductivity whereas light Ti ions exhibit only a very slight increase in conductivity by a factor of 10.

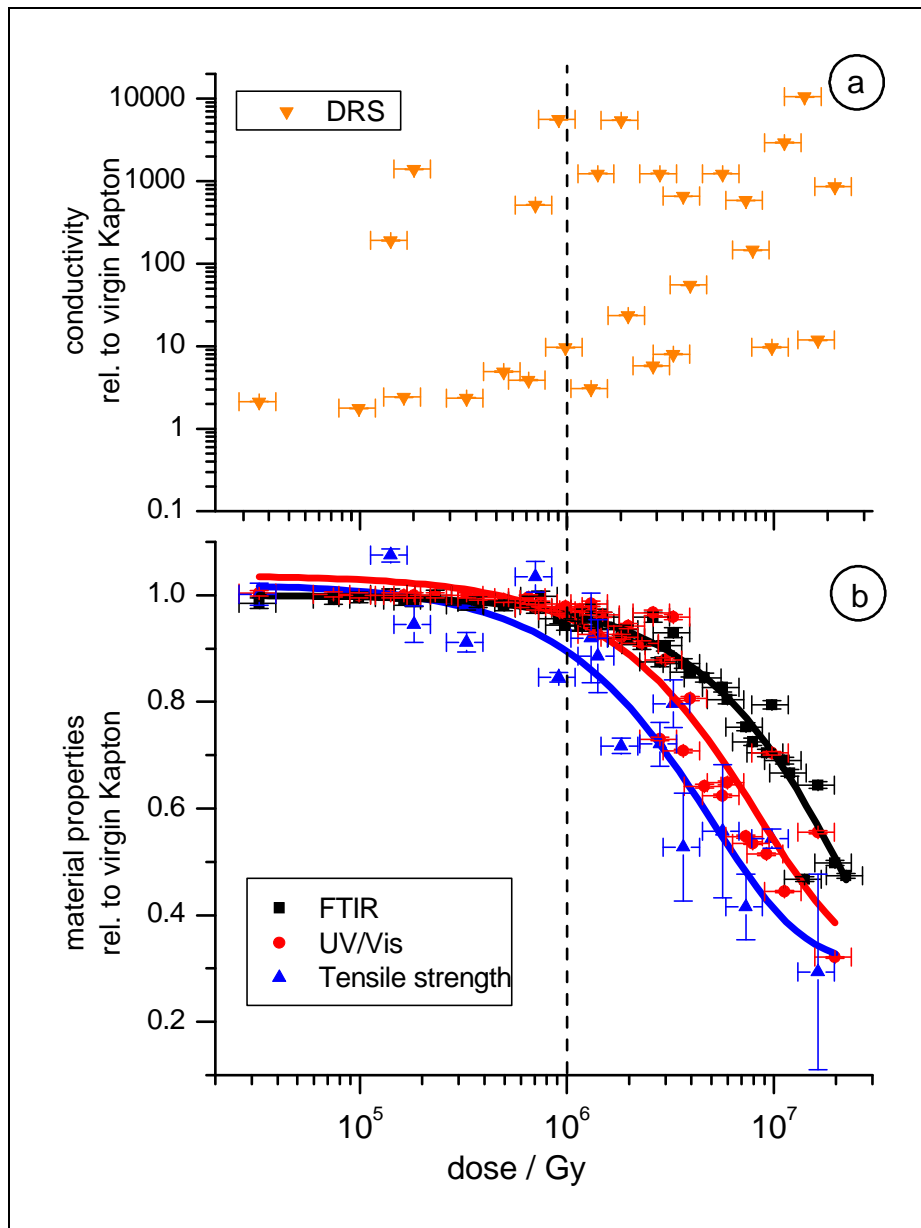


Figure 59: a) Increase of conductivity relatively to virgin Kapton analysed by means of DRS plotted on a logarithmic scale; b) Material properties normalized to virgin Kapton induced by ion irradiation indicated infrared spectroscopy, UV/Vis spectroscopy, and tensile strength measurements (here shown the breaking stress). The lines are fits to the data points based on an exponential function.

The irregular trend stands to reason that the induced conductivity is strongly linked to the deposited energy ( $dE/dx$ ) consequently also to the ion mass for constant relative beam energy ( $E/u$ ) and to the produced track size. The enormous increase in conductivity reached with heavier ions (Au, Sm) already at low fluences ( $1 \times 10^{10} - 1 \times 10^{11}$  ions/cm<sup>2</sup>) points to the phenomena that a

single track leads to a disproportionately high increase in conductivity. It is not observable by irradiation with light Ti ions which describe a material change comparable to the other analytical methods discussed before. Especially the Mo ion irradiation demonstrates a transition state between the two situations by showing a linear increase in conductivity.

The massive increase in conductivity is limited to a kind of plateau level which could be caused by an overall degradation of the material which simultaneously occurs with increasing irradiation dose. This destructive overall degradation may lead to a destruction of the created conductive structures working against the further increase of conductivity.

## 6.2 Low temperature experiments

The analysis of the irradiation induced degradation of Kapton by means of infrared spectroscopy and residual gas analysis shows massive outgassing at room temperature. At low temperature, the outgassing during irradiation is slightly reduced due to the accumulation of small degradation fragments which are frozen inside the material. The formation of CO and CO<sub>2</sub> inside the bulk material at low temperature is proportional to the irradiation dose indicated by the transition infrared spectroscopy. The release of the gasses, which occurs while warming up the sample, points to a specific outgassing temperature for each molecule.

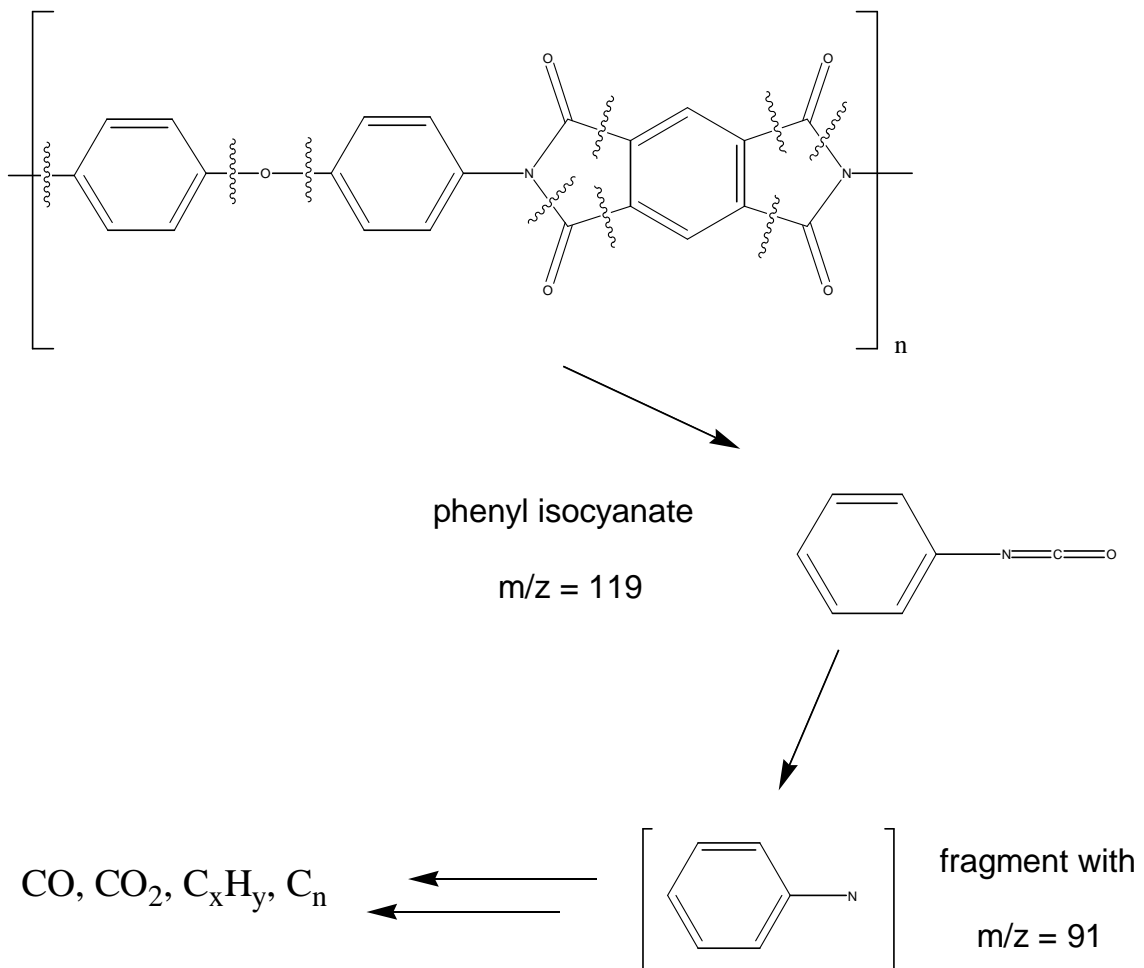


Figure 60: Initial polyimide degradation

Besides hydrogen, carbon monoxide is identified as main fragmentation product. Also the outgassing spectrum gives strong indications of the degradation mechanism by showing  $m/z$  signals of 119 and 91. Figure 60 illustrates the initial degradation coming to the phenyl isocyanate ( $m/z = 119$ ) as primary fragment after breaking the imide ring and the ether bond. The aromatic structure of the phenyl rings is very stable and keep intact in the first steps. The fragmentation of the phenyl isocyanate leads to a nitrogen substituted phenyl ring with the mass to charge ratio of 91 under subtraction of CO.

These observations are the first experimental results supporting the earlier proposed degradation mechanism induced by ion irradiation [74]. Also the identification of carbon monoxide as main fragment confirms the degradation mechanism as mentioned under 3.3.

The evaluation of the heat-up cycle after polymer irradiation gives information about critical temperature regions where a lot of gaseous molecules leave the bulk material. The fast outgassing induced by passing the boiling point of an accumulated substance initiates further material degradation (e.g. by the formation of micro cracks). The outgassing of carbon monoxide appears as the by far most intensive peak in a temperature zone between 35 and 55 K. The measurements point to an enormous gas volume related to the irradiation dose which is set free in this temperature region.

### 6.3 Consequences for the magnet design

The degradation analysis of Kapton indicates three limitations for the use of the material as insulator in superconducting magnets under high radiation levels:

- a. *mechanical stability*: mechanical tests as well as optical spectroscopy data congruently deliver a threshold of 1 MGy concerning the radiation dose induced by high energetic heavy ions. Beyond this dose level, the radiation leads to a continuing loss of material properties, shown in detail for the mechanical strength. The material is getting brittle and the UV/Vis spectroscopy shows the increase of graphite-like structures in the material.
- b. *the increase of conductivity*: the irradiation of Kapton with heavy ions ( $m > 150$ ) of an energy of 11.1 MeV/u increases the conductivity by several orders of magnitude already at moderate doses below 1 MGy. Lighter ions (Ti, Mo) indicate similar degradation tendencies as reported for optical spectroscopy and tensile strength analysis. The enormous increase of conductivity induced by heavier projectiles is especially relevant for insulator parts of the magnet which are close to the beam tube where they are exposed to large projectiles fragments.
- c. *the outgassing problematic*: the accumulation of small fragments and their later outgassing during heat-up cycles (for service) produce a large volume of volatile gases inside the magnet coil package. The expansion of the gas could induce micro cracks which influence the mechanical stability leading to a loss of magnetic field quality and end up in a failure of the entire magnet.

These arguments point to the fact that especially heavy ion irradiation leads to a loss of required properties of Kapton when use as insulator material. Mainly the material which is used close to the beam tube and hence exposed to large fragments of the primary particle beam should be protected additionally.

A possible approach is the use of a ribbon structured beam tube. Small ribbons standing perpendicularly to the beam direction on to of the beam tube lead to an increase of fragmentation. The primary particles which penetrate the beam tube wall under a small angle of incidence also have to pass the ribbons to enter into the insulator structure. The effect of this simple shielding is based on the low

angle of incidence of the primary projectiles which causes the passing of many ribbons before reaching the soft insulator material. The penetration of the stainless steel beam tube wall and the ribbons leads to an enhanced fragmentation of the primary projectile and lowers the amount of heavy particles depositing their energy inside the insulator material.

# Chapter 7 :

## Outlook

Further irradiations at GSI and at the GANIL (France) of insulator samples will specify the information concerning the degradation behaviour of polymer material. A future focus will be set on multi projectile irradiations, by which material will be analysed, which has first been pre-irradiated with light particles (protons) or X-rays and then subsequently with heavy ions. As regards the radiation level, these irradiations better reflect the situation of the insulator material which is used close to the beam tube of a particle accelerator.

This section comprises several preliminary results and a few ongoing activities which demonstrate the current research being based on this study. The following approaches show a new experimental irradiation setup and introduce further analytical methods to describe the material degradation induced by ion irradiation.

### 7.1 High dose experiment at (HHD)

The results of the study are based on the approach to create a worst case scenario by irradiating the polymer directly with swift heavy ions of a medium energy (11.1 MeV/u). A first test experiment to simulate the radiation conditions in the later magnet has been performed in a high dose experiment carried out in May 2008 at GSI in the HHD cave at the SIS beam dump. Figure 61 shows the experimental setup. The sample holder which is shown in the upper left corner is designed in a v-like structure. The samples are positioned behind a 0.3 mm

thick stainless steel plate simulating the later beam tube wall. The primary 1 GeV/u Uranium beam hits the steel plate at an angle of 2°.

An irradiation of the setup with fluences up to  $1 \times 10^{15}$  ions/cm<sup>2</sup> was planned by exposing various samples (insulating material like Kapton foils and fibre reinforced plastics (G11cr) and devices of the later magnet) to fragments of the primary beam behind the steel plate.



**Figure 61: Experimental setup for the high energy experiment at HDD.**

The sample testing is postponed until the activation has decayed to an acceptable dose level for sample handling [101]. The analysis of the samples will deliver very important information about the distribution and the amount of fragments entering into the polymer parts behind the beam tube.

## **7.2 Electrical material properties**

With respect to the unexpected results of the dielectric relaxation spectroscopy, a second analytical method is desirable to clarify the electrical behaviour of the polymer after irradiation. Therefore, the breakdown voltage test was chosen as method of choice also because of its technical relevance for the later application in the FAIR magnet.

The preliminary measurement setup could be tested in summer 2007 at CERN (Accelerator Technology Division AT/MCS/MC) in cooperation with Davide Tommasini and Roberto Lopez [102]. It consists of a current limited high voltage source and two stainless steel cylindrical electrodes with edge done by rayon of 1 mm (standard electrode). The breakdown of the material was detected by hand (taking the abrupt increase of current and the acoustic bang as indication).

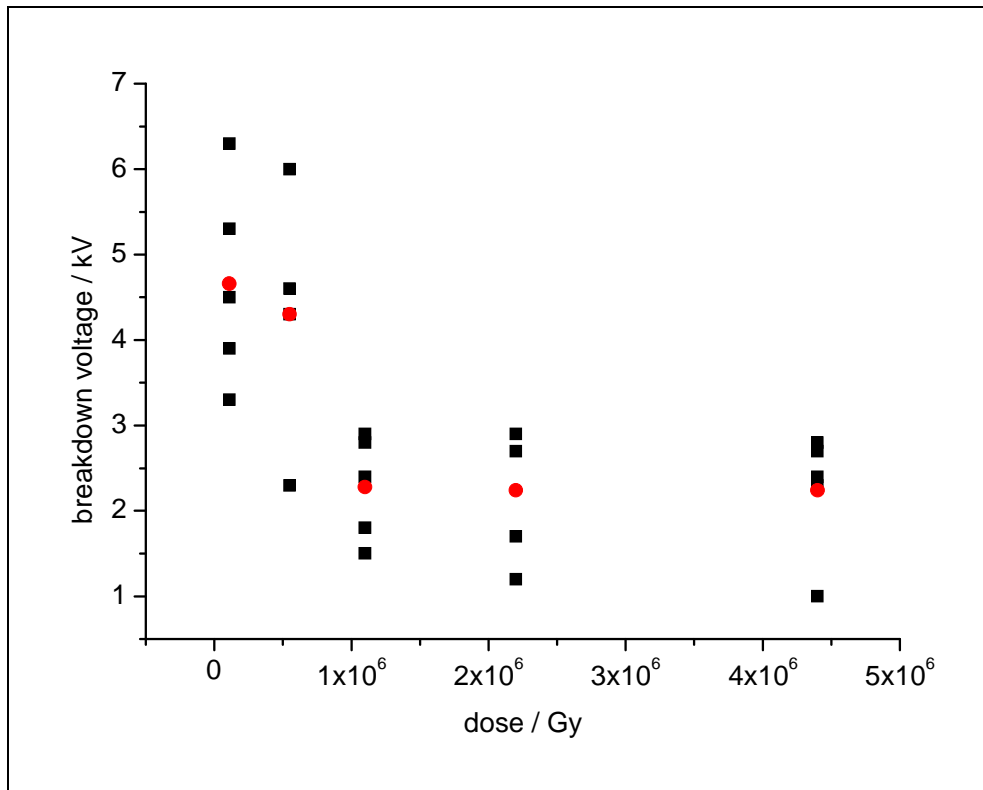


**Figure 62: Breakdown voltage test of Kapton foils (50  $\mu\text{m}$ ) irradiated with U ions.**

Figure 62 shows the first measurements. The black points represent the results of one foil measured five times at different spots. The red points display the mean value of the five tests for each sample. The diagram points to the tremendous error of the measurement as a result of the uncontrolled conditions (atmosphere and temperature) and the irreproducible detection procedure.

But nevertheless, the results indicate a significant material change which leads to the consequence that the CERN group builds up a new experimental test setup for more accurate breakdown voltage tests. The new setup is equipped with a vacuum chamber and a detection setup including an oscilloscope for recording the voltage and the current signal at breakdown. First measurements

have been performed within the framework of the dissertation of Tim Seidl but the data are not analysed yet.

### 7.3 Cryogenic conditions and the new M3 experimental station

The irradiation at cryogenic temperature is very important due to the fact that the FAIR magnet operated at 4.5 K. For this reason, experiments at the GANIL in France were carried out. Additional irradiation experiments at GSI using a cryostat were also performed to analyse quantitatively the polymer degradation by offline infrared spectroscopy in comparison to room temperature irradiation. Preliminary results denote a contradictory degradation rate given by the infrared analysis of the samples irradiated at the cryostat. Due to the experimental setup, the effect could not clearly be addressed to the temperature, also because of the oxygen concentration in the irradiation chamber which was not a controlled influence on the degradation rate.

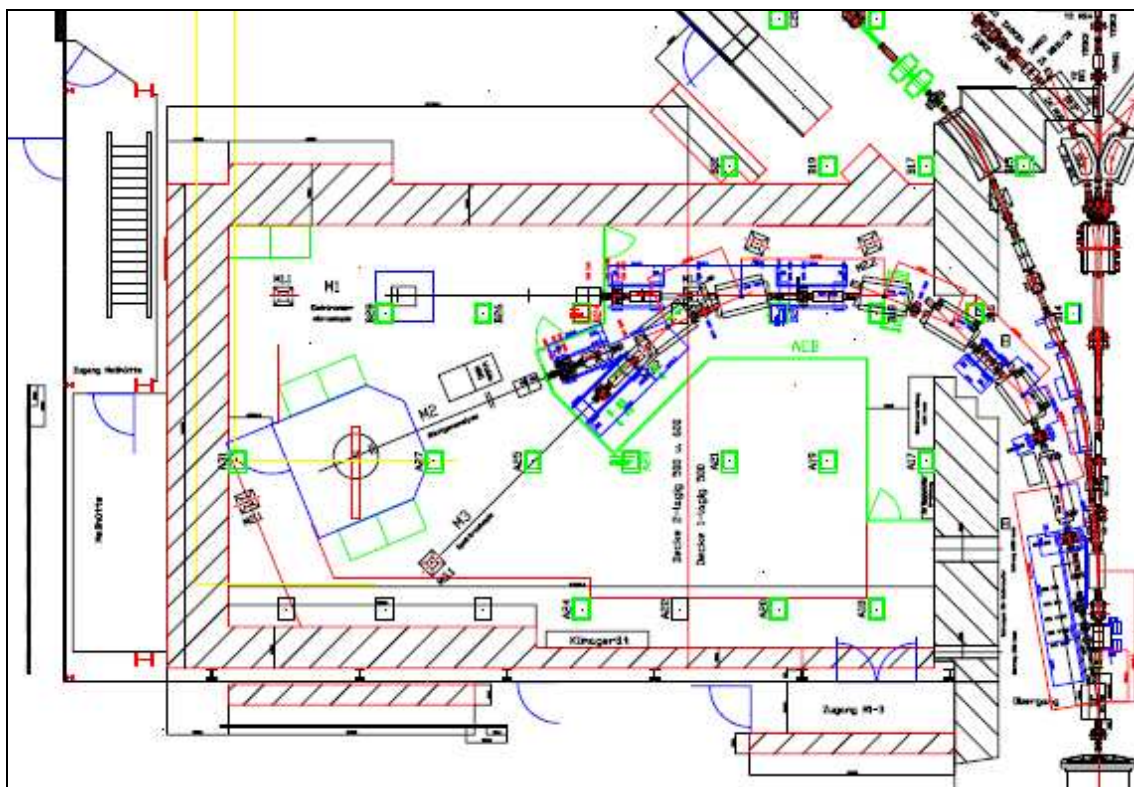
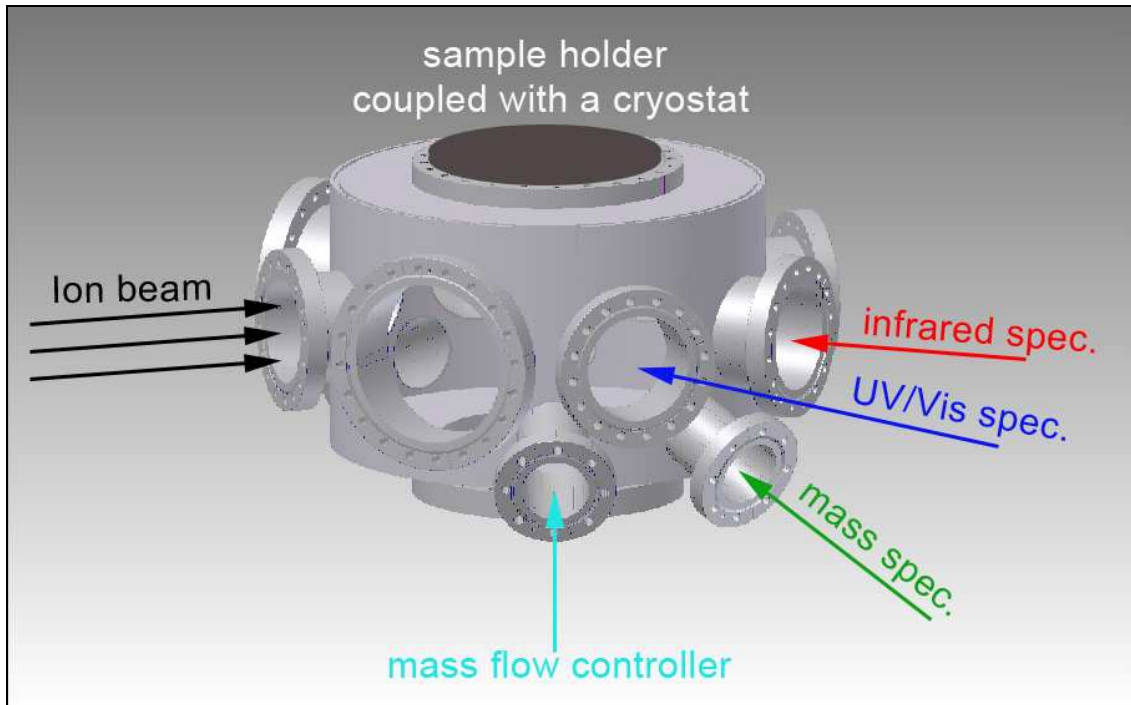


Figure 63: The new M-branch of GSI providing three new experimental stations (M1-3) with ions of the UNILAC (energies up to 11.4 MeV/u).

For further exact analysis of the material degradation behaviour at cryogenic temperature, a new experimental setup is necessary and will be realised at the newly constructed M-branch beamline at GSI which is located right behind the linear accelerator (UNILAC). Figure 63 shows the experimental cave including the three branches M1-3. An in-situ electron microscope will be installed at M1 and a goniometer for X-ray diffraction analysis at M2.

A setup for online polymer degradation analysis will be built at the M3 branch in connection with a project of the TU Darmstadt funded by the “Bundesministerium für Bildung und Forschung” (BMBF).

Figure 64 shows the planned chamber: a sample holder which is connected to a closed-cycle cryostat will be installed on top. The ion beam enters the chamber from the left side. The optical spectrometer covering the infrared and the UV/Vis spectral region are installed in-plane with the ion beam. The mass spectrometer for residual gas analysis points from a lower level to the chamber centre. The mass flow controller is also mounted at the downer level.



**Figure 64: Experimental setup of the planned M3 chamber for online polymer degradation analysis at the new M-branch of GSI.**

The setup allows to simultaneously analyse the material by means of the optical spectroscopy and the outgassing behaviour with residual gas analysis. The

sample temperature can be controlled by the cryostat. The installed mass flow controller permits the calibration of the mass spectrometer by providing a constant gas flow used as internal standard. Additionally, the chamber atmosphere can be influenced with the mass flow controller (e.g. for irradiation experiments under a controlled oxygen concentration).

This unique combination of analytical methods in addition to irradiation parameters of the GSI linear accelerator will deliver detailed information concerning the polymer degradation with special focus on the cryogenic temperature regime.

## Chapter 8 :

# Bibliography

- [1] M. H. Van de Voorde, Report: Effects of radiation on materials and components, CERN 70-5 (1970).
- [2] R. L. Clough, Nuclear Instruments & Methods in Physics Research Section B-Beam Interactions with Materials and Atoms, 185 (2001) 8-33.
- [3] O. Chauvet, S. Paschen, M. N. Bussac and L. Zuppiroli, Europhysics Letters, 26 (1994) 619-624.
- [4] F. A. Bovey, The Effects of Ionizing Radiation on Natural and Synthetic High Polymers, Interscience Publishers, New York - London, 1958.
- [5] A. Charlesby, Nature, 4343 (1954) 167.
- [6] A. Charlesby, Atomic Radiation and Polymers, Pergamon Press, New York, 1960.
- [7] A. Charlesby, Radiation Physics and Chemistry, 46 (1995) 153-154.
- [8] A. Chapiro, Radiation Physics and Chemistry, 51 (1998) 9.
- [9] G. J. Dakin, R. A. Arbelaez, F. J. Molz, J. E. Alonso, K. A. Mann and A. W. Eberhardt, Journal of Biomechanical Engineering-Transactions of the Asme, 123 (2001) 218-226.
- [10] J. Gehring, Radiation Physics and Chemistry, 57 (2000) 361-365.
- [11] D. Cangialosi, P. T. McGrail, G. Emmerson, A. Valenza, E. Calderaro and G. Spadaro, Nuclear Instruments & Methods in Physics Research Section B-Beam Interactions with Materials and Atoms, 185 (2001) 262-266.

- 
- [12] Z. Ghazali, A. F. Johnson and K. Z. Dahlan, *Radiation Physics and Chemistry*, 55 (1999) 73-79.
- [13] Y. Tabata, S. Ikeda and A. Oshima, *Nuclear Instruments & Methods in Physics Research Section B-Beam Interactions with Materials and Atoms*, 185 (2001) 169-174.
- [14] M. Grasselli, E. Smolko, N. Hargittai and A. Safrany, *Nuclear Instruments & Methods in Physics Research Section B-Beam Interactions with Materials and Atoms*, 185 (2001) 254-261.
- [15] J. L. Garnett, *Radiation Physics and Chemistry*, 46 (1995) 925-930.
- [16] P. Holl, *Radiation Physics and Chemistry*, 46 (1995) 953-958.
- [17] S. K. Datta, T. K. Chaki, V. K. Tikku, N. K. Pradhan and A. K. Bhowmick, *Radiation Physics and Chemistry*, 50 (1997) 399-405.
- [18] A. Singh, *Nuclear Instruments and Methods in Physics Research Section B: Beam Interactions with Materials and Atoms*, 185 (2001) 50-54.
- [19] S. Koh, S. Park, S. Kim, W. Choi, H. Jung and K. Pae, *Journal of Applied Polymer Science*, 64 (1997) 1913-1921.
- [20] M. Celina, H. Kudoh, T. J. Renk, K. T. Gillen and R. L. Clough, *Radiation Physics and Chemistry*, 51 (1998) 191-194.
- [21] D. M. Rück, *Nuclear Instruments and Methods in Physics Research Section B: Beam Interactions with Materials and Atoms*, 166-167 (2000) 602-609.
- [22] K. Friese and F. Tannert, *Radiation Physics and Chemistry*, 55 (1999) 47-54.
- [23] V. T. Stannett, *International Journal of Radiation Applications and Instrumentation. Part C. Radiation Physics and Chemistry*, 35 (1990) 82-87.
- [24] A. A. A. De Queiroz, R. R. Vargas, O. Z. Higa, É. R. Barrak, E. J. H. Bechara, B. Wlasdislaw and L. Marzorati, *Radiation Physics and Chemistry*, 55 (1999) 345-352.
- [25] S. Tsuneda, K. Saito, T. Sugo and K. Makuuchi, *Radiation Physics and Chemistry*, 46 (1995) 239-245.
- [26] E.-S. A. Hegazy, H. Kamal, N. Maziad and A. M. Dessouki, *Nuclear Instruments and Methods in Physics Research Section B: Beam Interactions with Materials and Atoms*, 151 (1999) 386-392.

- 
- [27] V. Haddadi-Asl and R. P. Burford, *Radiation Physics and Chemistry*, 47 (1996) 907-912.
- [28] J. M. Rosiak and P. Ulanski, *Radiation Physics and Chemistry*, 55 (1999) 139-151.
- [29] A. Chapiro, *Radiation Physics and Chemistry*, 46 (1995) 159-160.
- [30] D. A. Bedward, R. M. Brinston and J. Kotler, *Radiation Physics and Chemistry*, 46 (1995) 443-448.
- [31] G. Burillo, R. L. Clough, T. Czvikovszky, O. Guven, A. Le Moel, W. W. Liu, A. Singh, J. T. Yang and T. Zaharescu, *Radiation Physics and Chemistry*, 64 (2002) 41-51.
- [32] P. Apel, A. Schulz, R. Spohr, C. Trautmann and V. Vutsadakis, *Nuclear Instruments and Methods in Physics Research Section B: Beam Interactions with Materials and Atoms*, 131 (1997) 55-63.
- [33] P. Apel, A. Schulz, R. Spohr, C. Trautmann and V. Vutsadakis, *Nuclear Instruments and Methods in Physics Research Section B: Beam Interactions with Materials and Atoms*, 146 (1998) 468-474.
- [34] C. Trautmann, S. Bouffard and R. Spohr, *Nuclear Instruments and Methods in Physics Research Section B: Beam Interactions with Materials and Atoms*, 116 (1996) 429-433.
- [35] T. W. Cornelius, M. E. Toimil-Molares, R. Neumann and S. Karim, *Journal of Applied Physics*, 100 (2006) 114307-5.
- [36] G. Pepy, P. Boesecke, A. Kuklin, E. Manceau, B. Schiedt, Z. Siwy, M. Toulemonde and C. Trautmann, *Journal of Applied Crystallography*, 40 (2007) S388-S392.
- [37] B. Schiedt, K. Healy, A. P. Morrison, R. Neumann and Z. Siwy, *Nuclear Instruments & Methods in Physics Research Section B-Beam Interactions with Materials and Atoms*, 236 (2005) 109-116.
- [38] K. Lunkwitz, U. Lappan and D. Lehmann, *Radiation Physics and Chemistry*, 57 (2000) 373-376.
- [39] K. T. Gillen, M. Celina and R. L. Clough, *Radiation Physics and Chemistry*, 56 (1999) 429-447.
- [40] K. T. Gillen, R. Bernstein, R. L. Clough and M. Celina, *Polymer Degradation and Stability*, 91 (2006) 2146-2156.

- 
- [41] F. Hanisch, P. Maier, S. Okada and H. Schönbacher, *International Journal of Radiation Applications and Instrumentation. Part C. Radiation Physics and Chemistry*, 30 (1987) 1-9.
- [42] H. Schönbacher and A. Stolarz-Itzcka, Report: Compilation Of Radiation Damage Test Data. 2. Thermosetting And Thermoplastic Resins, CERN 79-08 (1979).
- [43] H. Schönbacher and A. Stolarz-Izycka, Report: Compilation Of Radiation Damage Test Data. 1. Cable Insulating Materials, CERN 79-04 (1979).
- [44] P. Beynel, P. Maier and H. Schönbacher, Report: Compilation Of Radiation Damage Test Data. Pt. 3. Materials Used Around High-Energy Accelerators, CERN 82-10 (1982).
- [45] G. Liptak, R. Schuler, P. Maier, H. Schönbacher, B. Haberthur, H. Müller and W. Zeier, Report: Radiation Tests On Selected Electrical Insulating Materials For High Power And High Voltage Application, CERN 85-02 (1985).
- [46] C. Chevalier, V. Coste, A. Fontaine and M. Tavlet, *Nuclear Instruments and Methods in Physics Research Section B: Beam Interactions with Materials and Atoms*, 151 (1999) 438-443.
- [47] P. Maier and A. Stolarz, Report: Long-Term Radiation Effects On Commercial Cable Insulating Materials Irradiated At Cern, CERN 83-08 (1983).
- [48] H. Kudoh, N. Kasai, T. Sasuga and T. Seguchi, *Radiation Physics and Chemistry*, 43 (1994) 329-334.
- [49] H. Kudoh, N. Kasai, T. Sasuga and T. Seguchi, *Radiation Physics and Chemistry*, 48 (1996) 695-696.
- [50] H. Kudoh, N. Kasai, T. Sasuga and T. Seguchi, *Radiation Physics and Chemistry*, 48 (1996) 89-93.
- [51] H. Kudoh, N. Kasai, T. Sasuga and T. Seguchi, *Radiation Physics and Chemistry*, 48 (1996) 95-100.
- [52] S. Takamura and T. Kato, *Journal of Nuclear Materials*, 103 (1981) 729-733.
- [53] Y. M. Sun, Z. Y. Zhu, Y. F. Jin, C. L. Liu, Z. G. Wang, J. Liu, M. D. Hou and Q. X. Zhang, *Nuclear Instruments & Methods in Physics Research*

- Section B-Beam Interactions with Materials and Atoms, 193 (2002) 214-220.
- [54] Y. M. Sun, Z. Y. Zhu and C. L. Li, Nuclear Instruments & Methods in Physics Research Section B-Beam Interactions with Materials and Atoms, 191 (2002) 805-809.
- [55] Z. Y. Zhu, Y. F. Jin, C. L. Liu, Y. M. Sun, M. D. Hou, C. H. Zhang, Z. G. Wang, J. Liu, X. X. Chen, B. Q. Li and Y. B. Wang, Nuclear Instruments & Methods in Physics Research Section B-Beam Interactions with Materials and Atoms, 169 (2000) 83-88.
- [56] Z. Y. Zhu, Y. M. Sun, C. L. Liu, J. Liu and Y. F. Jin, Nuclear Instruments & Methods in Physics Research Section B-Beam Interactions with Materials and Atoms, 193 (2002) 271-277.
- [57] Y. M. Sun, C. H. Zhang, Z. Y. Zhu, Z. G. Wang, Y. F. Jin, J. Liu and Y. Wang, Nuclear Instruments & Methods in Physics Research Section B-Beam Interactions with Materials and Atoms, 218 (2004) 318-322.
- [58] R. A. Assink, M. Celina, K. T. Gillen, R. L. Clough and T. M. Alam, Polymer Degradation and Stability, 73 (2001) 355-362.
- [59] A. De Bonis, A. Bearzotti and G. Marletta, Nuclear Instruments & Methods in Physics Research Section B-Beam Interactions with Materials and Atoms, 151 (1999) 101-108.
- [60] G. Marletta and F. Iacona, Nuclear Instruments & Methods in Physics Research Section B-Beam Interactions with Materials and Atoms, 80-1 (1993) 1045-1049.
- [61] G. Marletta, F. Iacona and A. Toth, Macromolecules, 25 (1992) 3190-3198.
- [62] H. Schönbacher and M. Tevlet, Report: Compilation Of Radiation Damage Test Data. 1. Halogen-free Materials: 2nd Edition, CERN 89-12 (1989).
- [63] I. Augustin, Nuclear Instruments and Methods in Physics Research Section B: Beam Interactions with Materials and Atoms, 261 (2007) 1014-1017.
- [64] S. Hagmann, H. F. Beyer, F. Bosch, A. Bräuning-Demian, H. J. Kluge, C. Kozhuharov, T. Köhl, D. Liesen, T. Stöhlker, J. Ullrich, R. Moshhammer, R. Mann, P. Mokler, W. Quint, R. Schuch and A. Warczak, Nuclear

- Instruments and Methods in Physics Research Section B: Beam Interactions with Materials and Atoms, 241 (2005) 5-8.
- [65] P. Spiller and G. Franchetti, Nuclear Instruments and Methods in Physics Research Section A: Accelerators, Spectrometers, Detectors and Associated Equipment, 561 (2006) 305-309.
- [66] E. Fischer, P. Shcherbakov and R. Kurnyshov, Cryogenics, 47 (2007) 583-594.
- [67] R. Spohr, Ion Tracks and Microtechnology, Principles and Applications, Vieweg & Sohn Verlagsgesellschaft mbH, Braunschweig, 1990.
- [68] H. A. Bethe, Annalen der Physik, 5 (1930) 325.
- [69] F. Bloch, Zeitschrift für Physik A Hadrons and Nuclei, 81 (1933) 363-376.
- [70] J. F. Ziegler, J. P. Biersack and U. Littmark, The Stopping Range of Ions in Solids, Pergamon Press, New York, 1985.
- [71] R. L. Fleischer, P. B. Price and R. M. Walker, Journal of Applied Physics, 36 (1965) 3645-3652.
- [72] M. Toulemonde, E. Paumier and C. Dufour, Radiation Effects and Defects in Solids, 126 (1993) 201 - 206.
- [73] J. F. Ziegler, M. D. Ziegler and J. P. Biersack, The Stopping and Range of Ions in Matter (SRIM), 2006.02: 2006.02
- [74] T. Steckenreiter, Charakterisierung von Spuren energiereicher Ionen in Polymeren, Dissertation, Technische Universität Darmstadt, Darmstadt, 1997.
- [75] DuPont, Kapton Polyimide films, Available at: [http://www2.dupont.com/Kapton/en\\_US/index.html](http://www2.dupont.com/Kapton/en_US/index.html)
- [76] N. M. Sobolevskiy, in Proceedings of the Third Yugoslav Nuclear Society International Conference YUNSC 2000 2001, Belgrade, 539.
- [77] A. A. Golubev, A. V. Kantsyrev, V. E. Luckjashin, A. Fertman, A. V. Kunin, V. V. Vatulin, A. S. Gnutov, Y. V. Panova, H. Iwase, E. Mustafin, D. Schardt, K. Weyrich, N. M. Sobolevskiy and L. N. Latysheva, Nuclear Instruments & Methods in Physics Research Section B-Beam Interactions with Materials and Atoms, 263 (2007) 339-344.
- [78] L. N. Latysheva and E. R. Mustafin, Report: Use of the SHIELD Code for Monte-Carlo modelling of the energy deposition and the fragment spectra in the elements of the SIS100 dipole magnet irradiated by 1

- GeV/u Uranium ions, Gesellschaft für Schwerionenforschung mbH (2003).
- [79] L. N. Latysheva, E. Floch, E. Mustafin and T. Seidl, Report: Estimates of radiation damage to samples S1 (1st layer) and S8 (1st part), Gesellschaft für Schwerionenforschung mbH (2008).
- [80] N. Angert, International Journal of Radiation Applications and Instrumentation. Part D. Nuclear Tracks and Radiation Measurements, 19 (1991) 871-874.
- [81] W. Barth, W. Bayer, L. Dahl, L. Groening, S. Richter and S. Yarymyshev, Nuclear Instruments and Methods in Physics Research Section A: Accelerators, Spectrometers, Detectors and Associated Equipment, 577 (2007) 211-214.
- [82] A. C. C. Villari, Nuclear Instruments and Methods in Physics Research Section B: Beam Interactions with Materials and Atoms, 204 (2003) 31-41.
- [83] H. Ishida, S. T. Wellinghoff, E. Baer and J. L. Koenig, Macromolecules, 13 (1980) 826-834.
- [84] N. B. Colthup, L. H. Daly and S. E. Wiberley, Introduction to Infrared and Raman Spectroscopy, Academic Press, New York and London, 1964.
- [85] J. Lu, S. V. Deshpande, E. Gulari, J. Kanicki and W. L. Warren, Journal of Applied Physics, 80 (1996) 5028-5034.
- [86] G. Compagnini, G. Foti, R. Reitano and G. Mondio, Applied Physics Letters, 57 (1990) 2546-2548.
- [87] R. Artiaga, M. Chipara, C. P. Stephens and R. S. Benson, Nuclear Instruments & Methods in Physics Research Section B-Beam Interactions with Materials and Atoms, 236 (2005) 432-436.
- [88] K. Dworecki, T. Hasegawa, K. Sudlitz and S. Wasik, Nuclear Instruments and Methods in Physics Research Section B: Beam Interactions with Materials and Atoms, 166-167 (2000) 646-649.
- [89] H. Ishida and M. T. Huang, Journal of Polymer Science Part B-Polymer Physics, 32 (1994) 2271-2282.
- [90] T. Steckenreiter, E. Balanzat, H. Fuess and C. Trautmann, Journal of Polymer Science Part a-Polymer Chemistry, 37 (1999) 4318-4329.

- 
- [91] J. P. Salvétat, J. M. Costantini, F. Brisard and L. Zuppiroli, *Physical Review B*, 55 (1997) 6238-6248.
- [92] C. L. Li, Y. M. Sun, Y. F. Jin, G. Liu, M. D. Hou, F. Ma and A. Patnaik, *Nuclear Instruments & Methods in Physics Research Section B-Beam Interactions with Materials and Atoms*, 135 (1998) 234-238.
- [93] J. M. Costantini, F. Couvreur, J. P. Salvétat and S. Bouffard, *Nuclear Instruments & Methods in Physics Research Section B-Beam Interactions with Materials and Atoms*, 194 (2002) 132-140.
- [94] J. M. Costantini, J. P. Salvétat, F. Brisard, M. P. Cals, J. P. Marque and F. Issac, *Nuclear Instruments & Methods in Physics Research Section B-Beam Interactions with Materials and Atoms*, 116 (1996) 496-501.
- [95] J. P. Salvétat, A. Berthault, F. Brisard, J. M. Costantini and J. Davenas, *Radiation Effects and Defects in Solids*, 136 (1995) 1177-1182.
- [96] J. P. Salvétat, J. M. Costantini and F. Brisard, *Nuclear Instruments & Methods in Physics Research Section B-Beam Interactions with Materials and Atoms*, 116 (1996) 284-288.
- [97] T. Steckenreiter, E. Balanzat, H. Fuess and C. Trautmann, *Nuclear Instruments & Methods in Physics Research Section B-Beam Interactions with Materials and Atoms*, 151 (1999) 161-168.
- [98] T. Steckenreiter, E. Balanzat, H. Fuess and C. Trautmann, *Nuclear Instruments & Methods in Physics Research Section B-Beam Interactions with Materials and Atoms*, 131 (1997) 159-166.
- [99] J. F. Gibbons, *Proceedings of the IEEE*, 60 (1972) 1062.
- [100] L. S. Farenzena, R. M. Papaleo, A. Hallen, M. A. deAraujo, R. P. Livi and B. U. R. Sundqvist, *Nuclear Instruments & Methods in Physics Research Section B-Beam Interactions with Materials and Atoms*, 105 (1995) 134-138.
- [101] A. Fertman, E. Mustafin, R. Hinca, I. Strasík, M. Pavlovic, D. Schardt, N. Sobolevskiy, A. Golubev, B. Sharkov, G. Fehrenbacher, I. Hofmann, H. Iwase, E. Kozlova and G. Mustafina, *Nuclear Instruments and Methods in Physics Research Section B: Beam Interactions with Materials and Atoms*, 260 (2007) 579-591.
- [102] R. Lopez, Report: Dielectrical test on irradiated Kapton foils provided by GSI, CERN (2007).

## Chapter 9 :

# Appendix

### Used material

#### **Kapton**

Kapton HN foils from DuPont with different thicknesses of 12, 25, and 50  $\mu\text{m}$  were used.

### Used Instruments

#### **Infrared spectroscopy**

The infrared measurements were performed with a Nicolet Magna-IR 550 with TGS detector at GSI, materials research in Darmstadt, Germany or with a Magna-IR 550 with cooled TE DLaTGS detector at CIRIL in Caen, France.

#### **UV/Vis spectroscopy**

The UV/Vis spectroscopic measurements were carried out with an ATI UNICAM double beam spectrometer (UV4) at GSI, materials research in Darmstadt, Germany with a resolution of 2 nm.

**Dielectric relaxation spectroscopy**

The dielectric measurements were performed with a frequency response analysis at the DKI in Darmstadt, Germany. The system consists of a Solartron SI 1260 Impedance/Gain phase analyzer and a Novocontrol broadband dielectric converter. Additionally the capacity was measured with a HP 4284 LCR.

**Residual Gas Analysis**

The residual gas analyses were done with a quadrupole mass spectrometer (QMS) from Balzer (Prisma QMS 200) operated in the scan mode for mass-to-charge ratio ( $m/z$ ) from 1 to 200 at CIRIL in Caen, France.

**Tensile strength**

The tensile strength measurements were performed at the Deutsches Kunststoff Institut (DKI) in Darmstadt, Germany with a Zwick Z020TH<sup>2a</sup> (with macro setup).

---

## Acknowledgement

Last but not least, it is a pleasure for me to thank the numerous people who contributed to this thesis by giving me their support. In particular, I would like to express my deep and sincere gratitude to:

- my supervisor, Prof. Dr. W. Ensinger for giving me the opportunity to accomplish this thesis in his group at the Philipps-University of Marburg and subsequently in his group at the Technische Universität Darmstadt;
- Prof. Dr. H. Jungclas for acting as referee and for his accommodation at the Nuclear Chemistry in Marburg;
- Prof. Dr. A. Greiner and Prof. Dr. J. Wendorff for being members of the examination committee;
- Dr. C. Trautmann for guiding me through the world of high energetic particles and accelerators as well as for introducing me to a great scientific community. Furthermore I would like to thank her for all the help and support she provided me with during my doctoral research work as well as for reading and correcting this and many other manuscripts;
- Prof. R. Neumann and Dr. G. Walter for their help and support at the GSI;
- Dr. E. Balanzat and all involved staff of the CIRIL at the GANIL in Caen, France for their contributions to the investigation of cryogenic polymer degradation and its outgassing behaviour;
- Prof. Dr. I. Alig, Dr. S. Dudkin, and Mr. R. Damko from the DKI in Darmstadt for the collaboration with respect to the dielectric relaxation spectroscopy and the tensile strength measurements;
- Tim Seidl for his support during his diploma and (ongoing) PhD. time;
- Dr. D. Tommasini and R. Lopez from the AT/MCS division of CERN for further testing the electrical properties of irradiated Kapton;

- 
- Dr. F. Sittner and Dr. T. Zimmermann for introducing me to the post-student life;
  - Dr. B. Schiedt, Dr. T. Cornelius, Dr. K.-O. Voss and the group of Materials Research of GSI for many fruitful discussions and for helping me with gaining a deeper insight into physics and into the world around a particle accelerator;
  - the members of the Nuclear Chemistry of the Philipps-University of Marburg for giving me a shelter. In particular, I express my thanks to Dr. B. Herrmann for the numerous discussions and her “open door policy” as well as to R. Streng for the various occasions when we have been saving the world.

---

**Eidesstattliche Erklärung**  
(gem. § 5 der Promotionsordnung)

Ich versichere, dass ich meine Dissertation „Study of the degradation process of polyimide induced by high energetic ion irradiation“ selbständig, ohne unerlaubte Hilfe angefertigt und mich dabei keiner anderen als der von mir ausdrücklich bezeichneten Quellen und Hilfen bedient habe.

Die Dissertation wurde in der jetzigen oder einer ähnlichen Form noch bei keiner anderen Hochschule eingereicht und hat noch keinen sonstigen Prüfungszwecken gedient.

Marburg, den 08.08.2008